



Functional Hydrogels

Dissertation

zur Erlangung des Grades

Doktor der Naturwissenschaften

im

Fachbereich Chemie, Pharmazie und Geowissenschaften
der Johannes Gutenberg-Universität Mainz

vorgelegt von

Robert Fokko Roskamp
geboren in Bad Schwalbach

Mainz, im Juli 2009

Die vorliegende Arbeit wurde am

Max-Planck-Institut für Polymerforschung in Mainz, am

IESL-FORTH in Heraklion und am

Ian Wark Research Institute in Adelaide

unter Anleitung von

Prof. Dr. [REDACTED], Prof. Dr. [REDACTED] und Dr. [REDACTED]

in der Zeit von Juli 2006 bis Juli 2009 angefertigt.

Dekan:

1. Berichterstatter:

2. Berichterstatter:

Übrige Mitglieder der Prüfungskommission:

Tag der mündlichen Prüfung:

Prof. Dr. [REDACTED]

Prof. Dr. [REDACTED]

Prof. Dr. [REDACTED]

Prof. Dr. [REDACTED]

Prof. Dr. [REDACTED]

03. September 2009

Abstract

Hydrogels are used in a variety of applications in daily life, such as super absorbers, contact lenses and in drug delivery. Functional hydrogels that allow the incorporation of additional functionalities have enormous potential for future development. The properties of such hydrogels can be diversified by introducing responsiveness to external stimuli. These crosslinked polymers are known to respond to changes in temperature, pH and pressure, as well as chemical and electrical stimuli, magnetic fields and irradiation. From this responsive behavior possible applications arise in many fields like drug delivery, tissue engineering, purification and implementation as actuators, biosensors or for medical coatings. However, their interaction with biomaterial and way of functioning are yet not fully understood.

Therefore, thorough investigations regarding their optical, mechanical and chemical nature have to be conducted.

A UV-crosslinkable polymer, consisting of *N*-isopropylacrylamide, methacrylic acid and the UV-crosslinker 4-benzoylphenyl methacrylate was synthesized. Its composition, determined by a comprehensive NMR study, is equivalent to the composition of the monomer mixture. The chemical characteristics were preserved during the subsequently formation of hydrogel films by photo-crosslinking as proved by XPS. For the optical characterization, e.g. the degree of swelling of very thin films, the spectroscopy of coupled long range surface plasmons is introduced. Thicker films, able to guide light waves were analyzed with combined surface plasmon and optical waveguide mode spectroscopy (SPR/OWS). The evaluation of the data was facilitated by the reverse Wentzel-Kramers-Brillouin (WKB)-approximation.

The mesh size and proper motion of the surface anchored hydrogels were investigated by fluorescence correlation spectroscopy (FCS), micro photon correlation spectroscopy (μ PCS) and SPR/OWS. The studied gels exhibit a mesh size that allowed for the diffusion of small biomolecules inside their network. For future enhancement of probing diffusants, a dye that enables FRET in FCS was immobilized in the gel and the diffusion of gold-nanoparticles embedded in the polymer solution was studied by PCS.

These properties can be conveniently tuned by the crosslinking density, which depends on the irradiation dose. Additionally, protocols and components for polymer analogous reactions based on active ester chemistry of the hydrogel were developed.

Based on these syntheses and investigations, the hydrogel films are applied in the fields of medical coatings as well as in biosensing as matrix and biomimetic cushion. Their non-adhesive properties were proved in cell experiments, SPR/OWS and ToF-SIMS studies. The functionality and nonfouling property of the prepared hydrogels allowed for adaption to the needs of the respective application.

Contents

Abstract	i
1 Introduction	1
1.1 Hydrogels	1
1.1.1 Responsive Hydrogels	2
1.1.2 Functional Hydrogels	6
1.1.3 PNIPAAm-based Hydrogels	7
1.2 Biosensors	7
1.3 Bio-Compatibility and Non-Fouling	9
1.4 Aim and Outline of the Thesis	12
2 Methods	15
2.1 Contact Angle Measurement	15
2.2 Surface Plasmon Resonance Spectroscopy (SPR)	16
2.3 Optical Waveguide Mode Spectroscopy (OWS)	22
2.3.1 Wentzel-Kramers-Brillouin (WKB)-Approximation	24
2.4 Correlation Spectroscopy	27
2.4.1 Fluorescence Correlation Spectroscopy (FCS)	27
2.4.2 Photon Correlation Spectroscopy (PCS)	29
2.5 X-ray Photoelectron Spectroscopy (XPS)	30
2.6 Time of Flight Secondary Ion Mass Spectrometry (ToF-SIMS)	31
2.7 Electrochemical Impedance Spectroscopy (EIS)	32
3 Preparation of the Hydrogel	37
3.1 Polymerization	37
3.2 Grafting	39
3.3 Crosslinking	41
3.4 Chemical Modification	42
3.5 Outlook	44

3.6	Experimental Part	44
3.6.1	P(NIPAAm-stat-MAA-stat-MABP)	44
3.6.2	BP-silane	45
3.6.3	Active Esters	46
3.6.3.1	TFA-NHS	46
3.6.3.2	TFA-AO	46
3.6.3.3	TFA-TFPS	46
3.6.3.4	TFA-DMPS	47
3.6.4	Aminomethylbenzophenone	48
3.6.5	Benzophenylacrylamide	49
4	Chemical Characterization	51
4.1	Polymer Composition by NMR	51
4.2	Hydrogel Surface Chemistry by XPS	53
4.3	Conclusion	56
4.4	Experimental Part	56
5	Optical Characterization	57
5.1	Coupled Long Range Surface Plasmon (cLRSP) Spectroscopy	58
5.1.1	Introduction	58
5.1.2	Thin Hydrogel Layers and Diffusion of BSA	59
5.1.3	Conclusion and Outlook	62
5.1.4	Experimental Part	63
5.2	WKB-assisted SPR/OWS	64
5.2.1	Introduction	64
5.2.2	Gradient Fitting	64
5.2.3	Conclusion and Outlook	67
5.2.4	Experimental Part	67
6	Dynamic Characterization	69
6.1	Tracking-Probe Diffusion	69
6.1.1	Introduction	69
6.1.2	FCS of Rhodamine 6G Diffusion	70
6.1.2.1	Diffusion in the Free Polymer	71
6.1.2.2	Diffusion in the Crosslinked Hydrogel	74
6.1.3	FRET-excited FCS	76
6.1.4	PCS of embedded Gold-Nanoparticles	78
6.1.5	WKB-assisted SPR/OWS of Polymer Diffusion	84

6.1.6	Conclusion and Outlook	88
6.1.7	Experimental Part	89
6.2	Tracking-Probes with various Sizes and Charges	92
6.2.1	Introduction	92
6.2.2	PEG-Dye	93
6.2.3	Conclusion and Outlook	95
6.2.4	Experimental Part	95
6.3	Gel Dynamics	99
6.3.1	Introduction	99
6.3.2	FCS of Dye-labeled Hydrogel	100
6.3.3	μ PCS of the Hydrogel	103
	6.3.3.1 Fast Mode Relaxation	105
	6.3.3.2 Slow Mode Relaxation	107
6.3.4	Conclusion and Outlook	108
6.3.5	Experimental Part	109
7	Application	111
7.1	Biosensor Matrix	111
7.1.1	Introduction	111
7.1.2	Immobilization of BSA	113
7.1.3	Antifouling Properties	113
7.1.4	Detection of Neutraavidin	114
7.1.5	Conclusion and Outlook	116
7.1.6	Experimental Part	116
7.2	Cell-resistant Implant Coatings	118
7.2.1	Introduction	118
7.2.2	Cell Experiments	120
7.2.3	Conclusion and Outlook	122
7.2.4	Experimental Part	122
7.3	Protein-resistant Coatings: A ToF-SIMS Study	123
7.3.1	Introduction	123
7.3.2	ToF-SIMS Measurements	124
	7.3.2.1 Evaluation of Negative Ionized Fragments	124
	7.3.2.2 Evaluation of Positive Ionized Fragments	128
	7.3.2.3 Evaluation by Principle Component Analysis	129
7.3.3	Conclusion and Outlook	130
7.3.4	Experimental Part	130

7.4	A Hydrogel-supported ptBLM	132
7.4.1	Introduction	132
7.4.2	Hydrogel-smoothed ITO	134
7.4.3	Formation of the Supported Membrane	137
7.4.3.1	EIS-Measurements	137
7.4.4	Conclusion and Outlook	139
7.4.5	Experimental Part	140
7.4.5.1	Preparation of the Substrate	140
7.4.5.2	Preparation of the Membrane	141
8	Conclusion and Outlook	143
	Abbreviations	150
	Bibliography	151
	Danksagung	175

1 Introduction

Today, polymers are ubiquitous in our daily life as well as in science, medicine and engineering. We use dishes made from melamine, diapers consist of superabsorbers made from polyacrylates and electric cables are isolated with polyvinyl chloride. Polymers control the hardening of concrete and aromatic polyamides are applied in safety clothing. Polyethylene glycol (PEG) is used in toothpaste, drug delivery and tissue engineering, and GPC columns are filled with polystyrene beads, as it is employed as stationary phase in solid phase peptide synthesis. For some applications, so called hydrogels, which are commonly water swollen, but insoluble networks, gained more and more interest.

1.1 Hydrogels



Fig. 1.1: Tanakas famous polyelectrolyte hydrogel.^[1]

Gels, originating from the Latin *gelatus* – frozen, are defined as fine dispersed systems, consisting of solid and liquid or gaseous phases. The solid phase or phases form a three dimensional network, acting as host for the liquid or gaseous

phases. In case of a gas as dispersant the system is called aerogel, whereas a host for liquids is referred to as lyogel. In the following lyogels with water as liquid phase – hydrogels – are discussed.

Silica gels and gelatine are well known examples for physically, non-covalently crosslinked hydrogels or aqueous colloidal dispersions. There, the network is formed and stabilized by van-der-Waals interaction, hydrogen bonding or charge attraction. These gels are stable, but can easily be reliquified, e.g. by shaking.

In contrast, chemically, covalently crosslinked hydrogels do not reliquify, they can only loose the accumulated water, turning them back into a solid. This process is reversible. The ability to take up a multiple of their own weight in water is one of the reasons why hydrogels are applied in a broad variety of fields. For instance, polyvinyl alcohol is used as gelatinizing agent in water gel explosives,^[2] polyhydroxyethyl methacrylate (PHEMA) is found in contact lenses,^[3] polyacrylates in diapers^[4] and some, like PEG cover numerous areas from skin cream to solid phase material in gas chromatography.^[5,6]

Environmentally sensitive hydrogels were intensively explored during the last decades as their behavior, like the swelling state can be controlled by external stimuli. These polymers are often called ‘smart’, ‘intelligent’ or ‘stimuli responsive’ hydrogels.

1.1.1 Responsive Hydrogels

After the discovery of responsive hydrogels in the late seventies by Tanaka *et al.*,^[7] a large number of polymers were identified, responding to all thinkable stimuli.^[8–10] Brief examples are response to changes in temperature, pH, pressure, and to irradiation, electric fields and chemical stimuli. This response can be from a small change in the degree of swelling to the complete collapse and total inversion of their properties.

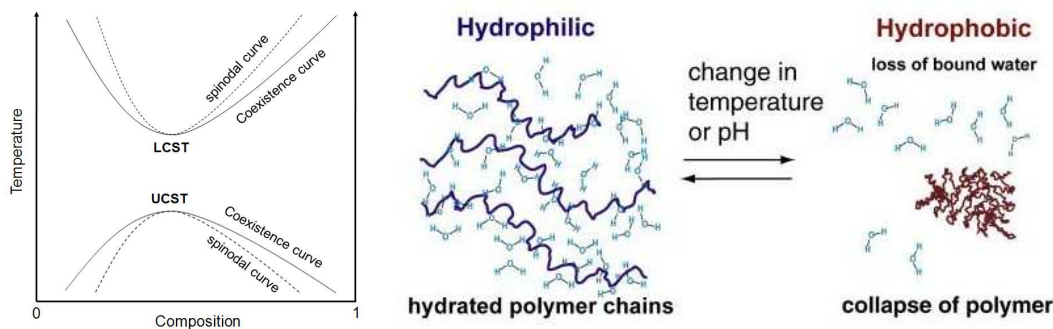


Fig. 1.2: Left: phase diagram with LCST and UCST. Right: schematic mechanism.^[11]

The most frequently used stimulus, a change in temperature, is based on the solution behavior of the polymers. Some hydrogels are temperature sensitive as they exhibit a critical solution temperature. They undergo a volume-phase transition with temperature. Contrary to most other polymers, most of them show a decreased solubility in water with rising temperature. Above their lower critical solution temperature (LCST), they collapse (see fig 1.2). The LCST depends foremost on the ratio of hydrophilic and hydrophobic segments within the polymer or a single monomer, but effects like crosslinking density and grafting should not be neglected. A selection of frequently studied polymers with a LCST in water is listed in table 1.1.

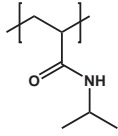
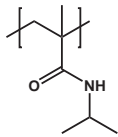
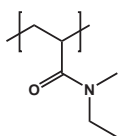
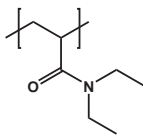
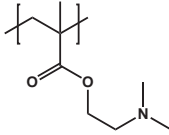
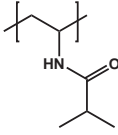
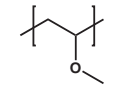
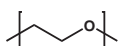
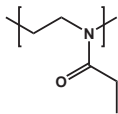
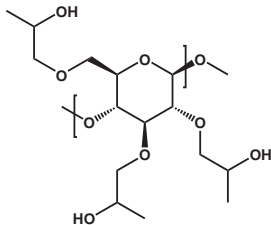
Of special interest are those with a transition temperature in the physiological regime, as they can be applied for drug delivery and allow for controlled interaction with biomolecules.^[12]

Interestingly, the reverse behavior exists as well. Few polymers, like polysulfobetaines, are known to have an upper critical solution temperature (UCST) (see fig. 1.2).^[13]

Temperature sensitive polymers are generally pressure sensitive as well. Upon applying hydrostatic pressure they expand, as the response to pressure is attributed to the same physical properties as the LCST, which increases with rising pressure.^[14]

1 Introduction

Table 1.1: List of polymers with LCST *in water

Polymer name	Polymer structure	LCST*	Lit.
Poly- <i>N</i> -isopropylacrylamide		33°C	Schild, <i>Progr. Polym. Sci.</i> , 1992 , 17., 163
Poly- <i>N</i> -isopropylmethacrylamide		40°C	Netopilik <i>et al.</i> , <i>Macromol. Rapid Commun.</i> , 1997 , 18., 107
Poly- <i>N</i> -ethyl- <i>N</i> -methylacrylamide		56°C	Plate <i>et al.</i> , <i>Polym. J.</i> , 1999 , 31., 21
Poly- <i>N,N</i> -diethylacrylamide		32°C	Idziak <i>et al.</i> , <i>Macromol.</i> , 1999 , 32., 1260
Poly- <i>N,N</i> -dimethylaminoethylmethacrylate		50°C	Cho <i>et al.</i> , <i>Europ. Polym. J.</i> , 1999 , 35., 1841
Polyvinylisobutyroamide		35°C	Akashi <i>et al.</i> , <i>J. Polym. Sci. Polym. Chem.</i> , 1996 , 34., 301
Polymethylvinylether		36°C	Ichijo <i>et al.</i> , <i>Radiat. Phys. Chem.</i> , 1995 , 46., 185
Polyethylene glycol		96°C	Ataman, <i>Colloid Polym. Sci.</i> , 1987 , 265., 19
Poly-2-ethylloxazoline		65°C	Chen <i>et al.</i> , <i>Macromol.</i> , 1990 , 23., 4688
Hydroxypropyl-cellulose		44°C	Winnik, <i>Macromol.</i> , 1987 , 20., 2745

Response to pH is another widely found stimulus, that originates from the electrostatic repulsion between charged groups within the polymer. At high pH, polyacrylates show enhanced swelling, whereas polyamines exhibit the same behavior at low pH.^[15] Considering the different pHs in the digestive organs, pH responsive hydrogels found application in drug delivery.^[16–19]

The response to irradiation with light can be assigned to an effect of either LCST or osmotic pressure. In the case of polymers modified with leuco derivatives, UV-light creates ion pairs (see fig. 1.3), causing a swelling due to the increase in osmotic pressure.^[20] When functionalized with chlorophyll, visible or IR light is transformed to local heat resulting in a collapse of the hydrogel.^[21] Light can be used as very defined stimulus which led to the application of these hydrogels in microfluidics.

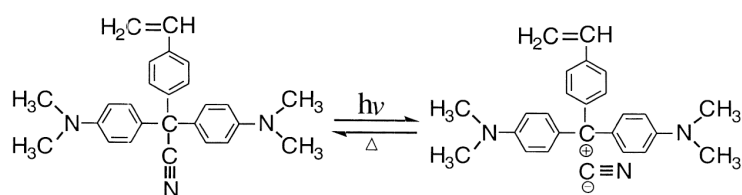


Fig. 1.3: Polymerizable leuco derivative splitting into an ion pair upon UV irradiation. ^[20]

The collapse can be triggered by an electric signal as well, as the movement of ions in the electric field results in an osmotic gradient from cathode to anode.^[22–24] At low ionic strength or in the absence of ions, shrinkage can be forced by electroosmosis and electrophoresis.^[25] Electro sensitive hydrogels can be applied as actuators and are a step forward towards the development of artificial muscles.^[26,27]

Finally, specifically modified hydrogels can undergo swelling or collapse upon a chemical stimulus. For example, an interpenetrating network formed by one polymer functionalized with an antibody and another with the respective antigen will swell upon addition of free antigen and thus indicate its presence (see fig. 1.4).^[28] Applied for controlled insulin delivery, a polymer with attached concanavalin A and glucose responds to an increase of glucose in solution by swelling and releasing insulin.^[29–31]

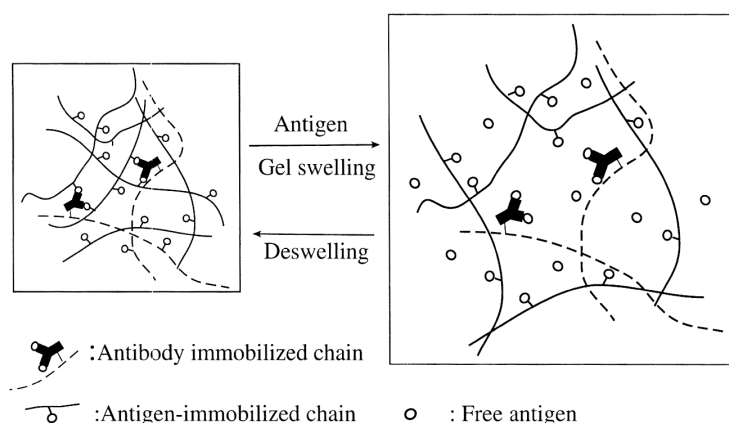


Fig. 1.4: Antigen-antibody interpenetrating network responding to free antigen.^[28]

Beside the introduction of responsive segments in the polymer chain, polymers that allow for further functionalization, so called functional hydrogels provide access to an even larger range of applications.

1.1.2 Functional Hydrogels

Functional hydrogels consist of at least one polymer segment that enables polymer analogous reactions. The possible routes utilize active ester chemistry, click chemistry, polymeric anhydrides, epoxides, aldehydes and ketones. Including Michael-type and Friedel-Crafts reactions as well as methylations, polymer analogous reactions involve almost all high yield organic reactions.^[32–34] Furthermore, for most of these transformations, both reaction partners are polymerizable or can be provided by functionalization of a precursor polymer. For example PHEMA can be transformed into a carboxylate with cyclic anhydrides and carbamates.

These reactive sites allow for the modification with a variety of biomolecules for biosensor applications and chromatography based on affinity binding.^[35–39] Additionally, attaching molecular recognition sites diversified cell culturing,^[40] and polymer assisted drug delivery advanced medication.^[8] As mentioned above, responsive behavior can be implemented to create a functional responsive hydrogel or to diversify the responsiveness, i.e. to a magnetic field by incorporating magnetite nanoparticles.^[41,42]

The combination of functionality and responsive behavior allows for the development of advanced biosensors. The concept is described in figure 1.5 in section 1.2.

1.1.3 PNIPAAm-based Hydrogels

One of the most frequently used and studied responsive polymer and hydrogel is poly-*N*-isopropylacrylamide (PNIPAAm).^[43] It is temperature sensitive, with a sharp phase transition at 33°C, its LCST. This is caused by the fine balance between the hydrophilic amide and the hydrophobic backbone and isopropyl group. The latter are responsible for the hydrophobic effect, the orientation of water molecules around nonpolar regions, resulting in a negative mixing entropy ΔS_{mix} . Meanwhile, the mixing enthalpy ΔH_{mix} is negative due to hydrogen bonding of the water with the amide group. According to the definition of the free Gibbs energy

$$\Delta G_{mix} = \Delta H_{mix} - T\Delta S_{mix} \quad (1.1)$$

raising the temperature above a certain value leads to a positive ΔG_{mix} , causing demixing. Indeed, above the LCST the polymer turns from coil to globule, causing the hydrogel to undergo phase separation and collapse.

The collapse temperature and kinetics, as well as the degree of volume change, can be influenced to a certain extent by copolymerizing other monomers, grafting and crosslinking.^[44–48] However, PNIPAAm loses its temperature sensitivity when too many comonomers are introduced.

The applications found for PNIPAAm-based hydrogels comprise most of those typically for temperature responsive hydrogels. Some are presented in chapter 7.

1.2 Biosensors

According to IUPAC, a biosensor is a 'device that uses specific biochemical reactions mediated by isolated enzymes, immunosystems, tissues, organelles or whole cells to detect chemical compounds usually by electric, thermal, or optical signals.'^[49]

Two representative examples will be introduced in the following.

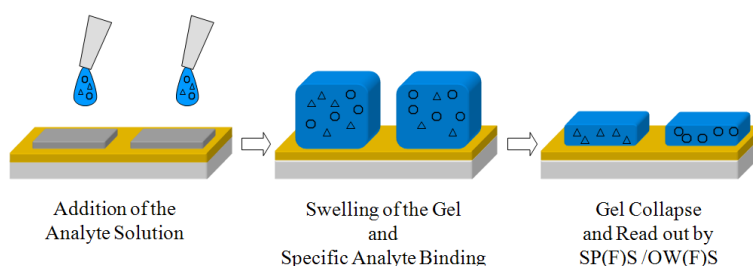


Fig. 1.5: Sensor concept with a functional responsive hydrogel.

The first is based on the optical recognition of binding events inside a sensor matrix. As depicted in figure 1.5, a hydrogel can act as such a matrix being the solid support for one partner of an affinity binding pair, e.g. an antigen. It might even host an array of different interaction schemes, as indicated by the two gel patches. Upon addition of the analyte solution, i.e. an antibody, the network swells and offers specific binding sites for the analytes. Unbound specimen are washed out and by exceeding the LCST the gel collapses, thus providing a higher analyte concentration in the detection area. The optical recognition can be conducted by measuring the change in refractive index by surface plasmon resonance (SPR) or optical waveguide mode spectroscopy (OWS), for example. For fluorescent or dye-labeled analytes, SPR or OWS excited fluorescence spectroscopy (SPFS/OWFS) can be utilized to determine the amount of analyte.

Important parameters of such a biosensor matrix are stability – i.e. prevention of unspecific adsorption – accessibility by means of large enough pore size, and optical properties enabling optical measurements. The employment of a hydrogel as biosensor matrix is demonstrated in section 7.1.

The second representative example employs electrochemical investigation methods to probe an analyte solution. The most sensitive and selective biosensors are probably found in nature, integrated into cell membranes. There, receptors trigger signal transduction through the membrane, for example by influencing the ion transport of channels. Artificial biomembranes attached to an electrode with incorporated proteins or engineered channels merge nature's sensing systems with a physicochemical transducer.^[50] However, these artificial environments have to meet a number of criteria to effectively mimic a natural cell membrane. First of all, they have to allow for the functional incorporation of the proteins, but excellent sealing qualities and a long term stability are required to reliably monitor the response of the receptor.

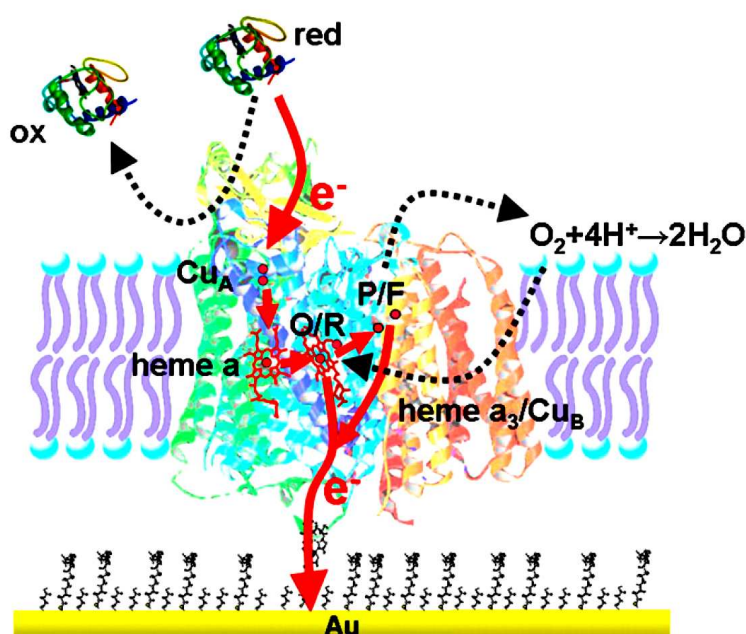


Fig. 1.6: A protein tethered bilayer lipid membrane (ptBLM) enabling the electrochemical detection of cytochrome C (cyt c) via the protein cytochrome C oxidase (CcO).^[51]

One class of artificial biomembranes are so called protein tethered bilayer lipid membranes (ptBLM), illustrated in figure 1.6. They consist of proteins tethered to a surface via a spacer and a lipid bilayer span between the proteins by the self-assembly of phospholipids. The spacer decouples the protein from the influence of the substrate and forming an ion reservoir to avoid the denaturing of the proteins. Moreover, the lipids are stabilizing the proteins and enabling electrochemical measurements by separating the electrode from the outer membrane environment. In the presented case, cytochrome C (cyt c) can be detected by the current resulting from its oxidation by the ‘receptor’ cytochrome C oxidase (CcO).^[51]

1.3 Bio-Compatibility and Non-Fouling

Although the biological reaction of organisms to foreign bodies is being investigated for decades^[52] and ship hull fouling is known since the beginning of navigation, the nature of the interactions with biomolecules and complete organisms is largely unknown. Lately, the development of biosensors urged the engagement with their major problem of unspecific adsorption, often referred to as (bio)fouling.^[53]

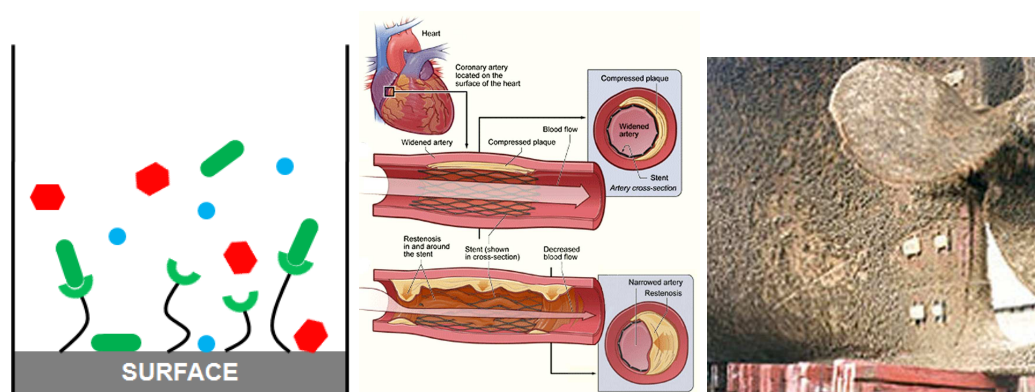


Fig. 1.7: Left: unspecific adsorption to a sensor surface.(adapted from polyintell) Middle: stent restenosis.(nhlbi.nih.gov) Right: ship hull fouling.(BASF)

To prevent or at least reduce unspecific adsorption, several strategies were employed, taking into account the limitations and requirements of the field of application. For biosensor applications only few reliable coatings are known. Sensing devices in diagnostic practice mainly resort to PEG coatings, though PNIPAAm, dextran and recently polymers containing zwitterionic groups, like phosphorylcholine, sulfobetaine, and carboxybetaine to mimic cell membranes are employed as well.^[36]

For soft tissue implants, medical scientists rely on inert materials like stainless steel, titanium and cobalt/chromium alloys for artery stents or silicone and teflon for augmentation mammoplasty and artificial cardiac valves. These materials are often combined with polymers eluting drugs to prevent inflammatory reactions. However, restenosis, the choking of stents and encapsulation or rejection of implants, caused by the stents material or even the eluted drug currently still are a major problem.^[54]

Similar to drug eluting implants, ship owners use so called antifouling paintings on the hull of their vessels to reduce the attachment of marine organisms. These coatings elute tin-organic, copper or zinc-organic compounds or organic cytotoxins. The latter are found in herbicides and fungicides as well. Due to the baneful side effects on the marine life and its high persistency in the food chain, the most commonly used ingredient tributyltin was banned by the International Maritime Organization (imo.org) in 2008. One possibility to replace these coatings might be to adapt the principles of reducing unspecific adsorption on sensors and implants.

On the other hand, for some applications, the adsorption of cells is desirable, or proteins and polysaccharides which can act as adhesion promoter for them, i.e. for ossific fillers in bone implant coatings.^[55] In engineering cell tissue replace-

ment, even surfaces that enable switching between bioadsorption and repulsion are employed to release tissue from the dish after growth.^[56] Taking into account the need of coatings which prevent the proliferation of cells on them, but at the same time do not cause inflammatory reactions, the demand for biocompatible materials that can be adapted to the corresponding application rises.

This topic is highly complex as the efficiency of the coated material differs from tissue to tissue. When nonfouling properties are needed, an implant coating suitable for bladder catheter might be unsuitable for ophthalmic stents and in the case of tissue engineering, the necessities of tissues from bone and liver differ as well. A recent introduction to materials used in medicine was published by Ratner and coeditors.^[57]

1.4 Aim and Outline of the Thesis

The aim of this thesis is the synthesis and characterization of a functional hydrogel with the scope of exploitation as matrix for biosensing and as coating for medical applications.

Its utilization requires the understanding of the relevant properties of the applied hydrogel and the exploration of its interplay with biomaterials. To ascribe these interaction to its properties, thorough investigations regarding their optical, mechanical and chemical nature have to be conducted. For these studies, it is necessary to adapt existing or develop new methods to study the synthesized hydrogels. A complete characterization furthermore allows for a future comparison with other materials employed in the field of application.

It was decided to employ a hydrogel based on an initially non-crosslinked polymer, which allows for subsequent transformation to a hydrogel network. This approach and the possibility to accurately control the crosslinking density grants tunability and a high reproducibility of the properties of the used hydrogel. To gain functionality, a protocol had to be established to modify copolymerized methacrylic acid, based on active ester chemistry. The corresponding compounds had to be synthesized. A diversification of characteristics can be achieved by implementing responsiveness to external stimuli. Hence, the polymer investigated and employed for the preparation of the hydrogel was chosen to mainly consist of PNIPAAm, with a LCST of $\sim 32^{\circ}\text{C}$.

The procedure developed to obtain a functional hydrogel is presented and discussed in chapter 3, 'Preparation of the Hydrogel'. These syntheses are the basis of the research performed in the following chapters.

The first step towards a systematic characterization of the hydrogel is studying the underlying polymer. Beside its molecular weight and molecular weight distribution (see section 3.1), its chemical composition was determined by a specifically developed $^1\text{H-NMR}$ protocol to reveal and distinguish the different structural components. For the analysis of the composition of the respective grafted and crosslinked hydrogel, X-ray photoelectron spectroscopy was employed in chapter 4, 'Chemical Characterization'.

An investigation on the optical properties of the gel, like swelling state with respect to environmental changes, was conducted based on surface plasmon and waveguide mode spectroscopy in chapter 5, 'Optical Characterization'. Section 5.1 introduces the spectroscopy of coupled long range surface plasmons which was developed lately for a more reliable investigation of very thin films.

In section 5.2, the combination of plasmon and waveguide mode spectroscopy (SPR/OWS) was utilized. The complex data were evaluated with the help of the Wentzel-Kramers-Brillouin-approximation, which enables studying structural gradients in thin films perpendicular to the substrate.

In the subsequent chapter 6 'Dynamic Characterization', the diffusion of tracking probes as well as the dynamics of the gel itself are studied. To follow the movement of diffusants inside the hydrogel, fluorescence correlation spectroscopy and SPR/OWS were employed. In addition, a synthetical approach to enhance FCS and the usage of PCS were commenced and the synthesis of new probes was initiated. The motion of the grafted and crosslinked network itself was studied with PCS. These investigations shed light on the mechanical and structural properties of the hydrogel.

These methods give information, which are important for the application of the hydrogel as sensor matrix. They allow for the determination of the mesh size and the proper motion of the host, which is necessary to understand the performance as sensor platform.

Section 7.1 introduces the hydrogel as biosensor matrix, using SPR/OWS as signal transducer.

The application of the hydrogel as medical coating is presented in the subsequent section. Its interaction with cells is investigated, to enable employing the hydrogel for the coating of intraocular stents.

The results of the research performed on the interaction with biomaterial for medical coatings are likewise of interest for sensor application as unspecific adsorption reduces the efficiency of the biosensor.

In the last section, a hydrogel with a higher degree of functionality is introduced. The gel presented before was adapted to meet the requirements to support a protein tethered bilayer lipid membrane. Therefore, the employed polymer consists only of a functional monomer and the photo crosslinker.

Thus, this thesis spans the whole range from design and synthesis, via characterization to the application of functional hydrogels.

The section 5.1, 'Coupled Long Range Surface Plasmon (cLRSP) Spectroscopy' was published in

[58]J. Dostálek, R. F. Roskamp and W. Knoll, *Sensors and Actuators B: Chemical*, **2009**, *139*, 9-12, Coupled long range surface plasmons for the investigation of thin films and interfaces.

Sections 6.1.2, 'FCS of Rhodamine 6G Diffusion' and 6.3.2, 'FCS of Dye-labeled Hydrogel' were published in

[59]M. Gianneli, P. W. Beines, R. F. Roskamp, K. Koynov, G. Fytas and W. Knoll, *Journal of Physical Chemistry C*, **2007**, *111*, 13205-13211, Local and Global Dynamics of Transient Polymer Networks and Swollen Gels Anchored on Solid Surfaces.

The section 6.3.3, ' μ PCS of the Hydrogel' was published in

[60]M. Gianneli, R. F. Roskamp, U. Jonas, B. Loppinet, G. Fytas and W. Knoll, *Soft Matter*, **2008**, *4*(7), 1443-1447, Dynamics of swollen gel layers anchored to solid surfaces.

The application as 'Biosensor Matrix' in section 7.1 was published in

[61]A. Aulasevich, R. F. Roskamp, U. Jonas, B. Menges, J. Dostálek and W. Knoll, *Macromolecular Rapid Communications*, **2009**, *30*, 872-877, Optical Waveguide Spectroscopy for the Investigation of Protein-Functionalized Hydrogel Films.

Section 7.3, 'Protein-resistant Coatings: A ToF-SIMS Study' is prepared to be submitted to *Biomaterials*

R. F. Roskamp, C. R. van den Brom, U. Jonas, M. Jasieniak and H. J. Griesser, A collapsed Non-Fouling PNIPAAm-based Hydrogel.

Section 7.4, 'A Hydrogel-supported ptBLM' is prepared to be submitted to *Soft Matter*

A. Kibrom, R. F. Roskamp, U. Jonas, B. Menges and R. L. C. Naumann, Hydrogel-supported Protein-tethered Bilayer Lipid Membranes: a new approach towards polymer-supported Lipid Membranes.

2 Methods

2.1 Contact Angle Measurement

Contact angle measurements are one of the easiest methods to investigate a solid surface, particularly to obtain information on tension and roughness. The contact angle is determined at the interface between the three phases, liquid, solid, and vapor, of a liquid droplet placed on the solid surface of interest. The thermodynamic equilibrium of such a system is described by the Young-equation:

$$\gamma_s = \gamma_{sl} + \gamma_l \cos \Theta \quad (2.1)$$

Equation 2.1:

γ_s - surface tension (solid); γ_{sl} - interfacial tension (solid/liquid); γ_l - surface tension (liquid); Θ - equilibrium contact angle.

The contact angle is, in the first, determined by the hydrophilic property of the surface.



Fig. 2.1: Contact angle of a water droplet on an ultrahydrophobic (left), hydrophobic (center) and very hydrophilic (right) surface.

Contact angles can cover a range from below 30° (very hydrophilic) to 90° (hydrophobic) and up to 180° (ultrahydrophobic) surfaces, as illustrated in figure 2.1. On a very hydrophilic substrate, the droplet can spread completely. Among several other methods to measure a contact angle, only the static contact angle in 'Sessile-Drop'-mode is determined here. The system applied is the Drop Shape Analysis System DSA 10 (Kruess, Germany) with a thermo stage and degassed

MilliQ (ultra pure water, > 18.2 MΩ cm, 2.5 μL droplets). To avoid effects of evaporation, evaluation was performed on the basis of pictures taken right after placing the droplet. At least four measurements were carried out on each surface and evaluated by commercially available software. (SCA202, V.3.7.4., DataPhysics Instruments, Germany)

2.2 Surface Plasmon Resonance Spectroscopy (SPR)

Surface plasmon resonance spectroscopy (SPR) was designed for the nondestructive investigation of the optical properties of ultra thin films at metal surfaces and incidents close to the metal-dielectric interface. The spectroscopy of surface plasmons is based on the attenuation of total internal reflection (ATR).

If light hits the interface of two media with different optical density, going from the denser n_1 (e.g. glass) to the thinner n_2 (e.g. water), one part is reflected with the same angle $\Theta_r = \Theta_i$ as the incident wave. The other part is refracted following Snell's law as depicted in figure 2.2.

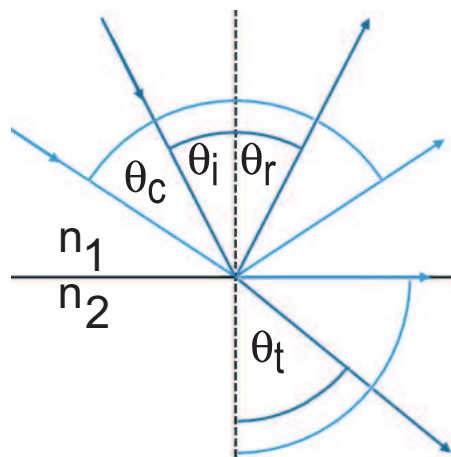


Fig. 2.2: Reflection and refraction at an interface according to Snellius.

$$\sin \Theta_t = \frac{n_1}{n_2} \sin \Theta_i \quad (2.2)$$

Equation 2.2:

Θ_t - emergent angle of the transmitted wave; n_1 - refractive index of the optically denser media; n_2 - refractive index of the optically thinner media; Θ_i - incidence angle of the incident wave.

From eq. 2.2 one can derive the critical angle of total internal reflection (TIR) Θ_c with $\Theta_t = 90^\circ$. The relations between the fields of the incident and the reflected and transmitted wave were described by Fresnel:

$$r_s = \frac{n_2 \cos\Theta_i - n_1 \cos\Theta_t}{n_2 \cos\Theta_i + n_1 \cos\Theta_t}$$

$$r_p = \frac{n_2 \cos\Theta_t - n_1 \cos\Theta_i}{n_2 \cos\Theta_t + n_1 \cos\Theta_i}$$

$$t_s = \frac{2n_1 \cos\Theta_i}{n_2 \cos\Theta_i + n_1 \cos\Theta_t}$$

$$t_p = \frac{2n_1 \cos\Theta_t}{n_2 \cos\Theta_i + n_1 \cos\Theta_i}$$

Equation 2.3:

r_s - reflection ratio for s-polarized light; r_p - reflection ratio for p-polarized light; t_s transmission ratio s-polarized light; t_p transmission ratio for p-polarized light.

Above TIR, the incident light gives rise to a wave restricted to the surface with an evanescent (exponential) decaying intensity along and perpendicular to the interface. The penetration depth of the evanescent wave ($\frac{I}{I_0} = \frac{1}{e}$) is given by:

$$d_{\frac{1}{e}} = \frac{\lambda}{2\pi} \left[\frac{n_1^2}{n_2^2} \sin^2 \Theta_i - 1 \right]^{-\frac{1}{2}} \quad (2.3)$$

Equation 2.3:

$d_{\frac{1}{e}}$ - penetration depth; λ - wavelength of the light; n_1 - refractive index of the denser media; n_2 - refractive index of the thinner media; Θ_i - angle of the incident wave.

Changes in the refractive index in the field of the evanescent wave by a layer that absorbs energy from the wave lead to corresponding changes in the intensity of the reflected light, according to eq. 2.3. In the case of a glass surface, the field is that weak, that it is commonly enhanced taking advantage of the excitation of surface plasmons.^[62-64] This is enabled by coating the interface with a thin metal, typically gold or silver. P- or T_M -polarized light, which has an electric field component perpendicular to the interface, can induce surface charges in the free electron gas and hence generate surface plasmons. Furthermore, plasmons allow for the detection of layers that do not absorb energy from the evanescent wave.

2 Methods

To probe the resonance between the light wave and the plasmon, both have to have the same wave vector, given for the plasmon as:

$$k_{x,plasmon} = \frac{\omega}{c} \sqrt{\frac{\epsilon_m \epsilon_d}{\epsilon_m + \epsilon_d}} \quad (2.4)$$

Equation 2.4:

$k_{x,plasmon}$ - wave vector of the plasmon in x direction; ω - angular frequency; ϵ_m - dielectric constant of the metal; ϵ_d - dielectric constant of the dielectric; c - speed of light.

derived from Maxwells equations. The wave vector of the plasmon will always exceed the wave vector of light in air, hence the metal has to be coated on a denser medium like glass (e.g. a prism). One possible realization is the Kretschmann-configuration (see fig. 2.3).^[65]

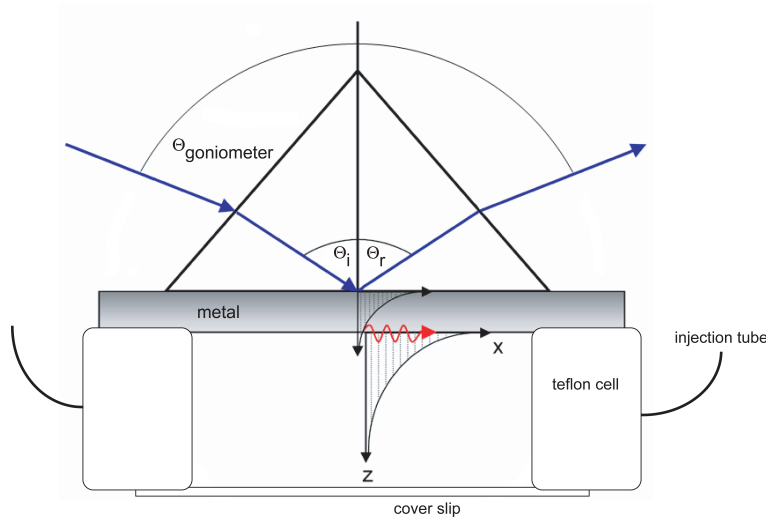


Fig. 2.3: Kretschmann-configuration mounted on a teflon cell with injection tubes.

Using a prism, the wavevector of the incident light

$$k_{x,photon} = \frac{\omega}{c} \sqrt{\epsilon_{prism}} \sin \Theta_i \quad (2.5)$$

Equation 2.5:

$k_{x,photon}$ - wavevector of the photon in x direction; ω - angular frequency; ϵ_{prism} - dielectric constant of the prism; c - speed of light; Θ_i - angle of the incident wave.

depends on the angle of incidence Θ_i , allowing for an increase of k_x to gain resonance with the plasmon for a given angular frequency of the laser ω_{laser} (see fig. 2.4).

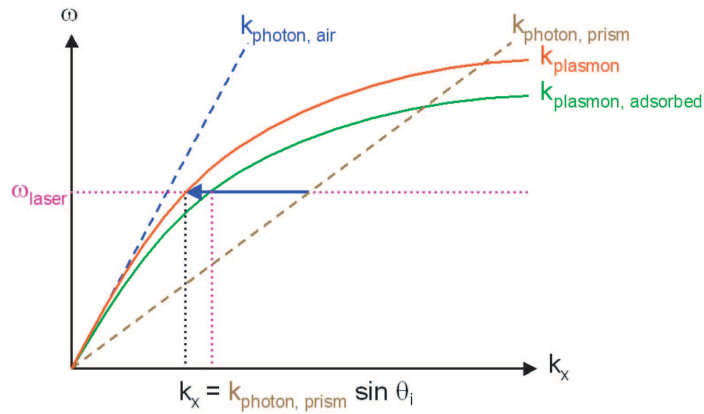


Fig. 2.4: Dispersion relations of photons in air and prism, and of plasmons with different media on top of the interface.

Hence, upon changing the incident angle, the reflected intensity runs through the resonance minimum after passing the angle of total internal reflection (see fig. 2.5). SPR is therefore described as attenuated total internal reflection method.

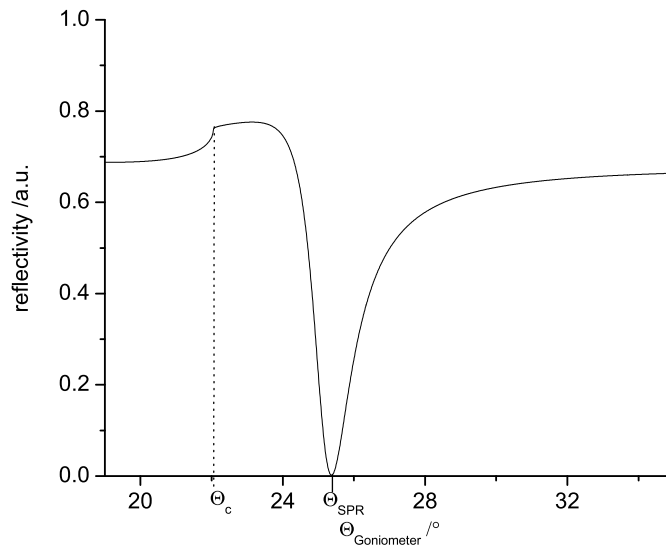


Fig. 2.5: Simulated reflectivity spectra of gold against air.

The adsorption of molecules on the gold, or any change in the refractive index in the field of the plasmon, changes the wave vector of the plasmon (see fig. 2.4) and the resonance angle Θ_{SPR} , respectively.

This shift is proportional to the dielectric constant and the thickness of the adsorbed layer following

$$\Delta\Theta_i \sim (\sqrt{\epsilon_d} - \sqrt{\epsilon_p}) d \quad (2.6)$$

with

$$\epsilon = (n + ik)^2 = n^2 + 2ikn - k^2 = \epsilon' + i\epsilon'' \quad (2.7)$$

Equations 2.6 and 2.7:

Θ_i - angle of incidence; ϵ_d - complex dielectric constant of the dielectric; ϵ_p - complex dielectric constant of the buffer; d - thickness of the adsorbed layer; n - real part of the refractive index; k - imaginary part of the refractive index; ϵ' - real part of the dielectric constant ($\epsilon' = n^2 - k^2$); ϵ'' - imaginary part of the dielectric constant ($\epsilon'' = 2kn$).

This allows for the determination of the optic properties and the thickness of the adsorbed layer.^[66] The shift can be followed in scan and kinetic mode. The scan mode requires a repeated measurement of angular dependent reflectivity spectra as depicted in figure 2.6.

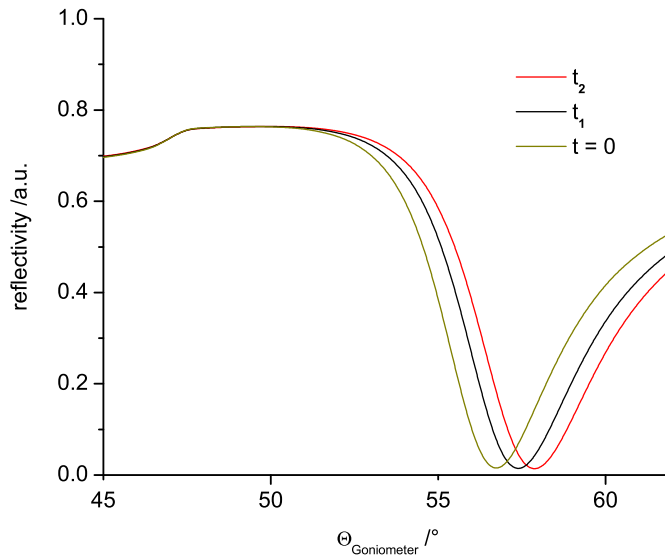


Fig. 2.6: Simulated changes in reflectivity spectra for the adsorption from solution with time.

The kinetic mode measures the change of reflected intensity with time at a fixed angle Θ_K in the linear part of the flank of the minimum (see fig. 2.7). A shift of the resonance angle alters the reflectivity at the chosen angle. This method is much faster than a full angular scan and thus allows for recording of adsorption kinetics.

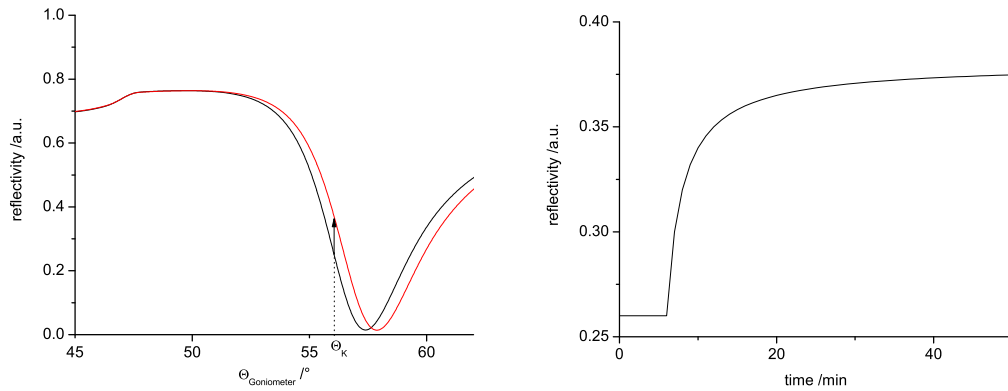


Fig. 2.7: Simulated reflectivity spectra at a certain time (left) and a fixed angle Θ_K (right).

Figure 2.8 shows the schematic construction of the applied SPR setup with a measurement cell as depicted earlier (see fig. 2.3).

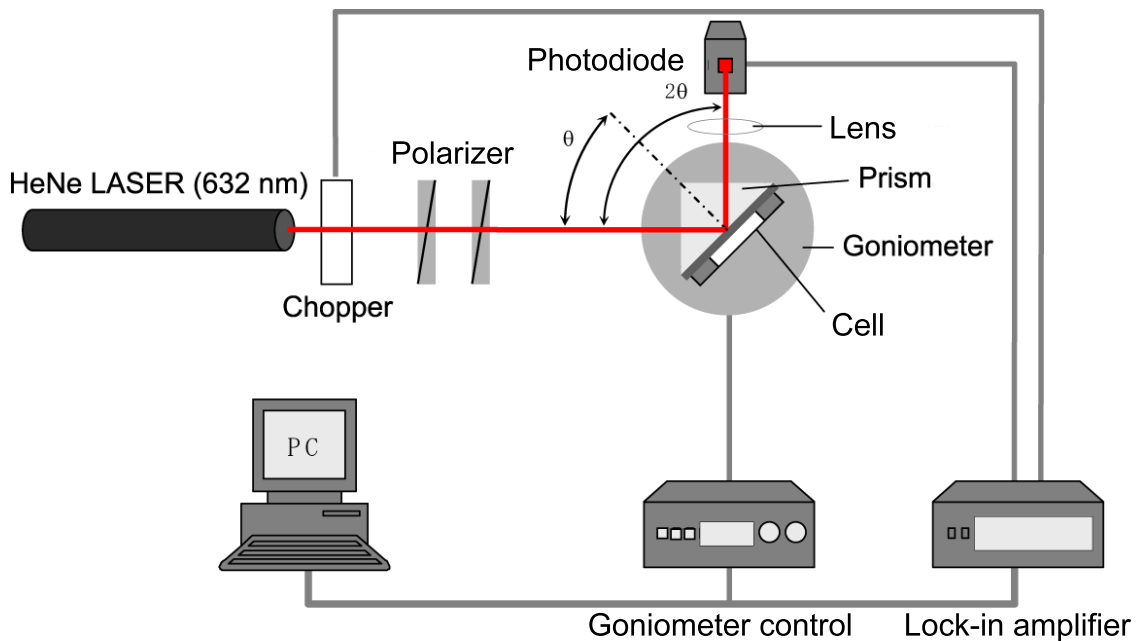


Fig. 2.8: Schematic SPR-setup.

However, SPR requires the knowledge of either the refractive index or the thickness to determine the respective other parameter. To overcome this disadvantage coupled long range surface plasmons (section 5.1) or a combination of SPR and waveguide mode spectroscopy is applied.

2.3 Optical Waveguide Mode Spectroscopy (OWS)

The principle of TIR is used to guide lightwaves in confined media, as well. Assuming a model waveguide consisting of three layers with refractive indices n_1 , n_2 and n_3 , for the case of $n_2 > n_1, n_3$ layer 2 can guide lightwaves (see fig. 2.9). For angles larger than the critical angle of TIR θ_c of both interfaces, the wave can not escape the layer anymore, it is guided. From ray optics one can derive that only waveguide modes of discrete angles or corresponding wavelengths can exist, as the interference after two reflections has to be constructive. A more adequate description of this phenomena and the fact, that the beam is not completely reflected at the interface, but exhibit a decaying field outside the waveguide, can be found in wave optics theory.^[67-69]

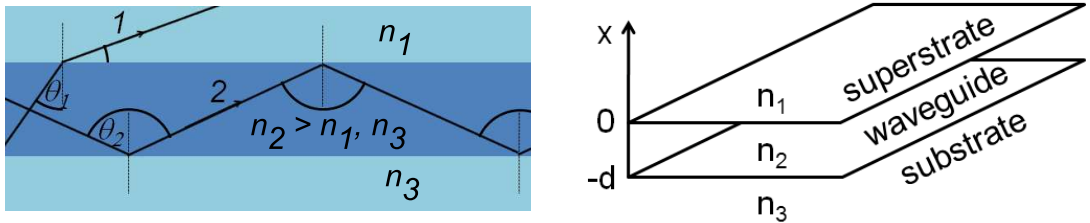


Fig. 2.9: Waveguide with a refractive index $n_2 > n_1, n_3$, the indices of the surrounding layers and the guided beam 2 with and incident angle $\theta_2 > \theta_c$, the critical angle of TIR and the non-guided beam 1 with $\theta_1 < \theta_c$.

Starting from the Maxwell equations

$$\begin{aligned} \nabla \times \vec{E} &= -\frac{\partial \vec{B}}{\partial t} & \nabla \cdot B &= 0 \\ \nabla \times \vec{H} &= \frac{\partial \vec{D}}{\partial t} & \nabla \cdot D &= 0 \end{aligned} \tag{2.8}$$

Equation 2.8:

\vec{E} - the electric field; \vec{B} - the magnetic field; \vec{H} - the magnetic field strength; \vec{D} - the electric displacement.

one obtains two groups of solutions. Transversal electric (T_E) modes with a polarization of the electric field perpendicular to the plane of incidence and transversal magnetic (T_M) modes with a polarization of the electric field parallel to the plane of incidence. As SPR can only be performed with p-polarized light, having an

electric field parallel to the propagation direction, and we are particularly interested in the combined use of SPR and OWS, here only the T_M modes with T_{M0} , the surface plasmon are discussed.

Using the following approach for the wavefunctions in the three media

$$\begin{aligned} H_{y1} &= A \exp(vx) \\ H_{y2} &= B \cos(ux) + C \sin(ux) \\ H_{y3} &= D \exp(-wx) \end{aligned} \quad (2.9)$$

Equation 2.9:

$$v = \sqrt{-k_0^2 n_1^2 + \beta^2}; u = \sqrt{k_0^2 n_2^2 - \beta^2}; w = \sqrt{-k_0^2 n_3^2 + \beta^2}; k_0 - \text{wavenumber in vacuum}; \beta - \text{propagation constant.}$$

one can derive the dispersion relation

$$\tan ud = \frac{\frac{u}{n_2^2} \left(\frac{v}{n_1^2} + \frac{w}{n_3^2} \right)}{\frac{u^2}{n_2^4} - \frac{v}{n_1^2} \frac{w}{n_3^2}} \quad (2.10)$$

and finally the wavefunctions:

$$\begin{aligned} H_{y1} &= -\frac{u}{n_2^2/n_1^2 v} C \exp(vx) \\ H_{y2} &= C \left(-\frac{u}{n_2^2/n_1^2 v} \cos(ux) + \sin(ux) \right) \\ H_{y3} &= -C \left(\frac{u}{n_2^2/n_1^2 v} \cos(ud) + \sin(ud) \right) \exp(w(x+p)) \end{aligned} \quad (2.11)$$

The dispersion relation is only solvable for discrete β , allowing only discrete wavelengths with a wave vector $k_x = \sqrt{k_0^2 n^2 - \beta^2}$ as described in the particle optics part. For a real k_x , the guided wave propagates in x direction, for an imaginary k_x , the wave is evanescent.

However, this description is not completely true for the waveguide discussed in this thesis. Here the substrate with the lower refractive index is a gold layer, far too thin to allow for the complete evanescent decay of the wavefunction. The

wave guided between gold and buffer or air, is referred to in literature as leaky mode. A neat description of the phenomena can be supplied by a quantum mechanical approach. For a closed expansion ('normal') waveguide, the sub- and superstrate of lower refractive index can be treated as potential walls of finite height and infinite width. The solution of the Schrödinger equation is the same as described above by wave optics theory, with an evanescent solution in the walls and an oscillating wave in between. For a leaky mode expansion, the gold substrate can be treated as potential wall of finite height and finite width. This gives rise to the possibility of reflection by anti-tunneling and the coupling into and out of the waveguide by tunneling. A complete description can be found in literature,^[70,71] here it is only stated, that guiding leaky waves is possible and that the coupling efficiency – the depth of the modes – depends on the thickness of the gold layer (see fig. 2.10), as intuitively assumed.

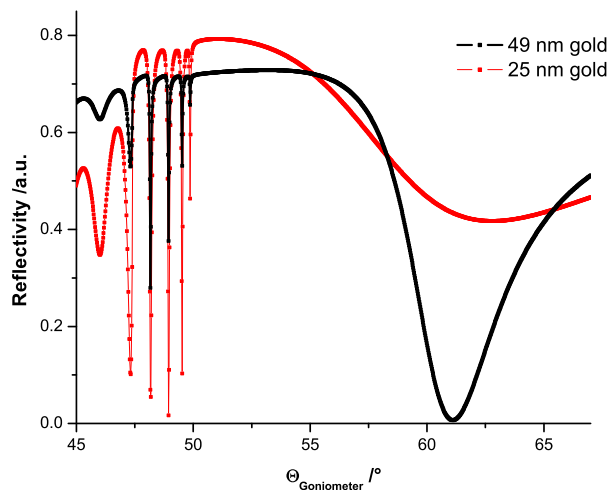


Fig. 2.10: Increasing coupling efficiency with decreasing gold layer thickness.

2.3.1 Wentzel-Kramers-Brillouin (WKB)-Approximation

Additionally to the waveguides with uniform refractive index discussed above, such with a gradient in refractive index can be found or are desirable to produce. For some gradients, the exact solution can be calculated and is known from literature,^[69] for those with an inhomogeneous gradient, however, only approximations can be applied. One is the Wentzel-Kramers-Brillouin (WKB)-approximation, which is discussed briefly in the following. A detailed derivation can be found in literature.^[67,69]

To solve the scalar wavefunction, after the addition of a x-dependency of the refractive index

$$\frac{\partial^2 H_y}{\partial x^2} + (k_0^2 n^2(x) - \beta^2) H_y = 0 \quad (2.12)$$

the approach

$$H_y = H_0 \exp(ik_0 U(x)) \quad (2.13)$$

is expanded in series. By summarizing the terms of the same order, the zeroth and first order of the WKB-approximation.

$$U_0 = 1/k_0 \int \sqrt{k_0^2 n^2(x) - \beta^2} dx \quad (2.14)$$

$$U_1 = i/2 \ln \left| \frac{dU_0}{dx} \right| \quad (2.15)$$

The zeroth order results in two solutions, an oscillating

$$H_y = \frac{H_0}{\sqrt[4]{k_0^2 n^2(x) - \beta^2}} \exp\left(\pm i \int \sqrt{k_0^2 n^2(x) - \beta^2} dx\right) \quad (2.16)$$

and an evanescent

$$H_y = \frac{H_0}{\sqrt[4]{\beta^2 - k_0^2 n^2(x)}} \exp\left(\pm \int \sqrt{\beta^2 - k_0^2 n^2(x)} dx\right) \quad (2.17)$$

for $k_0^2 n^2(x) < \beta^2$. At the point of discontinuity the one solution merges into the other (after connecting linearly). This transition point (x_t) is at the same time the integration limit for eq. 2.16, introducing the effective refractive index sensed by

the mode:

$$\int_0^{x_i} \sqrt{n^2(x) - n_{eff}^2} dx = \lambda_0/2(N + 3/4) \quad (2.18)$$

with $N = 0, 1, 2, \dots, n_2 - n_1 \ll n_1$.

Practically, with a n_{eff} given by the measured incident angle:

$$n_{eff} = n_p \sin \left(\gamma + \arcsin \left(\frac{\sin \Theta}{n_p} \right) \right) \quad (2.19)$$

Equation 2.19:

n_p - refractive index of the prism; γ - prism angle; Θ - angle of incidence.

$n^2(x)$ can be approximated according to

$$n^2(x) = n_{eff,k}^2 + \frac{n_{eff,k-1}^2 - n_{eff,k}^2}{x_k - x_{k-1}} (x_k - x) \quad (2.20)$$

with $x_{k-1} \leq x \leq x_k$ and $k = 1, 2, 3, \dots, m$.

Together with eq. 2.18, the measured refractive index n_{eff} can be assigned to a distance from the substrate by a recursive procedure:

$$\begin{aligned} \frac{x_m - x_{m-1}}{\lambda_0} = & \frac{1}{\sqrt{n_{eff,m-1}^2 - n_{eff,m}^2}} \left(\frac{3(4m-1)}{16} - \sum_{k=1}^{m-1} \frac{x_k - x_{k-1}}{\lambda_0(n_{eff,k-1}^2 - n_{eff,k}^2)} \right) \\ & \times [(n_{eff,k-1}^2 - n_{eff,m}^2)^{3/2} - (n_{eff,k}^2 - n_{eff,m}^2)^{3/2}] \end{aligned} \quad (2.21)$$

Due to the actual way of performing the WKB-approximation in the opposite direction it is often referred to as 'reversed WKB-approximation'.

2.4 Correlation Spectroscopy

Correlation spectroscopy is used to investigate and describe the fluctuations in light intensity $I(t)$, detected from scattering or confocal fluorescence experiments, as a function of time. When probing a hydrogel, these fluctuations can have their origin in the diffusion of tracking-probes through the network or the motion of the scattering host itself.^[72-75] The processing is done by a hardware autocorrelator which multiplies the time-dependent scattered intensity with itself, shifted by a distance τ in time. By averaging over the total measurement time $\langle I(t)I(t + \tau) \rangle$ one obtains the normalized intensity autocorrelation function:

$$G(\tau) = \frac{\langle I(t)I(t + \tau) \rangle}{\langle I(t)^2 \rangle} \quad (2.22)$$

as depicted in figure 2.11.

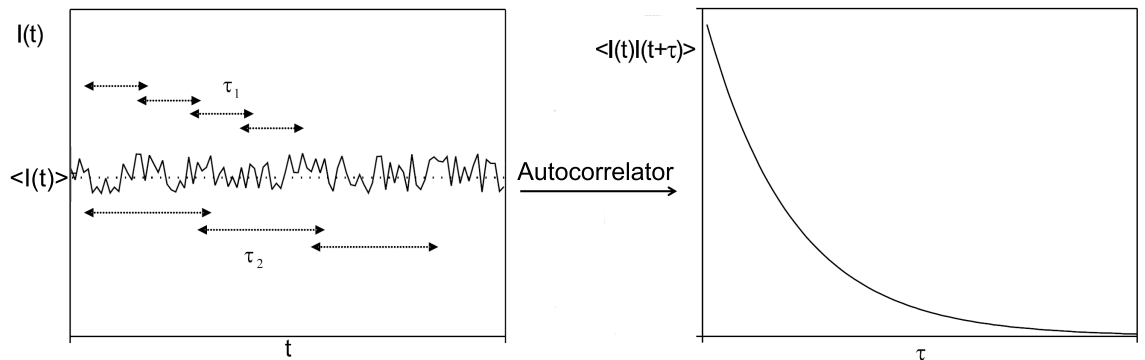


Fig. 2.11: Scattering intensity fluctuation around the mean $\langle I(t) \rangle$, processed by an autocorrelator giving the intensity autocorrelation function.

2.4.1 Fluorescence Correlation Spectroscopy (FCS)

Fluorescence correlation spectroscopy (FCS) is based on detecting the fluctuations of the fluorescent light intensity in a small observation volume V_{obs} , usually formed by the focus of a confocal microscope.^[76]

$$V_{obs}(x, y, z) = e^{-2((x^2+y^2)/r_0^2)} e^{-2(z^2/z_0^2)} \quad (2.23)$$

as depicted in figure 2.12.

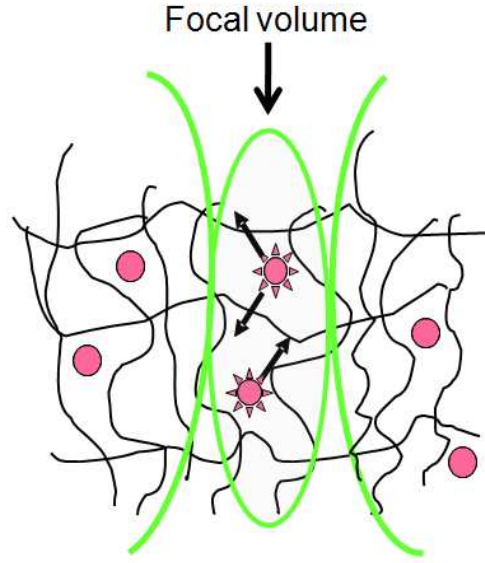


Fig. 2.12: Focal volume of a confocal FCS measuring the diffusion of the illuminated fluorophores (red) through a network.

The experimental autocorrelation function of the motions has the analytical form:

$$G(t) = \frac{1 + \frac{T}{1-T} e^{-t/\tau_T}}{N} \left(\sum_{i=1}^M \frac{F_i}{(1 + t/\tau_i) \sqrt{1 + t/(S^2\tau_i)}} \right) + 1 \quad (2.24)$$

Equation 2.24:

F_i - fractional population of the i^{th} component; T - triplet fraction; τ_T - triplet decay time; τ_i - characteristic diffusion time of the i^{th} fluorescent component with $\tau_i = r_0^2/4D_i$ with the self-diffusion coefficient D_i ; $S = z_0/r_0$ structural setup parameter.

As a result of very low fluorophore concentrations, FCS allows for the computation of the tracer mean square displacement $\langle \Delta r^2(t) \rangle$ in the observation volume V_{obs} with lateral and vertical dimensions of $r_0 = 0.2 \mu m$ and $z_0 = 0.8 \mu m$, respectively from the experimental autocorrelation function:

$$G(t) = N^{-1} [1 + (2/3) \langle \Delta r^2(t) \rangle / r_0^2]^{-1} \cdot [1 + (2/3) \langle \Delta r^2(t) \rangle / z_0^2]^{-1/2} + 1 \quad (2.25)$$

The normalized fluorescence intensity correlation function $C(t)$ is derived from the experimental autocorrelation function in eq. 2.24 as $C(t) = (G(t) - 1) N$.

The employed setup is described in literature.^[59]

2.4.2 Photon Correlation Spectroscopy (PCS)

Contrary to FCS, photon correlation spectroscopy (PCS) detects light scattered from inhomogeneities, like particles, in a volume illuminated by laser light.^[77] From dynamic light scattering, as well as static, one can obtain additional information, like structure parameter of the scatterer, when measuring at different angles. The scattering wave vector q (see fig. 2.13) is added to the normalized intensity autocorrelation function

$$G(q, \tau) = \frac{\langle I(q, t)I(q, t + \tau) \rangle}{\langle I(q, t)^2 \rangle} \quad (2.26)$$

with

$$q = \frac{4\pi n \sin(\theta/2)}{\lambda_0} \quad (2.27)$$

Equation 2.27:

n - the refractive index of the solution; θ - the scattering angle; λ_0 - the wavelength of the laser.

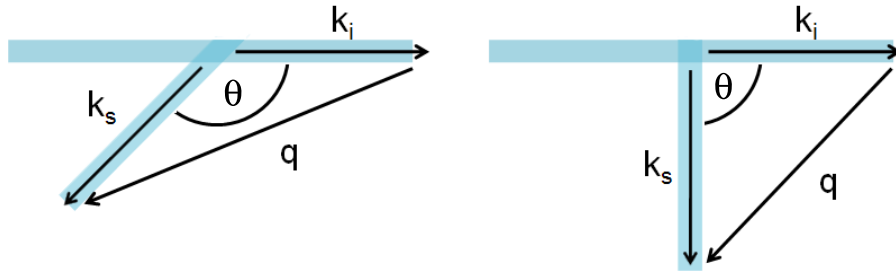


Fig. 2.13: Scattering wave vector q derived by $q = k_s - k_i$ with k_s and k_i the wave vectors of the scattered and the incident light, respectively.

The field autocorrelation function is calculated by:

$$C(q, \tau) = \sqrt{G(q, \tau) - 1} \quad (2.28)$$

known as Siegert relation. For a dilute solution of monodisperse polymers applies

$$C(q, \tau) = \alpha \exp(-q^2 \langle \Delta r^2(\tau) \rangle / 6) = \alpha \exp(-D_0 q^2 \tau) \quad (2.29)$$

Equation 2.29:

$\langle \Delta r^2(\tau) \rangle$ - the mean square displacement; $\alpha I(q)$ - the net intensity of the solute polymer.

From

$$D_0 = k_B T / 6\pi\eta_s R_h \quad (2.30)$$

Equation 2.30:

R_h - the hydrodynamic radius; k_B - the Boltzmann constant; η_s - the solvents shear viscosity.

one can derive the hydrodynamic radius R_h .

A description of the used setup can be found in literature.^[78]

2.5 X-ray Photoelectron Spectroscopy (XPS)

Typically, NMR is applied to investigate the chemical composition of the terpolymer and its modification. X-ray photoelectron spectroscopy (XPS) on the other hand allows for probing the elemental composition of grafted and crosslinked hydrogels and can be used complementary to the optical methods SPR and OWS described before.^[79] XPS analyzes surfaces based on the interaction between the x-ray photons and the inner electrons of the atoms on the substrate of interest. If enough energy is transferred to the electron it is ejected from its orbital and called photoelectron as depicted in figure 2.14. Its kinetic energy E_k measured by the spectrometer is given by:

$$E_k = h\nu - E_b - E_w \quad (2.31)$$

Equation 2.31:

E_w - the work function of the spectrometer; E_b - the binding energy of the former electron.

E_b is characteristic for a particular element and furthermore depends on the chemical environment. The binding energy of the 1s electron of a carbon atom, for example, is rising with the electronegativity of the binding partner, therefore XPS allows for quantitative element analysis and the determination of the elements binding partners as well. A typical XPS spectra is shown in figure 2.14.

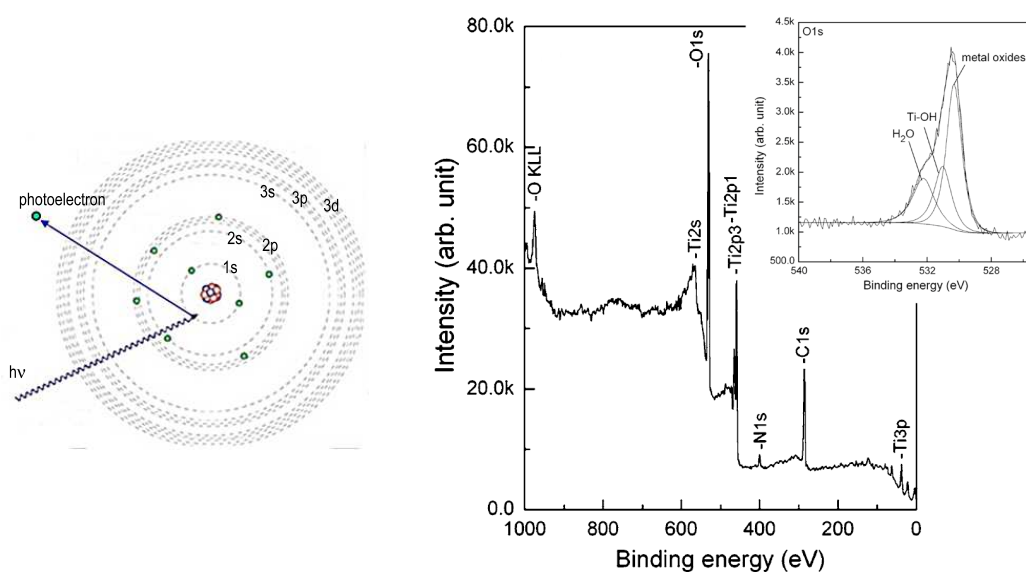


Fig. 2.14: Left: schematic interaction between x-ray photon and electron resulting in a photoelectron. Right: typical XPS spectra showing the elements and a high resolution enlargement allowing for the determination of the binding partner.^[80]

2.6 Time of Flight Secondary Ion Mass Spectrometry (ToF-SIMS)

Complementary to XPS, which allows for the determination of the electronic state of the atoms at the surface and hence the binding partner, time of flight secondary ion mass spectrometry (ToF-SIMS) detects the mass of fragments of molecules on a substrate.^[81] To create and release these fragments from the surface, it is sputtered with a focused primary ion beam. This bombardment initiates a collision cascade inside the first 10 nm of the sample leading to the desorption of molecule fragments from the first 1 - 2 nm (see fig. 2.15). The size of the fragments can be in the range of clusters or down to single atoms, they can be charged or non-charged. The emitted charged fragments, so called secondary ions are extracted and accelerated by an applied high voltage and measured by ToF mass spectrometry to determine their mass to charge ratio (m/z).

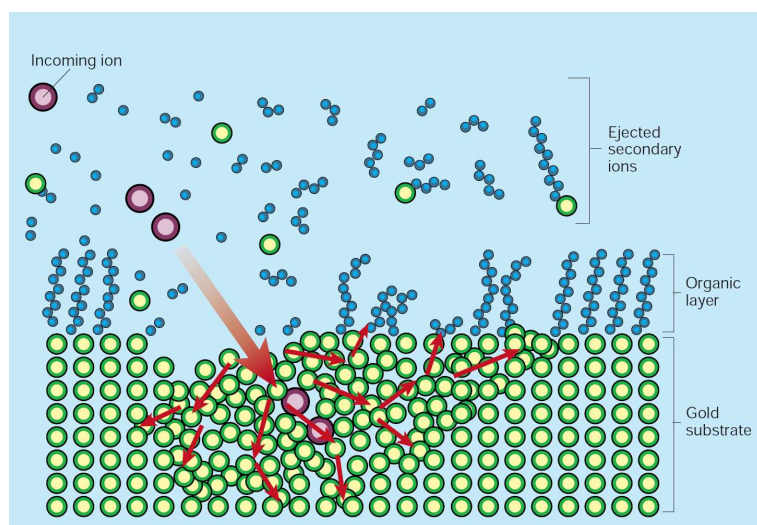


Fig. 2.15: Secondary ions created by collision cascade upon sputtering with primary ions.^[82]

This technique is of 'destructive' nature, however, measuring in static mode, the primary ion fluxes are between 3×10^{11} and 6×10^{11} ions per cm^2 . This means that in the static conditions regime,^[79] less than 0.1% of the surface atomic sites are hit and destroyed by the primary ion beam during a measurement. Therefore, spectra recorded under the 'static SIMS' conditions reveal detailed information about the surface composition without significantly affecting their chemical integrity in larger areas.

2.7 Electrochemical Impedance Spectroscopy (EIS)

In the field of material science, impedance spectroscopy is well established to investigate the electronic properties of various materials and their interfaces to electrodes. Besides studying electrochemical processes like corrosion, few years ago electrochemical impedance spectroscopy (EIS) entered the field of biophysics and is still employed to characterize model membranes and incorporated proteins.^[83–85]

Impedance is the complex resistance of a circuit made from resistors, capacitors and inductors. The impedance is measured by applying an ac voltage of low amplitude and detecting the responding current of the system. For a small ac amplitude [86], the impedance $Z(\omega)$ is given by:

$$Z(\omega) = \frac{U(\omega)}{I(\omega)} = \frac{U_0 e^{i\omega t}}{I_0 e^{i(\omega t - \varphi(\omega))}} = \frac{U_0}{I_0} e^{i\varphi(\omega)} = |Z(\omega)| e^{i\varphi(\omega)} \quad (2.32)$$

Equation 2.32:

$Z(\omega)$ - complex electric impedance as a function of the frequency; $U(\omega)$ - applied voltage as a function of the frequency; $I(\omega)$ - measured frequency dependent current; $\omega = 2\pi f$ - radial frequency; U_0 - amplitude of the voltage; I_0 - amplitude of the current; $\varphi(\omega)$ - frequency dependent phase shift; $|Z(\omega)|$ - absolute value of the impedance.

The impedance can be expressed in cartesian as well:

$$Z(\omega) = Z' + iZ'' \quad (2.33)$$

with

$$\begin{aligned} Z' &= |Z(\omega)| \cos \varphi(\omega) & Z'' &= |Z(\omega)| \sin \varphi(\omega) \\ |Z(\omega)| &= \sqrt{(Z')^2 + (Z'')^2} & \varphi(\omega) &= \arctan\left(\frac{Z''}{Z'}\right) \end{aligned}$$

Equation 2.33:

Z' - real part of the impedance; Z'' - imaginary part of the impedance.

For a circuit consisting of a single resistor, the current is in phase with the voltage. An ideal capacitor, on the contrary, causes a phase shift of 90° or $\pi/2$. Figure 2.16 shows the effect of these two principle building blocks on an applied ac voltage.

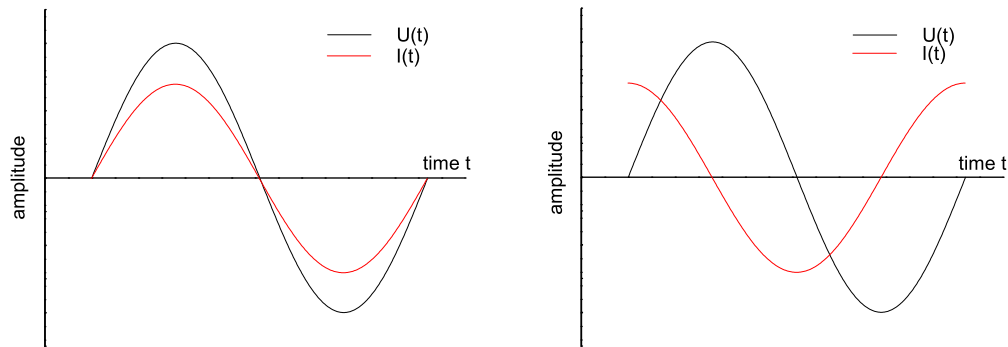


Fig. 2.16: Ideal resistor (left) and an ideal capacitor (right).

Impedance measurements allow for the characterization of complex systems made from combinations of resistors (R) and capacitors (C) parallel and in series. The measured values can be displayed in various plots, according to eq. 2.33. Here, only the Bode-plot and the admittance-plot are employed.

To analyze the plots, a circuit equivalent to the measured system has to be designed, representing the system in the easiest possible way. The easiest equivalent circuit for a model membrane consists of a resistor (R_{feed}) corresponding to the buffer, a RC-element (R and C parallel) in series describing the building stages of the membrane, and a capacitor (C_{SC}) in series representing the space charge effects close to the substrate surface.

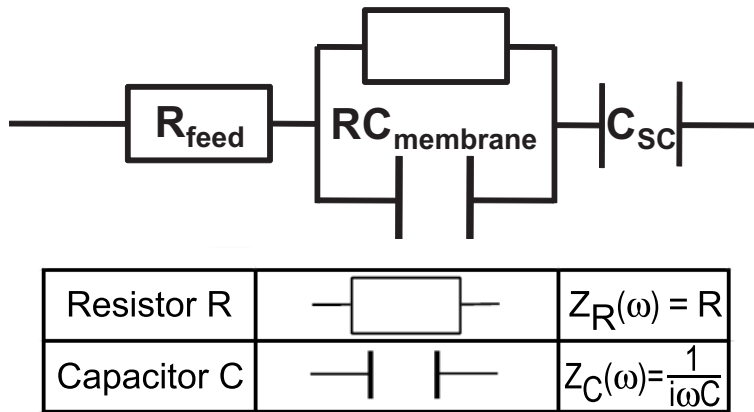


Fig. 2.17: Equivalent circuit and building blocks employed to fit the system.

With this model, an impedance measurement is simulated and matched to the real data by adjusting the building blocks values.

Figure 2.18 shows a typical Bode- and frequency reduced admittance-plot, simulated for a model membrane. The Bode-plot depicts the absolute value of the impedance and the phase shift as a function of the frequency. The admittance-plot displays the imaginary part of the admittance as a function of the real part, with the admittance being the inverse impedance.

$$Y(\omega) = \frac{1}{Z(\omega)} \tag{2.34}$$

The dashed and dotted lines show how to estimate the fit parameter from a real measurement. As a resistor is frequency independent and does not cause a phase shift, the resistances of the system can be obtained from the frequency range of the impedance spectrum with a low slope and a low phase shift, indicated by the horizontal lines. The values used to simulate the spectrum are shown next to the

corresponding guiding lines. These lines demonstrate how to obtain the values from a real measurement.

A slope of -1 in the impedance and a phase shift of 90° corresponds to a frequency range, where the system behaves like a perfect capacitor. The value of the capacity can be taken from the admittance-plot, given by the imaginary part of the admittance at the ends of the semicircles.

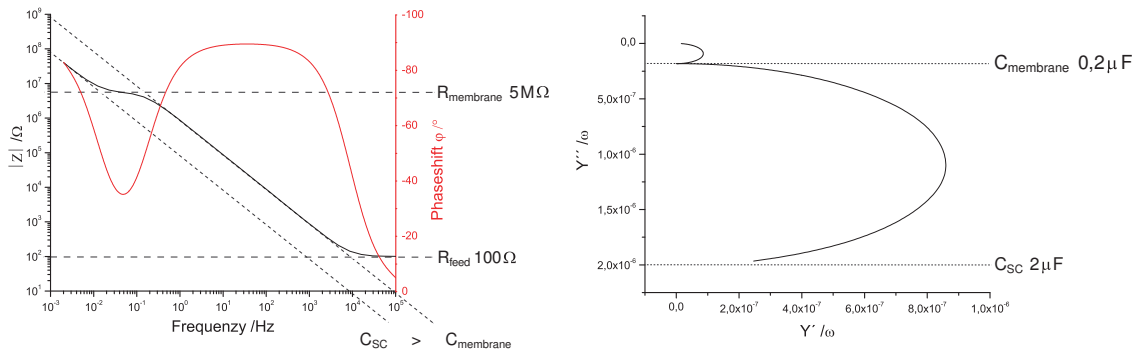


Fig. 2.18: Simulated impedance spectrum presented in Bode- (left) and admittance-plot (right).

When establishing an artificial biomembrane, the resistance rises, as the membrane seals the surface (acting as electrode) from the ions in the buffer. At the same time, the capacity decreases due to being – in a first approximation – inverse related with the distance of the electrolytes from the electrode. These changes are revealed in the Bode- and admittance-plot, shown in figure 2.19.

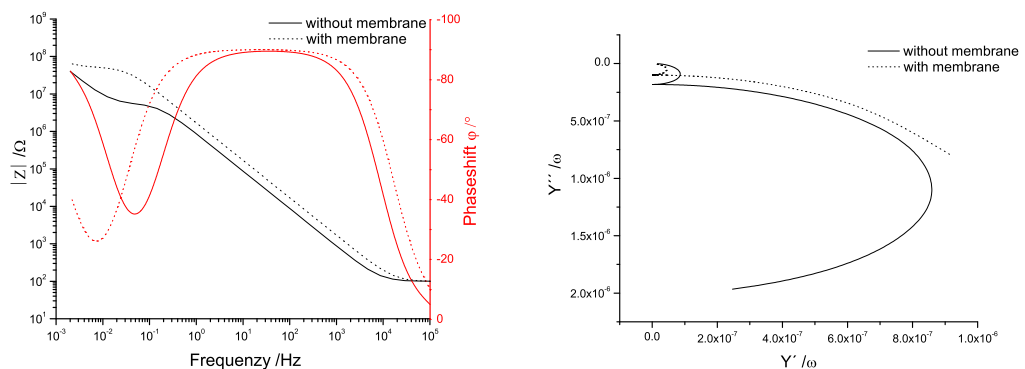


Fig. 2.19: Simulated impedance spectra for the establishment of an artificial biomembrane. Left: Bode-plot, right: admittance-plot.

The setup employed to record impedance spectra generally consists of a potentiostat recording voltage and current as a function of the frequency and a frequency generator, applying a 10 mV ac voltage in a frequency range from 100 kHz to

2 Methods

2 mHz. The measuring cell unites the working electrode – usually the substrate – the platinum counter electrode and the silver/silver chloride reference electrode in a chamber floated with buffer. The measuring cell is kept in a Faraday cage to minimize the electrostatic noise and equipped with in- and outlet tubes to replace the buffer.

3 Preparation of the Hydrogel

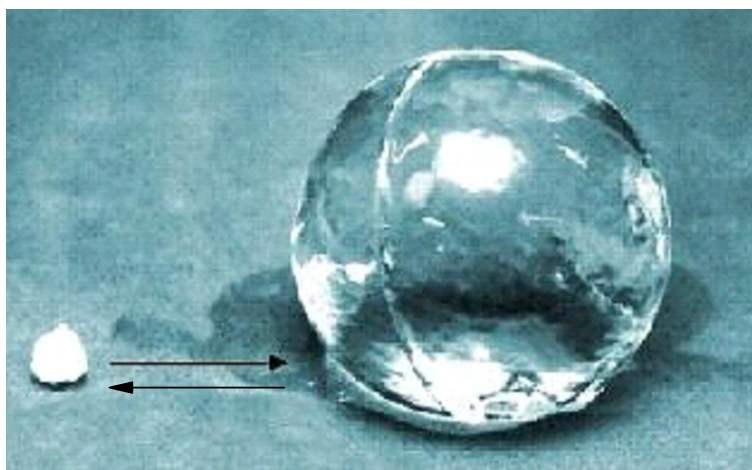


Fig. 3.1: Reversible swelling of a hydrogel ball.(patrick-beines.de)

This chapter introduces the polymer which is studied and applied in this thesis. The general preparation methods are described to obtain the PNIPAAm-based polymer (section 3.1), the hydrogel by subsequent coating and crosslinking on various substrates (section 3.2 and 3.3) and to perform further modifications (section 3.4).

3.1 Polymerization

Multiple methods are known to coat hydrogels on surfaces including brushes grafted from the surface by *in situ* free radical polymerization^[87,88] or by controlled radical polymerization techniques^[89–92] and grafting of functionalized PNIPAAm to a modified substrate.^[91,93,94] E-beam^[95] and plasma polymerization^[96–98] had been employed as well.

In this thesis coating is achieved by spincoating of an uncrosslinked polymer followed by crosslinking and surface attachment by UV-light.^[46,99,100] In a first step, a terpolymer from *N*-isopropylacrylamide (NIPAAm), methacrylic acid (MAA),

3 Preparation of the Hydrogel

and 4-benzoylphenyl methacrylate (MABP)^[101] was prepared by free radical polymerization in solution, as depicted in Figure 3.2.

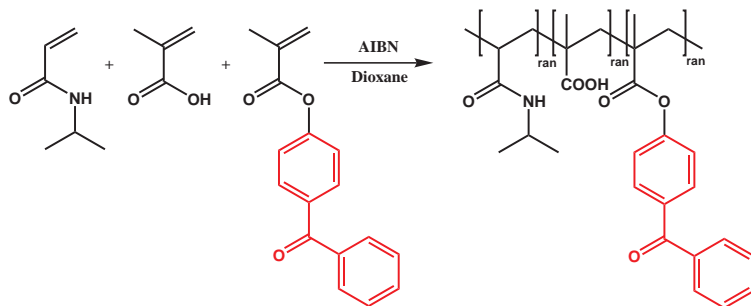


Fig. 3.2: Free radical terpolymerization of NIPAAm, MAA and MABP.

The terpolymer was obtained with an average yield of $\sim 80\%$. For purification it was either precipitated from methanol to ice cold diethyl ether, ultrafiltered (MWCO: 20.000 g/mol) with THF, or dialyzed (MWCO: 14.000 g/mol) with DMF. GPC gave a molecular mass of $M_n = (115.000 \pm 5.000)$ g/mol and $M_w = (250.000 \pm 15.000)$ g/mol and a polydispersity of $PDI = 2.2 \pm 0.1$ for all purification methods. The determination of the chemical composition is described in chapter 4.

The copolymerization with MABP allows for the subsequent crosslinking of the polymer by UV-irradiation. The crosslinking density can be conveniently tuned and its influence on the hydrogels properties is subject of the research in this thesis. Furthermore, MABP can covalently attach to alkyl alike substrates like polyethylene (see section 7.2) and enables structuring of the hydrogel by UV-lithography.

MAA as comonomer provides the possibility of further functionalization even subsequent to gel formation. This can be achieved via the introduction of active ester groups (see section 3.4). Such a chemical modification provides access to the insertion of more benzophenone crosslinking units (see section 3.6.4) and to an even larger range of applications such as response to an additional stimulus or as biosensor.

Additionally, MAA reduces the 'skin-effect' by supporting the formation of channels and contributes to a higher degree of swelling.^[43,45,102]

Generally, the benefit of grafting polymers to a surface and subsequent crosslinking is the possibility of preliminary investigations on the polymer, for example with NMR, GPC or light scattering techniques, as performed in the following chapters.

3.2 Grafting

Surfaces inert to the attack of the benzophenone, eg. noble metals, metal oxides and metal oxide alikes, require treatment prior to coating to enable the attachment of the hydrogel. For noble metals, such as gold and silver, which is commonly used in SPR-techniques, a benzophenone-derivative with a thiol anchor (4-(3-mercaptopropoxy)benzophenone, BP-thiol)^[103] (fig. 3.3 right) was synthesized and employed. In the case of metal oxides, ITO, silicon, and silicon oxide (glass) for instance or metal oxide alikes, for example plasma oxidized silicone and polystyrene, benzophenone with a triethoxysilane anchor (4-(3-triethoxysilyl)propoxybenzophenone, BP-silane) was used (fig. 3.3 left).

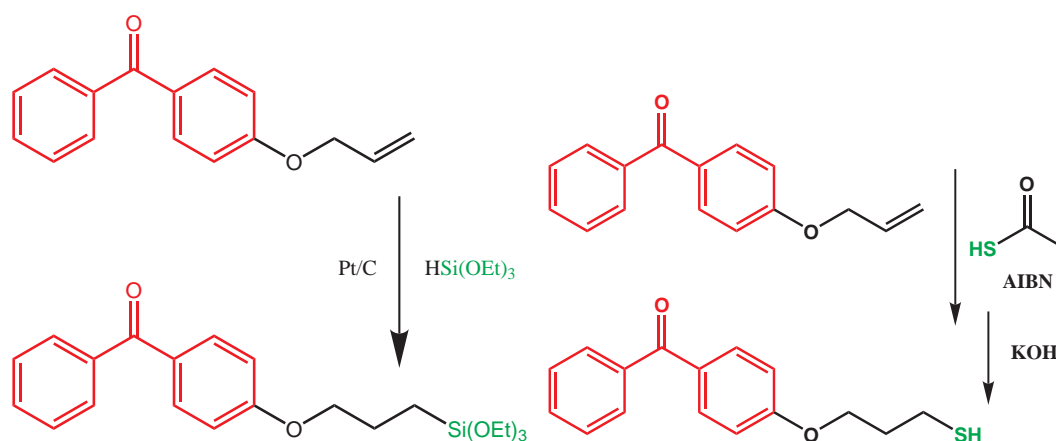


Fig. 3.3: Benzophenone-derivatives used for the self-assembly of benzophenone on the desired surface as adhesion promoter. BP-silane is shown on the left and BP-thiol on the right.

The BP-thiol was further developed from the known *S*-3-(4-benzylphenoxy)-propyl ethanethioate^[99] as it eases the self-assembly process. The ethanethioate was cleaved in a methanolic potassium hydroxide solution as depicted in figure 3.3 (right). The benzophenone SAM was obtained by simply immersing a respective substrate in an 1 mmol ethanolic solution for 24 hours. After thoroughly rinsing with ethanol and drying a measured contact angle of 80° with water proves a dense monolayer.

The triethoxysilane anchor was attached to the 4-allyloxy-benzophenone via hydrosilylation with platinum on activated charcoal. Compared to the patented procedure^[104] of using hexachloroplatinic acid where the catalyst is hazardous to the product, this method provides the product without any further purification besides the filtering from the solid catalyst. Due to its lower reactivity, the triethoxysilane can conveniently be handled under standard laboratory conditions and is therefore advantageous compared to the chlorosilanes. Furthermore,

3 Preparation of the Hydrogel

stored as ethanolic solution self-condensation is avoided and hence the durability is enhanced. Self-assembly was performed in an 1 mmol ethanolic solution within three days followed by extensive rinsing with ethanol. This procedure resulted in a less dense monolayer compared to the BP-thiol, as the contact angle is only $\sim 40^\circ$. A denser functionalization (ca $\sim 70^\circ$) can be achieved by curing the respective substrate in toluene and 1 % of a 50 mmol ethanolic BP-silane solution at 80°C over night. Afterwards the substrates were rinsed with toluene and subsequently with ethanol.

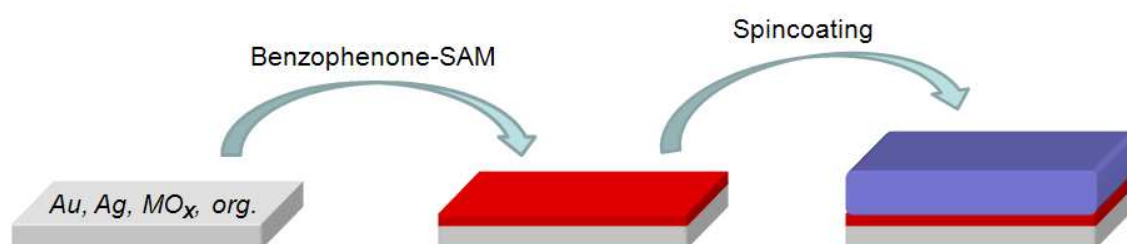


Fig. 3.4: Preparation of the hydrogel film by spincoating on the benzophenone modified surface.

On these functionalized substrates an ethanolic solution of the PNIPAAm-based terpolymer was spincoated (fig. 3.4). The concentration of the polymer varied corresponding to the desired thickness (see respective experimental parts) but the rotation speed was kept constant at 4000 rpm as this speed provided smooth surfaces. The coated substrates were dried under vacuum at 50°C over night.

An additional benefit of using an uncrosslinked hydrogel precursor is the possibility of structured coating. The easiest case is a 2D structure obtained by printing the polymer solution,^[105] which can be achieved with commercial available inkjet printer as well, as shown in figure 3.5.



Fig. 3.5: Hydrogel from an 1% aqueous polymer solution deposited by an inkjet printer. With Dave Tune, 9D Tech.

To take the pictures, the printed slides were cooled down to condense water. Upon condensation, the hydrogel swells whereas water particles form on the uncoated glass and scatter the light.

3.3 Crosslinking

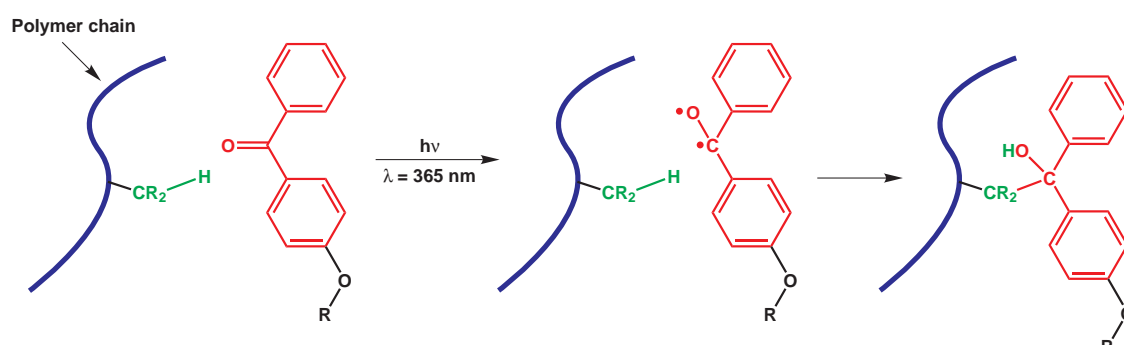


Fig. 3.6: Crosslinking and covalent surface attachment are achieved by irradiation with UV-light upon which the benzophenone forms the diradical responsible for the crosslinking and surface attachment as well.

Finally, the coatings were crosslinked and attached to the substrate via the benzophenone units. Upon irradiation with a wavelength of $\lambda = 365 \text{ nm}$ (Stratalinker 2400, Agilent, Germany) benzophenone forms a diradical, inserting into any available non-aromatic C-H bond as depicted in figure 3.6.

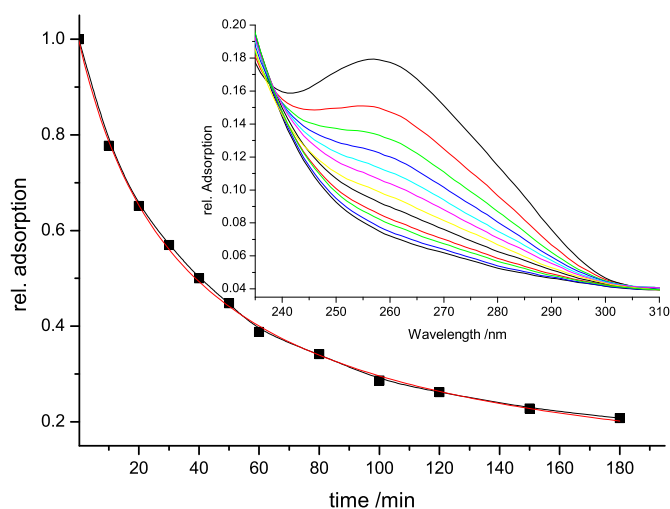


Fig. 3.7: Evolution of the intensity of the absorption maxima (261 nm) of the benzophenone (inset) with irradiation time. The decay was fitted with $I \sim T_{UV}^{-0.9}$ (red line).

Thereby, the copolymerized benzophenone units cause the crosslinking whereas the surface attached benzophenone enables the immobilization on the substrate. By varying the irradiation dose ($\sim 0.105 \text{ J cm}^{-2}$ per minute) corresponding to an irradiation time, properties like swelling ratio, mesh size (see chapter 6) and

refractive index (see chapter 5) can be customized for the aspired application (see chapter 7). Furthermore, it allows for a 3D structuring of the hydrogel by UV-interference-lithography.^[106]

The chosen wavelength for crosslinking does not match the absorption maxima of the benzophenone as the inset in figure 3.7 reveals. However, irradiating in the tail of the adsorption band allows for the fine tuning of the crosslinking density. The decay of the adsorption intensity I with irradiation time in figure 3.7 was fitted with $I \sim T_{UV}^{-0.9}$ (red line). In section 6.1.2.2 it was found that the swelling ratio $\kappa \sim T_{UV}^{-0.3}$. We assume that the hydrogel swells only perpendicular to the surface (1D) as the parallel swelling is hindered by the grafting. The ratio of three in the exponent of the two irradiation time dependencies – light adsorption is a 3D phenomena – supports this concept.

3.4 Chemical Modification

Active ester chemistry, though known for many years and well established in peptide synthesis, gained a lot of interest in polymer analogous reactions together with so called click chemistry. It allows modification of the terpolymer and furthermore the grafted gel as well.

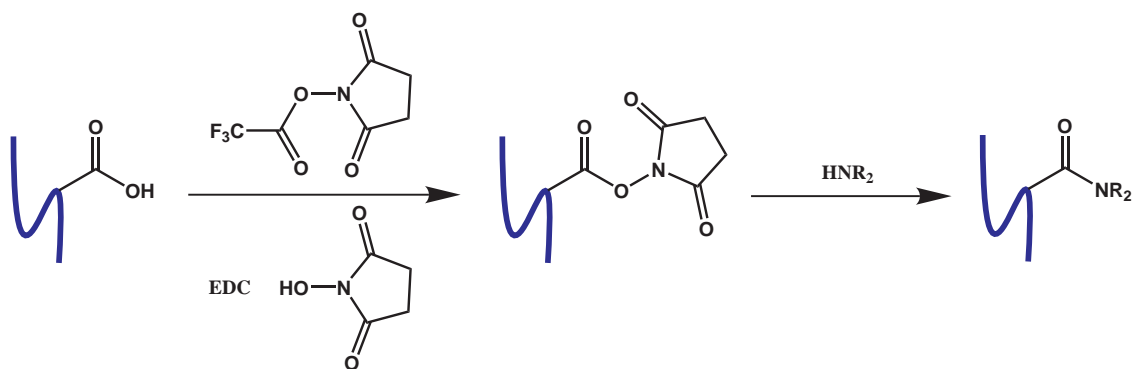


Fig. 3.8: Activation of the methacrylic acid via EDC route or exchange from the respective trifluoroacetate.

Beside forming the ester from the acid chloride, figure 3.8 describes the other two methods to obtain active esters. On the one hand, the trifluoroacetate (TFA) of the desired 'active' alcohol can be employed. Via transesterification the alcohol is transferred to the polymeric acid, releasing the free TFA. On the other hand, 1-ethyl-3-(3-dimethylaminopropyl)carbodiimide (EDC) can be used to form the ester with the 'active' alcohol. Both routes have their advantages and drawbacks,

the TFA-route, also referred to as *ex situ*-method, is not applicable in water and requires an additional purification step to avoid the reaction of the TFA-ester with the amine, one wants to attach. The EDC-route in turn bears the side reaction to the 'dead' amide via translocation and, though predestinated for *in situ* use in aqueous media, it failed preparing the acetonoxime ester (see overview in table 7.1 in section 7.1).

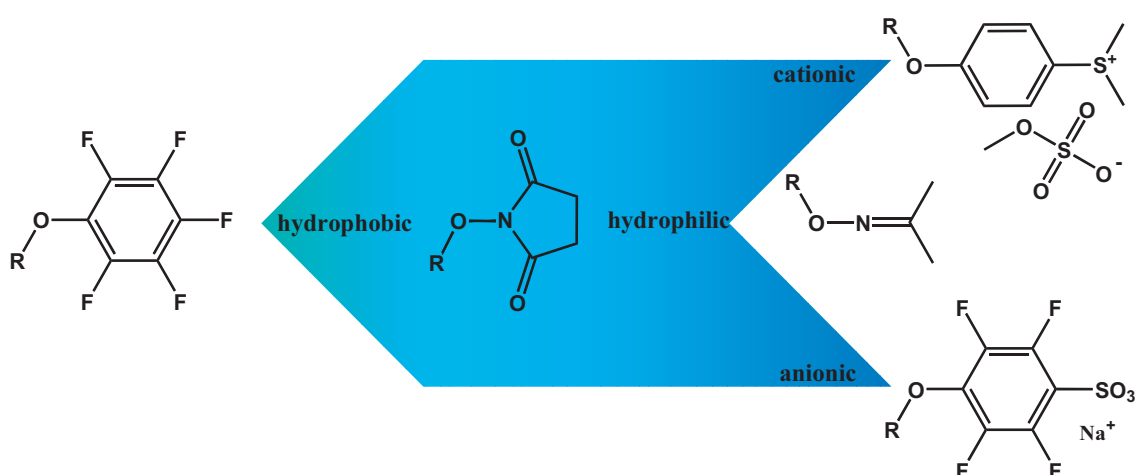


Fig. 3.9: Applied active esters classified according to their character.

Depending on the reaction media for the coupling of the amine and its character, several 'active' alcohols and corresponding TFA-esters were synthesized. Figure 3.9 shows and classifies them according to their hydrophobicity and charge. Initially, *N*-hydroxysuccinimide (NHS) was used, though known for its low stability in water. Pentafluorophenol (PFP) was employed due to its higher stability in water and nevertheless higher reactivity to amines. Since PFP is very hydrophobic, another uncharged species – acetonoxime (AO)^[107] – was added to the assortment to provide a more hydrophilic active ester. For the implementation of the hydrogel as (bio)sensor matrix, it is necessary to bind biomolecules like proteins (see section 7.1) and DNA single strands to the polymer. As these are charged and often limited to usage in aqueous media, active esters with a charge attraction scheme are desirable for the covalent immobilization. For proteins, sodium tetrafluorophenol sulfonate (TFPS) ester^[108] was synthesized to attract their positive charge. To couple negatively charged DNA single strands, the TFA-*p*-hydroxyphenyldimethylsulfonium methylsulfate (TFA-DMPS)^[109] is provided.

3.5 Outlook

If one takes a look on the copolymerization parameters, as already discussed in an earlier thesis of Patrick Beines,^[110] it is very likely, that the distribution of the monomers in the polymer is highly inhomogeneous. NIPAAm prefers the insertion of the other monomers ($r < 0.4$) whereas these prefer themselves ($r > 2$). Given the higher concentration of NIPAAm compared to MAA and MABP, the composition will even change with conversion.

One possibility to avoid heterogeneity is to synthesize monomers which are more similar. In order to have an all acrylamide backbone in the polymer, benzophenylacrylamide (inset of fig. 3.15) was prepared according to literature^[111] as a substitute to MABP. The next step would be the synthesis of acrylamidoacetate to replace MAA. However, this work was only launched during this thesis.

3.6 Experimental Part

3.6.1 P(NIPAAm-stat-MAA-stat-MABP)

The monomers were prepared according to literature,^[99] NIPAAm was recrystallized from toluene/hexane (1/4), AIBN from methanol, MAA was distilled from the stabilizer, MABP was prepared following Toomey *et al.*^[101] and dioxane was distilled over calcium hydride. Typically 21 g (185.57 mmol, 100 eq.) NIPAAm, 798.7 mg (9.27 mmol, 5 eq.) MAA and 494.2 mg (1.86 mmol, 1 eq.) MABP were dissolved in 140 ml dry dioxane. After argon was bubbled through the solution for at least one hour, 140 mg (0.85 mmol, 0.0046 eq.) AIBN were added. The free radical polymerization was carried out at 60°C under argon and quenched after 24 hours. This was achieved either by precipitating in ice cold diethyl ether when purified by precipitation or by adding untreated dioxane in the case of purification by dialysis techniques as described above. The obtained polymer was freeze-dried from *tert.* butanol in vacuum and characterized as discussed in chapter 4.

3.6.2 BP-silane

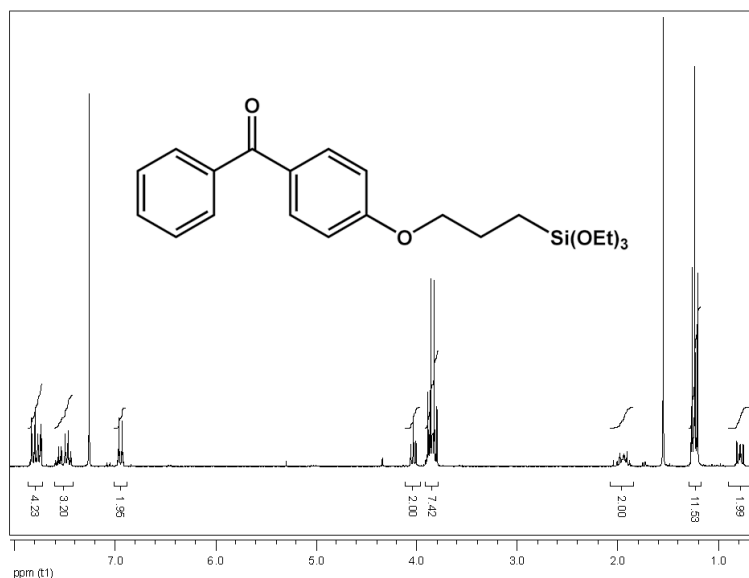


Fig. 3.10: ¹H-NMR of 4-(3-triethoxysilyl)propoxybenzophenone (BP-silane).

4-Allyloxybenzophenone (1 g, 4.2 mmol) (prepared according to literature^[101]) was dissolved in triethoxysilane (10 mL, 44.4 mmol) at room temperature under argon. After addition of platinum on activated charcoal (10 mg, 10%) the solution was stirred at room temperature until TLC (heptane : acetone = 5 : 1; 4-allyloxybenzophenone: R_f : 0.33; product: R_f : 0.22, further decomposition products due to the reaction with the silica gel have lower R_f values) shows complete conversion of the 4-allyloxybenzophenone, which was achieved after 2 d. The catalyst was filtered off and the excess of triethoxysilane was removed in high vacuum. The product was yielded quantitatively as brownish white solid and used without further purification.

FD-MS (Field Desorption Mass Spectrometry): m/z = 402.3 [M]⁺, 804.7 [$2M$]⁺.

¹H-NMR (250 MHz, CDCl₃): δ (ppm) = 7.81 (d, 2H, 2,6-phenone, ³J_{2,6;3,5} = 8.7 Hz), 7.75 (d, 2H, 2,6-benzyl, ³J_{2,6;3,5} = 7.1 Hz), 7.57 (t, 1H, 4-benzyl, ³J_{4;3,5} = 7.2 Hz), 7.47 (t, 2H, 3,5-benzyl, ³J_{3,5;2,4,6} = 7.2 Hz), 6.95 (d, 2H, 3,5-phenone, ³J_{3,5;2,6} = 8.7 Hz), 4.03 (t, 2H, 1-propoxy, ³J_{1,2} = 6.6 Hz), 3.84 (q, 6H, CH₂ ethoxy, ³J_{CH₂;CH₃} = 7.0 Hz), 1.94 (td, 2H, 2-propoxy, ³J_{2,1,3} = 6.6, 8.1 Hz), 1.24 (t, 9H, CH₃ ethoxy, ³J_{CH₃;CH₂} = 7.0 Hz), 0.78 (t, 2H, 3-propoxy, ³J_{3,2} = 8.1 Hz).

3.6.3 Active Esters

3.6.3.1 TFA-NHS

After adding *N*-hydroxysuccinimide (2.6 g, 23 mmol) to trifluoroacetyl anhydride (4.7 ml, 34 mmol) at 0°C the solution was stirred for 20 h at room temperature. The volatiles were evaporated leaving the product (colorless powder, 4.5 g, 21 mmol) behind.

3.6.3.2 TFA-AO

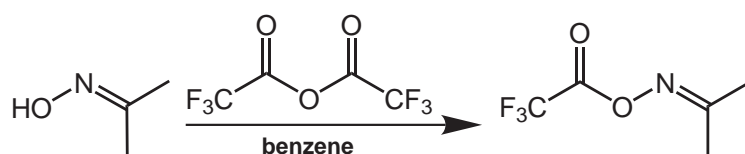


Fig. 3.11: Synthesis of TFA-acetonoxime.

Trifluoroacetyl anhydride was added to acetonoxime dissolved in dry benzene at 0°C under argon atmosphere. The solution was allowed to warm up to room temperature and was stirred for another 12 hours. The solvent was evaporated and trifluoroacetyl-acetonoxime (TFA-AO) was obtained by fractionated distillation at 30°C and a pressure of 5 mbar.

¹H-NMR (250 MHz, CDCl₃): δ (ppm) = 2.09 (s, 3H, CH₃), 2.08 (s, 3H, CH₃).

3.6.3.3 TFA-TFPS

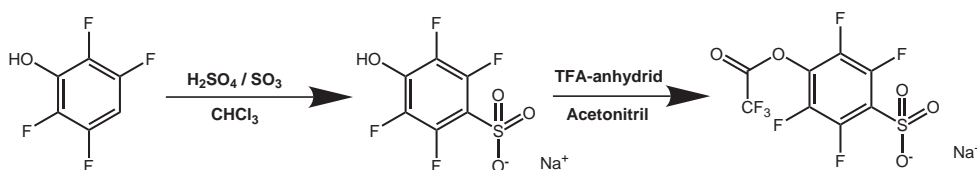


Fig. 3.12: Synthesis of TFA-TFPS.

TFPS:^[108] 2,3,5,6-Tetrafluorophenol (13.8 g, 84 mmol) dissolved in 50 mL chloroform where sulfonated by adding 40 mL fuming sulfuric acid (26 % SO₃) at 25°C. When the TLC showed complete conversion (typically after 20 h) the solution was poured into iced brine. TFPS was precipitated by adding sodium chloride, followed by repeated extraction of the precipitate with acetonitrile. The product was obtained as colorless crystals (4.3 g, yield 51 %).

^{19}F -NMR (470 MHz, CD_3CN) ϕ ($\text{C}_6\text{H}_5\text{F}$): δ (ppm) = -147.04 (d, 2F, $^3J = 17.5$ Hz), -168.18 (d, 2F, $^3J = 17.5$ Hz).

TFA-TFPS:^[108] TFPS (500 mg, 1.9 mmol) was refluxed with 30 mL dry acetonitrile and 5 mL trifluoroacetyl anhydride for 3 h under argon atmosphere. After the volatiles were distilled off TFA-TFPS was obtained as colorless powder (320 mg, 0.88 mmol, yield 46%).

^{19}F -NMR (470 MHz, CD_3CN) ϕ ($\text{C}_6\text{H}_5\text{F}$): δ (ppm) = -73.34 (s, 3F, CF_3), -136.68 (d, 2F, aromatic C-F, $^3J = 13.6$ Hz), -150.27 (d, 2F, aromatic C-F, $^3J = 13.6$ Hz).

3.6.3.4 TFA-DMPS

p-Hydroxyphenyldimethylsulfonium methylsulfate (1 g, 3.75 mmol) in 20 mL dry acetonitrile was added to 20 ml trifluoroacetyl anhydride at room temperature under argon atmosphere. After 18 h stirring at 50°C the volatiles were distilled off and TFA-DMPS was obtained as colorless powder. ^1H -NMR reveals that the counter ions were $\sim 33\%$ methylsulfate and $\sim 66\%$ trifluoroacetate.

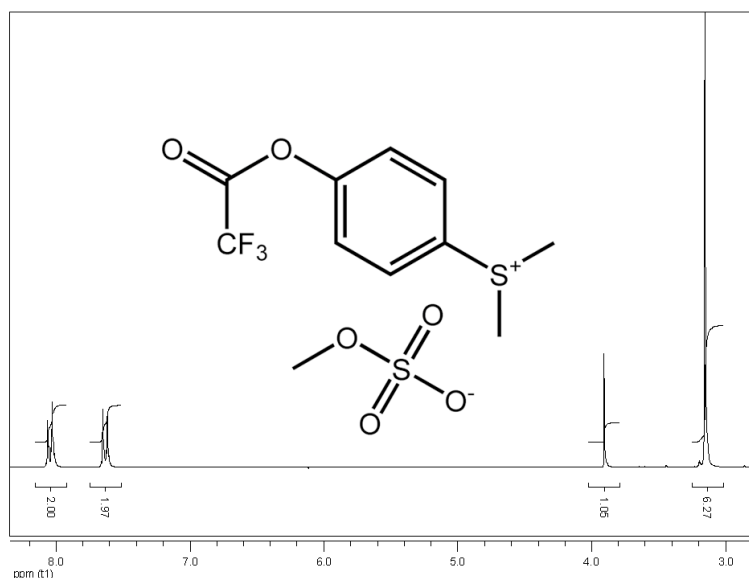


Fig. 3.13: ^1H – NMR of TFA-DMPS.

^1H -NMR (250 MHz, CD_3CN): δ (ppm) = 8.05 (d, 2H, ortho, $^3J_{\text{ortho;meta}} = 9.0$ Hz), 7.63 (d, 2H, meta, $^3J_{\text{meta;ortho}} = 9.0$ Hz), 3.91 (s, 3H methylsulfate), 3.15 (s, 6H, dimethylsulfonium).

3.6.4 Aminomethylbenzophenone

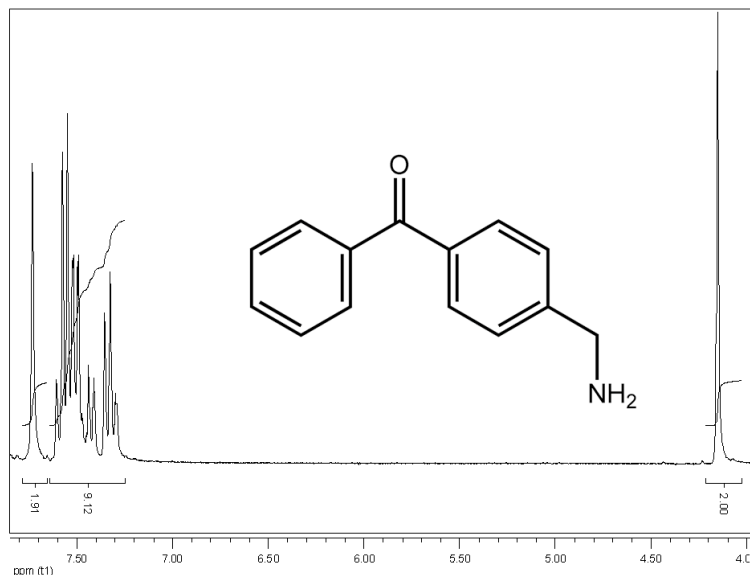


Fig. 3.14: ¹H-NMR of 4-(aminomethyl)-benzophenone.

4-(Bromomethyl)-benzophenone: To 4-methylbenzophenone (120 g, 612 mmol, 1.00 eq) in 600 ml carbontetrachloride *N*-bromosuccinimide (NBS, 120 g, 674 mmol, 1.10 eq) and AIBN (0.6 g, 3.66 mmol) were added and refluxed under argon atmosphere for 4 h. After cooling to room temperature the precipitated succinimide was filtered off, the volatiles were distilled off. The colorless powder was recrystallized from carbontetrachloride yielding 4-(bromomethyl)-benzophenone (101 g, 60%).

¹H-NMR (250 MHz, CDCl₃): δ (ppm) = 7.79 (m, 4H, 2,6-phenone, 2,6-benzyl), 7.60 (t, 1H, 4-benzyl, ³J_{4,3,5} = 7.4 Hz), 7.49 (m, 4H, 3,5-benzyl, 3,5-phenone), 4.54 (s, 2H, methyl).

4-(Aminomethyl)-benzophenone: To liquid ammoniac (3 L) 4-(bromomethyl)-benzophenone (70 g, 250 mmol) dissolved in dry THF (160 mL), dry MeOH (100 mL) and dry chloroform (260 mL) was added at -45°C. After the ammoniac was allowed to evaporate over night and the volatiles were distilled off, the residue was suspended in chloroform. Colorless crystals of 4-(aminomethyl)-benzophenone were obtained (44.59 g, yield 84%).

¹H-NMR (250 MHz, d-DMF): δ (ppm) = 7.73 (s, 2H, amine), 7.45 (m, 9H, aromatic), 4.15 (s, 2H, methyl).

3.6.5 Benzophenylacrylamide

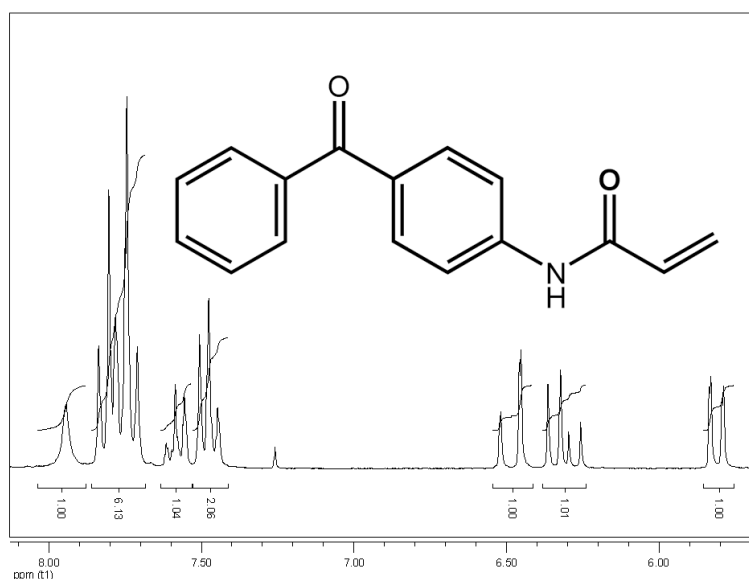


Fig. 3.15: ¹H-NMR of 4-benzophenylacrylamide.

4-Aminobenzophenone (4 g, 20.3 mmol) in 50 mL dry benzene, 2 mL dry DMSO, and 10 mL dry triethylamine was reacted with acryloyl chloride (5 mL, 61.5 mmol) in 40 mL dry benzene with few crumbles inhibitor (2,6-di-*tert*-butyl-4-methylphenol) at 0°C under argon for 30 min. After the addition of 40 mL 1 molar hydrogen chloride solution the solvents were separated from the solid formed and washed with 1 molar hydrogen chloride solution and MilliQ subsequently. Volatiles were distilled off and recrystallization of the solid from ethanol gave the product with a yield of 45%.

¹H-NMR (250 MHz, CDCl₃) δ (ppm) = 7.95 (s, 1H, amide), 7.78 (m, 6H, 2,3,5,6-phenone, 2,6-benzyl), 7.59 (t, 1H, 4-benzyl, ³J_{4;3,5} = 7.3 Hz), 7.48 (t, 2H, 3,5-benzyl, ³J_{3,5;4} = 7.3 Hz), 6.49 (dd, 1H, allyl-cis, ³J_{cis;gem} = 16.8 Hz, ²J_{cis;trans} = 1.3 Hz), 6.31 (dd, 1H, allyl-gem, ³J_{gem;cis} = 16.8 Hz, ³J_{gem;trans} = 10.0 Hz), 5.81 (dd, 1H, allyl-trans, ³J_{trans;gem} = 10.0 Hz, ²J_{trans;cis} = 1.3 Hz).

4 Chemical Characterization

Beside the characterization of the polymer chain length and chain length distribution by GPC reported in section 3.1, the chemical composition of the polymer was determined by $^1\text{H-NMR}$. The surface chemistry of the grafted hydrogel was characterized by XPS. Furthermore, ToF-SIMS was employed in section 7.3.

4.1 Polymer Composition by NMR

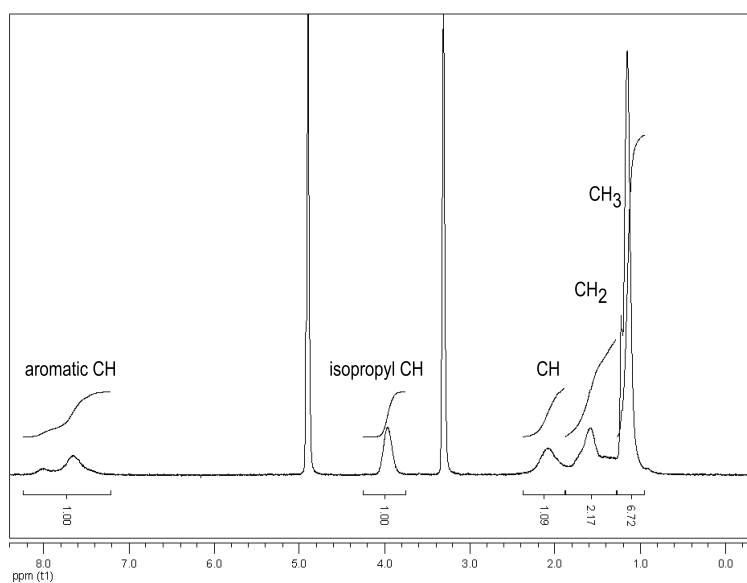


Fig. 4.1: $^1\text{H-NMR}$ in *d*-methanol of the hydrogel-polymer.

Figure 4.1 shows a typical $^1\text{H-NMR}$ of the terpolymer as prepared in section 3.1. The polymer composition was determined by the independent integration of the CH-peak (around 3.9 ppm) of the isopropyl group and the aromatic CH-peaks of the MABP (around 7.8 ppm). The amount of methacrylic acid had to be calculated from the CH_3 -peak (around 1.1 ppm) with a given amount of NIPAAm and MABP. Previously,^[99] this polymer was reported to consist of 86 mol% NIPAAm, 5 mol% methacrylic acid and 9 mol% MABP in good agreement with the integrals in figure 4.1.

4 Chemical Characterization

For a yield of $\sim 80\%$ and a monomer composition of 94% NIPAAm, 5% MAA and 1% MABP, this composition is mathematically impossible. When the copolymerization of NIPAAm and methacrylic acid created a peak at the same shift as the aromatic MABP peak, it was suggested that the polymer composition is closer to the composition of the monomer mixture.^[112] The increase in the intensity of the aromatic peak might be due to an interaction between the amide proton of the NIPAAm and the methacrylic acid.

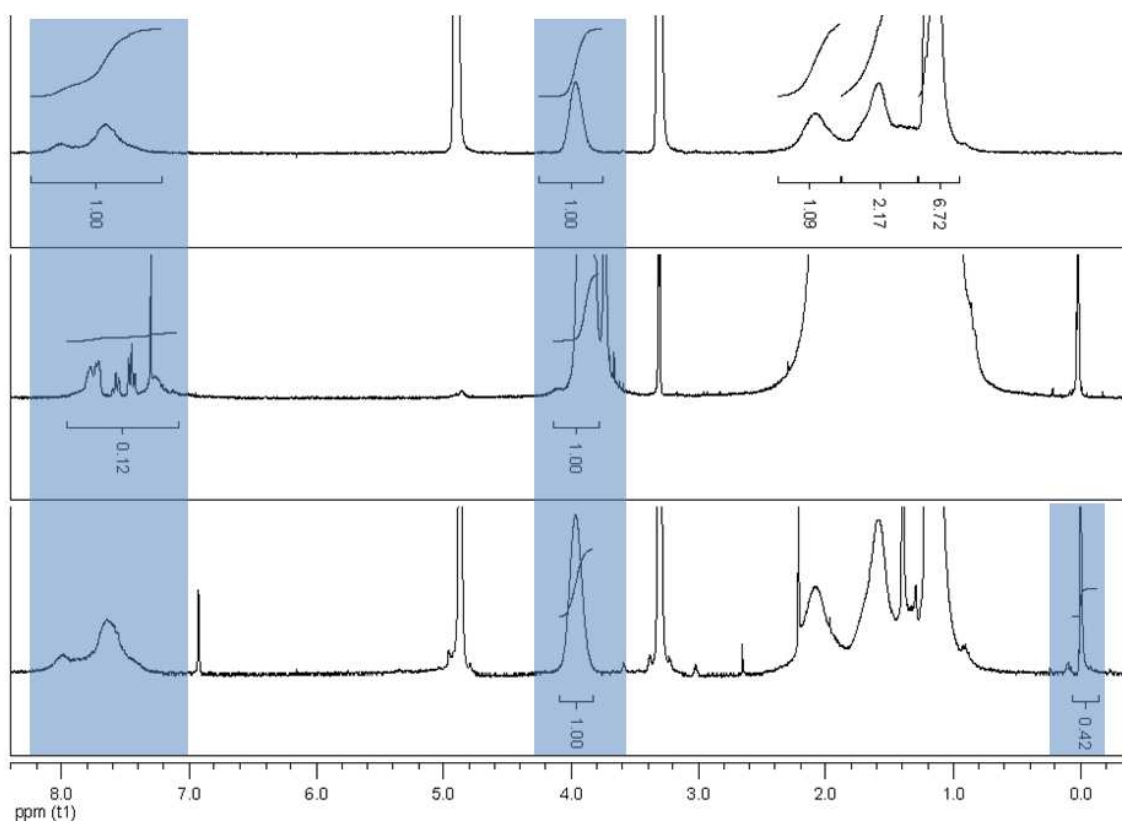


Fig. 4.2: Compared $^1\text{H-NMR}$ spectra of the terpolymer measured in *d*-methanol (top), after addition of D_2O and *d*-chloroform (middle), and after preparation of the TMS-ester (bottom, measured in *d*-methanol).

Such amide peaks can be concealed by the addition of deuterium oxide as these protons can be exchanged by deuterium. Actually, in a $^1\text{H-NMR}$ in a mixture of *d*-methanol, *d*-chloroform and D_2O the intensity of the broad aromatic peak was significantly decreased and a finer structure typical for MABP became visible (fig. 4.2, middle). To verify the assumption that the vanished peak can be assigned to an amide, a high temperature (373 K) $^1\text{H-NMR}$ was measured, as amide and carboxyl peaks are known to shift with temperature (fig. 4.3). Since the result validated the effect of the addition of D_2O , it can be stated, that the calculated amount of MABP in the terpolymer in relation to NIPAAm is $\sim 1 : 100$ contrary

to the ratio of $\sim 1 : 10$ reported earlier.^[99]

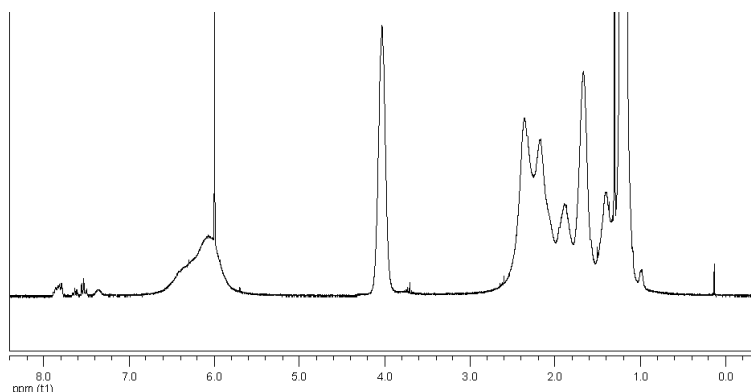


Fig. 4.3: High temperature (373 K) ^1H -NMR in *d*-tetrachloroethane of the terpolymer.

To check, if the calculated amount of methacrylic acid is correct, the carboxyl-group was converted in a polymer analogous reaction to the corresponding trimethylsilyl (TMS) ester. Taking its ^1H -NMR in figure 4.2 (bottom) into account, the fraction of MAA in the terpolymer was committed to 5 mol% and 1 mol% for MABP respectively. A ^1H -NMR of the terpolymer with the TMS ester in deuterium oxide was not recorded as D_2O contains TMS as reference material (see fig. 4.2 middle).

4.2 Hydrogel Surface Chemistry by XPS

Some hydrogel architectures are not accessible by NMR or GPC, like brushes grafted from the surface, gels obtained by *in situ* polymerization from the surface and plasma polymerized films. As for those, XPS is a valuable tool to determine the chemistry on the surface of the hydrogel film and furthermore to observe its modification. The XPS measurements were kindly performed by Marek Jasieniak from the Ian Wark Research Institute in Adelaide, a typical XPS spectra is shown in Figure 4.4.

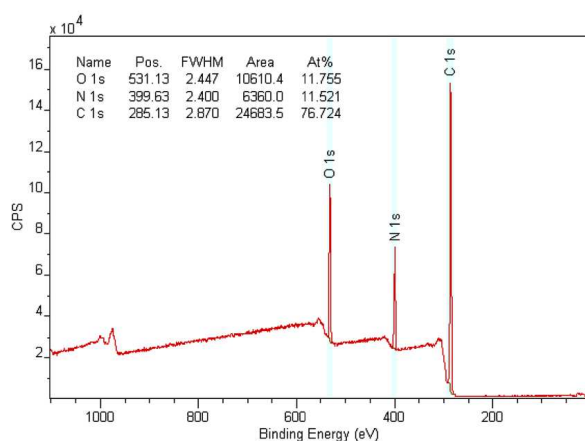


Fig. 4.4: XPS survey spectra of the grafted and crosslinked terpolymer.

It displays the binding energy of the corresponding elements. In high resolution spectra, more detailed information about the binding partner of the respective element can be received. Especially the C1s-spectra (see fig. 4.5, left) contains information about the quantitative composition of the hydrogel surface. The fit of the C1s spectra, and N1s and O1s as well, was performed according to the database of Beamson and Briggs.^[113] It reveals the different carbon containing groups, like carbonates and amides, as well as more general bonds, C-N, C-C-O, C-C and C-H. The O1s spectra was fitted with three groups of species with similar binding energy. Most prominent is the amide-oxygen, but the oxygen atoms of methacrylate and MABP are clearly visible and moreover well above the resolution limit. The measured values of the hydrogels with different crosslinking densities from uncrosslinked (HG-0) to a crosslinking time of 60 min (HG-60) are compared with the theoretical values in table 4.1.

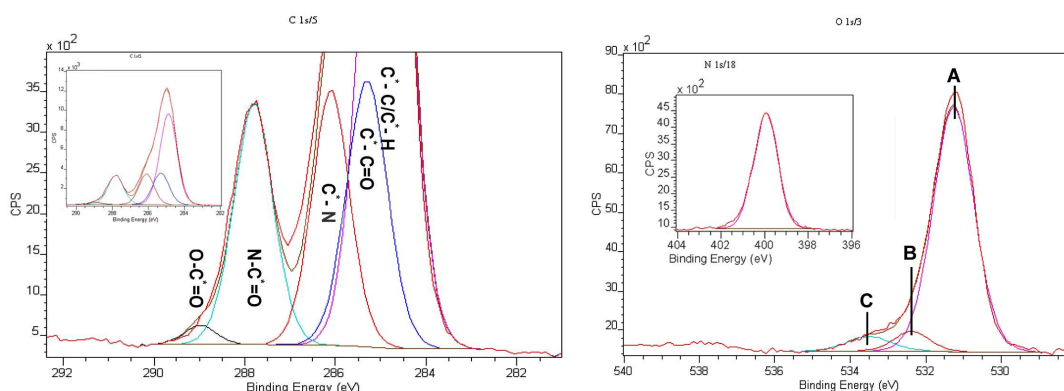


Fig. 4.5: High resolution XPS spectra including the fits of C1s (left, overview in the inset), O1s (right) and N1s (right inset).

The atomic composition of the hydrogel surface exhibits a slightly too high rela-

tive amount of carbon and nitrogen, a common problem in XPS. This results in a too low value for oxygen.

Table 4.1: Comparison of the experimental measured composition of the hydrogel surface by XPS with the theoretical values.

Sample	Composition /atom %			
	O	N	C	
HG-0	11.7	11.6	76.7	measured
HG-30	11.4	11.6	77.1	measured
HG-60	11.6	12.0	76.4	measured
	16.7	12.9	70.4	calculated

Sample	Composition of C 1s region /atom %					
	C-C / C-H	C-C=O	C-N	N-C=O	O-C=O	
HG-0	51.7	17.1	15.3	15.0	1.0	measured
HG-30	48.3	18.6	17.5	15.2	0.8	measured
HG-60	48.2	18.7	15.6	16.6	0.9	measured
	50.4	17.0	15.6	15.6	1.0	calculated

Sample	Composition of O 1s region /atom %			
	A (N-C=O, Ar-C=O)	B (CO*O, C-OH)	C (COO*, COO*R)	
HG-0	88.2	6.1	5.7	measured
	89.6	4.7	5.7	calculated
HG-30	88.0	6.4	5.6	measured
	89.2	5.2	5.7	calculated
HG-60	88.8	5.6	5.7	measured
	88.9	5.4	5.7	calculated

Nevertheless, the fit of the high resolution spectra of the C1s peak fully meets the theoretical amount of each species. A carbonate signal, assigned to the methacrylate, could be detected as well, but for a quantitative determination the integral is too close to the resolution limit.

Higher certainty is obtained from the O1s spectra. Beside the peak allocated to the methacrylate (COO*) and the MABP (COO*R), peak A and B contain species that reflect the crosslinking density. Upon irradiation with UV-light, Ar-C=O transforms into Ar-C-OH, yet, these changes are below the resolution limit and no significant trend was observed.

The N1s (see inset of fig. 4.5 right) exhibits only one peak as expected, since the hydrogel only contains one nitrogen species, which is the amide of the NIPAAm.

4.3 Conclusion

Thorough investigations on the composition of the hydrogel were conducted. Firstly, the uncrosslinked terpolymer was studied by NMR, revealing a composition, which is contrary to earlier results. The terpolymer consists of 94% NIPAAm, 5% methacrylic acid and 1% MABP, which is in excellent correspondence to the composition of the monomer mixture. Moreover, these measurements showed the complex interaction between the methacrylic acid and the NIPAAm and determined the actual number of sites that can be functionalized.

The spincoated and crosslinked hydrogel was characterized by XPS. The attained composition meets the results of the NMR study and indicates in addition, that the crosslinking does not affect the chemical integrity of the polymer, at least to the limit of detection.

4.4 Experimental Part

TMS-ester Hexamethyldisilazane (1 mL, 4.7 mmol) was added to 85 mg terpolymer. After two days all volatiles were distilled off and the polymer was freeze dried from *tert.*-butanol.

Film preparation for XPS A thin hydrogel film of approximately 1.1 μm thickness was deposited on a 140 mm² BP-silane functionalized silicon chip by spin-coating from a 10 w% ethanolic solution. The coatings were irradiated 0 min, 30 min and 60 min respectively with a total energy density of 3.14 J cm⁻² and 6.28 J cm⁻², respectively.

5 Optical Characterization

A variety of optical methods were developed in the last decades and are well established today for the *in situ* characterization of thin films and interfaces. These techniques include IR and Raman spectroscopy,^[114] ellipsometry,^[115] optical waveguide mode (OWS)^[116,117], surface plasmon (SP)^[118–121] and surface plasmon enhanced fluorescence spectroscopy (SPFS).^[122] To detect processes with a surface plasmon resonance (SPR) sensors, surface plasmons are excited on the metallic sensor surface, primarily gold or silver, which are influenced by the changes of the refractive index in their field caused by the event.^[123] These changes induce variations in the propagation constant of the surface plasmons which can be observed in the reflected light. Additionally, if a Kretschmann-configuration is employed, optical waveguide mode spectroscopy (OWS) can be performed on the same setup (here referred to as SPR/OWS). For sufficiently thick or dense films that meet the requirements of a waveguide (see chapter 2.3), additional minima can be observed, corresponding to thickness and refractive index, which allow for more detailed characterization of these films.

5.1 Coupled Long Range Surface Plasmon (cLRSP) Spectroscopy

5.1.1 Introduction

The spectroscopy of coupled long range surface plasmons was a cooperation with Jakub Dostálek who invented the sensor chip and performed the measurements and Wolfgang Knoll. This section is already published.^[58]

Recently, the excitation of long range surface plasmons (LRSPs) enhanced SPR sensors.^[37,124,125] LRSPs are generated at a thin metallic film embedded between two dielectrics with similar refractive indices.^[126] This configuration led to a narrower resonance and the enhancement of intensity of the electromagnetic field enabling a higher penetration depth,^[127] as the surface bound wave can propagate along the metallic film with an order of magnitude lower damping than conventional SPs.

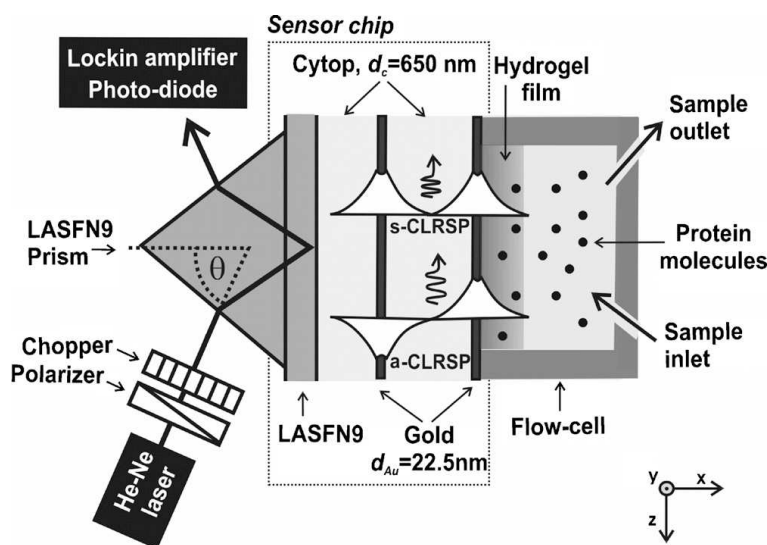


Fig. 5.1: Optical setup of a SPR sensor, modified to enable the excitation of coupled long range surface plasmons.

The spectroscopy of coupled long range surface plasmons (cLRSPs) is a new approach for the investigation of thin films. These modes can be excited in a layer structure of symmetrical refractive index with two metallic films along which the LRSPs propagate. A refractive index close to water is required for the dielectric media (in the present case the fluoropolymer Cytop) to keep symmetry with the investigated medium. The coupling of LRSPs across the gap between the metallic films gives rise to two new cLRSP modes with different penetration depths (see

fig 5.2). The spectroscopy of these modes allows for simultaneous measurement of the thickness and refractive index of studied thin films, whereas conventional SPR requires the knowledge of one parameter to determine the other. Moreover, it enables the interrogation of the distribution of measured events perpendicular to the sensor surface. In contrast to other reported approaches introduced to SPR sensors such as two-color SPR,^[118] multiple surface plasmon spectroscopy,^[128] spectroscopy of Bragg-scattered surface plasmons^[121] or spectroscopy of long range and short range surface plasmons,^[120] cLRSPs allow for the measurement at a single wavelength. Therefore, spectroscopy of cLRSP offers the advantage of observing variations of the refractive index without being affected by the dispersion of the involved materials. In addition, the cLRSPs sensor chip can easily be employed by other SPR-based techniques for the investigation of thin films and interfaces such as SPFS. The potential of the cLRSP sensor depicted in figure 5.1 was demonstrated by investigating the swelling of thin hydrogel films and the diffusion of protein molecules through these gels.

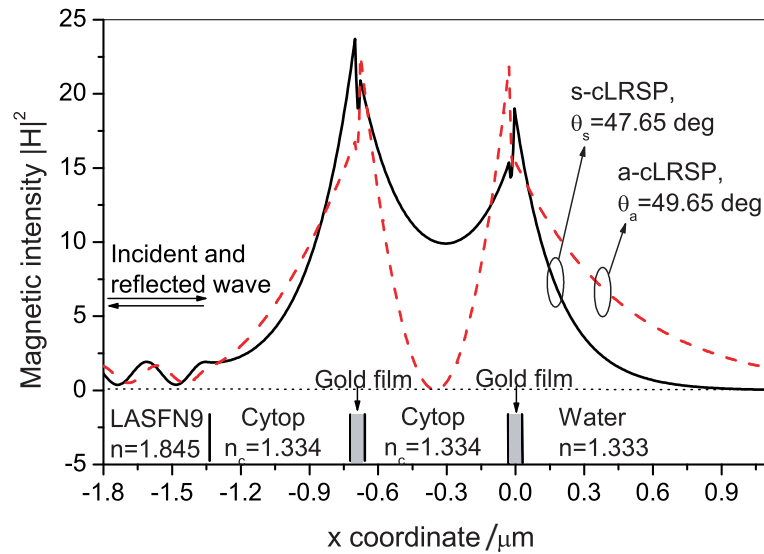


Fig. 5.2: Magnetic field intensity distribution of the symmetrical (solid line) and the anti-symmetrical (dashed line) cLRSP.

5.1.2 Thin Hydrogel Layers and Diffusion of BSA

As shown in figure 5.2, the cLRSPs, which are originated from the coupling of the two LRSPs, particularly the symmetrical (s-cLRSP) and anti-symmetrical mode (a-cLRSP) exhibit different penetration depths of $L_p = 364$ and 950 nm, respectively, into the aqueous medium. Therefore, these modes show different sensitivity to refractive index changes occurring at different distances perpendicular

to the sensor surface. As can be seen in the angular reflectivity spectra (fig. 5.3 and 5.4) the excitation of a-cLRSP and s-cLRSP modes is manifested by two distinct dips in the reflectivity spectrum with resonance angles of $\Theta_s = 47.63^\circ$ and $\Theta_a = 49.63^\circ$, respectively.

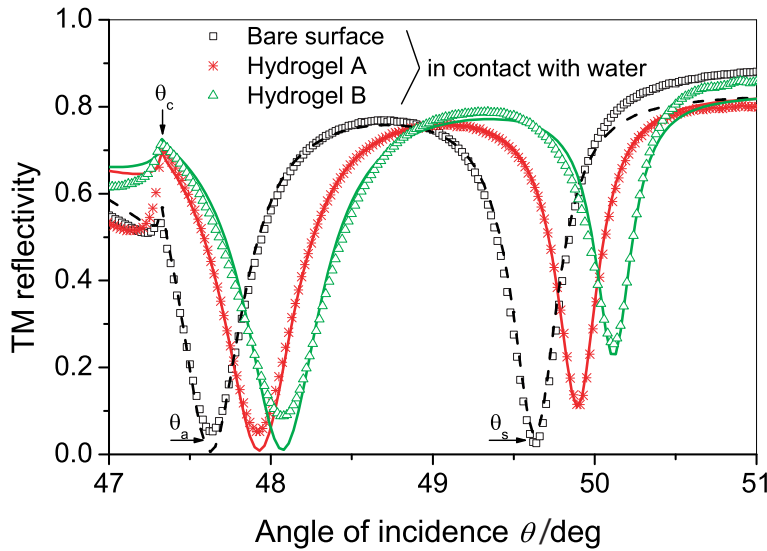


Fig. 5.3: Angular reflectivity spectra of the low crosslinked hydrogel layer A (asterisk) and the highly crosslinked hydrogel layer B (triangle) (see experimental part, section 5.1.4) compared to spectra measured for a bare gold surface (square) in contact with water. Fitted reflectivity spectra are shown for each sample (lines).

The fitting of the measured spectra (fig. 5.3) of the low crosslinked hydrogel A and the highly crosslinked B was performed assuming a constant refractive index n_h through the hydrogel films. It revealed that the hydrogel B had a lower thickness ($d_h = 612$ nm) and a higher refractive index ($n_h = 1.3521$) than hydrogel A ($d_h = 682$ nm and $n_h = 1.3438$). These results indicate that, as expected, for higher crosslinking time a denser and less swollen hydrogel film is prepared. For the preparation see the experimental part, section 5.1.4.

In addition, the pH-dependent swelling (fig. 5.4) of the hydrogel layer B was investigated in buffers with pH 4 (10 mM acetate buffer, refractive index of $n_b = 1.3344$) and pH 7.4 (10 mM phosphate buffer saline, refractive index of $n_b = 1.3349$). At pH 7.4 a higher thickness and a lower refractive index ($d_h = 790$ nm and $n_h = 1.3490$) was observed compared to pH 4.0 ($d_h = 611$ nm and $n_h = 1.3534$). This behavior is caused by repulsive forces between the carboxyl groups of the methacrylic acid ($pka \approx 5.5$ ^[129]) within the hydrogel film, which are negatively charged at higher pH.

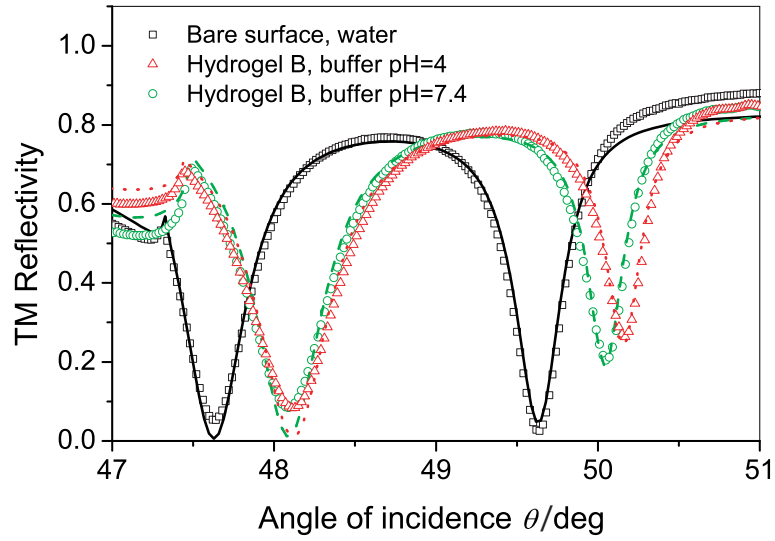


Fig. 5.4: Angular reflectivity spectra of the hydrogel layer B swollen in a buffer with pH 4 (tri-angle) and pH 7.4 (circle), and the bare gold surface (square) in contact with water as reference.

The diffusion of a bovine serum albumin (BSA) through the hydrogels was investigated by measuring the time evolution of changes in the resonance angles $\Delta\Theta_a(t)$ and $\Delta\Theta_s(t)$ (fig. 5.5). Prior to the addition of the protein the sensor surface was rinsed with pure buffer for 2 min in order to establish a baseline.

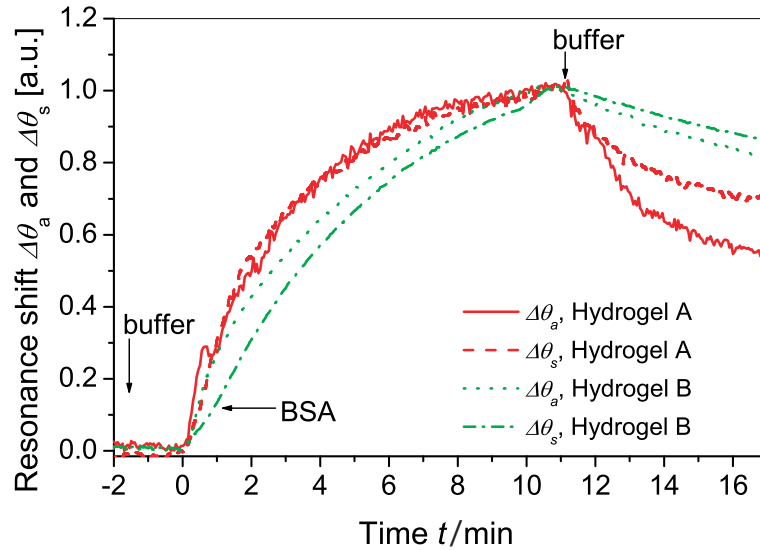


Fig. 5.5: Time evolution for $\Delta\Theta_a(t)$ and $\Delta\Theta_s(t)$ upon the diffusion of BSA into the low crosslinked hydrogel A (solid line - $\Delta\Theta_a(t)$, dashed line - $\Delta\Theta_s(t)$) and the highly crosslinked hydrogel B (dotted line - $\Delta\Theta_a(t)$, dash-dotted line - $\Delta\Theta_s(t)$)

Subsequently, a solution of BSA (2.5 mg/mL) in a 10 mM acetate buffer at pH 5.5 was pumped through the flow-cell for 10 min. Afterwards, the sensor surface

was rinsed with the pure buffer. The measured time evolutions in figure 5.5 show that Θ_a and Θ_s shifted to higher angles of incidence upon the diffusion of BSA into the hydrogels, visualizing an increase of its refractive index n_h . A refractive index increase of $\delta n_h = 1.8 \times 10^{-3}$ and 3.6×10^{-3} was observed for the hydrogel A and B, respectively. Contraintuitively, this indicates that the denser hydrogel was capable to take up a larger amount of BSA from a solution with pH 5.5 than the less dense one. The diffusion of BSA to the hydrogel was probably driven by ionic interaction between the methacrylate and the protein which is positive charged at pH 5.5. The lack of uptake of BSA at pH 4 where the methacrylate and pH 7.4 where the protein is less charged corroborates this concept. Furthermore, figure 5.5 shows that the sensor response approaches the equilibrium faster for the hydrogel A than for the hydrogel B indicating that the diffusion is slower in a denser gel. Additionally, one can see that the initial slope of the sensor response ($d\Theta/dt$) measured for the angle Θ_a is higher than that for Θ_s . The reason for this observation is the different penetration depth of the two cLRSP. The field of a-cLRSP excited at the angle Θ_a penetrates deeper into the hydrogel film where BSA molecules approach earlier from the solution. The s-cLRSP mode excited at the angle Θ_s probes the region closer to the gold surface which is reached by the diffusing BSA molecules at a later stage.

5.1.3 Conclusion and Outlook

New surface plasmon modes – cLRSPs – were excited on the surface of a SPR sensor by using a layer structure with two thin metallic films embedded in layers of similar refractive index. cLRSPs were used to simultaneously probe the sensor surface by their evanescent fields of different penetration depths into the medium on its top. This feature enabled the measurement of the distribution of refractive index changes perpendicular to the sensor surface. Furthermore, for thin films which are not accessible to OWS the thickness and the refractive index of an attached film can be determined independently which extends the performance of current SPR sensors. The cLRSP-based sensor allowed for the investigation of the swelling of hydrogel films on the sensor surface which are too thin to guide light waves. Furthermore, it enabled following the diffusion of protein molecules into these gels. Simultaneous probing of thin hydrogel layers by cLRSP modes will therefore provide the possibility of future investigations of more complex structures (e.g. the diffusion through a hydrogel film with a gradient perpendicular to the surface) and determination of important parameters (e.g. diffusion coef-

ficients) through the analysis of kinetics $\Delta\Theta_a(t)$ and $\Delta\Theta_s(t)$ and fitting with an appropriate model.

Decisive for future experiments on protein diffusion and attachment towards an application as biosensor matrix, is the discovery of the charge dependence of the diffusion.

5.1.4 Experimental Part

The sensor chip was prepared on a LASFN9 glass slide as shown in the figures above by coating low refractive index polymer layers (Cytop, CTL-809M, ASAHI Inc., Japan) with a thickness of $d_C = 650$ nm and a refractive index of $n_C = 1.3395$. Gold layers were deposited with the thickness of $d_{Au} = 22.5$ nm and their refractive index was determined as $n_{Au} = 0.3 + 3.5i$.^[127] As described in chapter 3.2 the top gold surface was functionalized with BP-thiol and the hydrogel-polymer was spincoated from a 2 weight% ethanolic solution. The thickness of the dry hydrogel layer was measured with a surface profiler to be 83 nm. Hydrogel films were investigated with two different crosslinking densities prepared by irradiating the hydrogel-polymer films A and B with 1.5 and 4.0 J cm⁻², respectively. Before taking a cLRSP spectra the crosslinked hydrogel films were immersed in the respective buffer for one hour.

5.2 WKB-assisted SPR/OWS

5.2.1 Introduction

A common method to analyze SPR or SPR/OWS data is to assume a homogeneous and average refractive index for the whole film. For more complex systems with gradients in density or refractive index, this simplified model (box-model) may result in unreliable film parameters or even preclude the fitting of the measured spectra. For such inhomogeneous films or such with an artificial gradient, the reversed Wentzel-Kramers-Brillouin (WKB)-approximation (see chapter 2.3.1) can be applied to determine the variation of the refractive index perpendicular to the surface. WKB was initially developed for the analysis of the diffusion of ions in inorganic waveguides.^[130] This tool assigns the measured effective refractive index N_{effm} for each mode with a distance from the surface, where the oscillating and the evanescent solution of the wave function are identical. Beines *et al.*^[99] successfully employed the reversed WKB-approximation in the investigation of thin hydrogel films. The readout of the coupling angles was performed with custom software coded by Andreas Unger, the WKB-calculations were conducted by Bernhard Menges.

5.2.2 Gradient Fitting

To determine the limits of the WKB-approximation and to demonstrate its potential to support the fitting of more complex structures, an artificial gradient within the hydrogel was created. A step like profile was fabricated by spincoating a second polymer film on top of an already crosslinked polymer layer. Upon the second crosslinking a sharp gradient in the refractive index arises, forming a two layer system with a lower layer crosslinked 60 min (6 J cm^{-2}) over all and a 30 min (3 J cm^{-2}) crosslinked upper one.

Figure 5.6 shows the measured spectrum of the hydrogel in the swollen state in water (interconnected black dots). The red fit curve was obtained by applying the box-model, the thickness was adjusted to match the simulated position of T_{M1} to its experimental value. Subsequently, the refractive index was adjusted to match the simulated position of T_{M12} (generally, T_{Mn} for a spectrum with n modes) to the last waveguide mode.

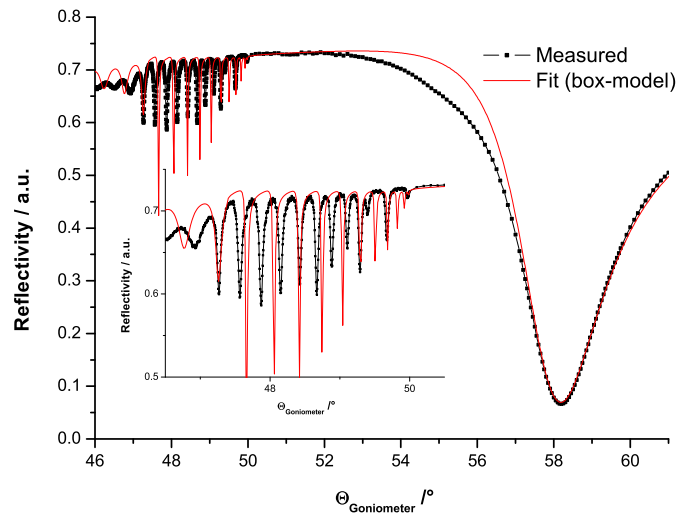


Fig. 5.6: Reflectivity spectra of the hydrogel with artificial gradient (60/30 min) in the swollen state in water (interconnected dots) and the box-model fit (solid).

This abortive attempt clearly illustrates that the box-model is inappropriate for more complex structures, as most of the other modes do not match. The coupling efficiency – the depth of the modes – is decreased by the inhomogeneity of the gel, which is taken into account by setting the absorption constant k to 0.0001. It nicely illustrates the sensitivity of the waveguide modes towards the absorption constant or the imaginary part of the dielectric constant.

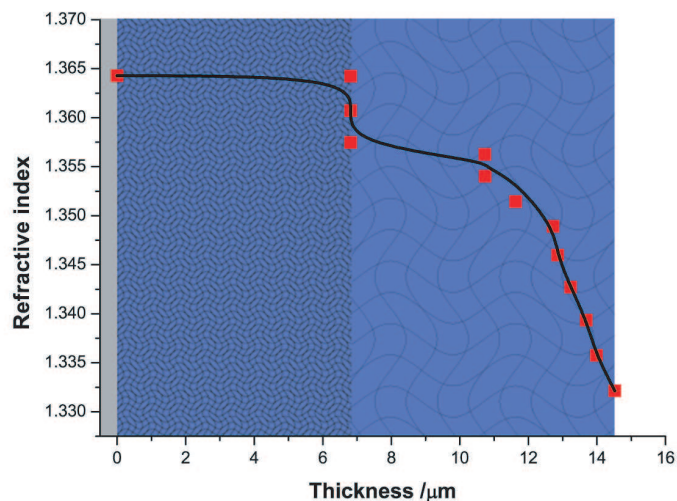


Fig. 5.7: Evolution of the refractive index perpendicular to the surface, as calculated by the reversed WKB method. The measured refractive indices at calculated distances (squares) are connected to guide the eye.

The reversed WKB-approximation was employed to resolve the course of the refractive index inside the hydrogel as depicted in figure 5.7. It shows two well separated areas of different refractive index. In line with literature^[59,60,99] the highly crosslinked layer close to the silver surface exhibit a lower swelling ratio ϕ ($\phi \approx 6$ for a crosslinking dose of 6 J cm^{-2}) than the lower crosslinked on top ($\phi \approx 9$ for a crosslinking dose of 3 J cm^{-2}). The red squares are the experimental measured refractive indices at distances from the silver surface calculated by the reversed WKB-approximation, the black line is a guide to the eye.

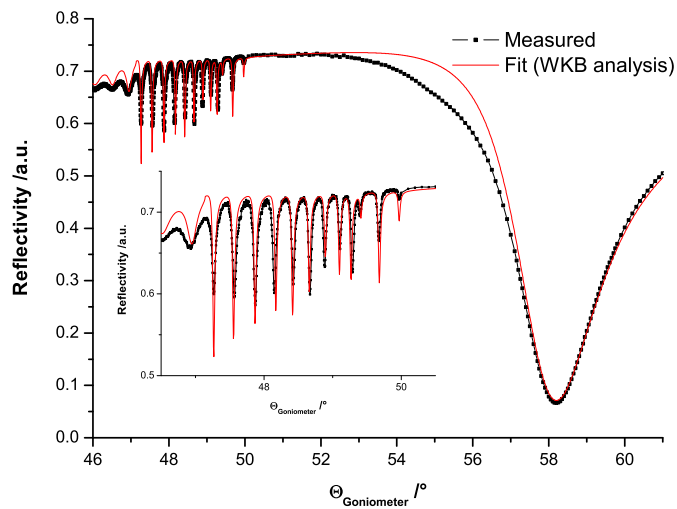


Fig. 5.8: Reflectivity spectra of the hydrogel in the swollen state in water (interconnected dots) and the fit of the WKB analysis (solid).

To verify this data and fortify the method, the refractive index gradient was segmented into six boxes of average refractive index (the number of segments should not be higher than half the amount of modes to avoid underdetermination). Indeed, applying these six boxes to fit the spectrum allowed for a proper description of the hydrogel film, as the fit nicely matches the measured spectra (fig. 5.8). After all, this fit was only performed to validate the method, as all information can be obtained from the refractive index profile in figure 5.7.

5.2.3 Conclusion and Outlook

A combination of SPR and OWS was applied to determine the optical properties of a film thick enough to guide light waves. These waves induce additional reflectivity minima corresponding to refractive indices and thicknesses. This increase in the amount of data enables a more reliable description of the hydrogel. The reversed Wentzel-Kramers-Brillouin (WKB)-approximation was employed to support and simplify the treatment of these spectroscopy data. Even for complex structures it allows for a fast and verifiable analysis and depiction of the gradient in refractive index with the thickness.

Furthermore, WKB-assisted SPR/OWS gives rise to the investigation of the diffusion of non-fluorescent and weakly scattering probes inside the hydrogel as carried out in section 6.1.5.

The application of the reversed WKB-approximation in the evaluation of SPR/OWS data is subject to ongoing research. One focus is to quantify the error in the assignment of a distance from the surface to the measured refractive index.

5.2.4 Experimental Part

To obtain the artificial gradient, in a first step hydrogel-polymer was spincoated on the benzophenone functionalized silver surface of a SPR/OWS slide. Spincoating a 10 w% ethanolic solution gave a $\sim 1 \mu\text{m}$ thick film. After crosslinking with a dose of 3 J cm^{-2} a second hydrogel-polymer layer was spincoated on top with the same parameters. A second crosslinking provided the connection between the layers and resulted in a total crosslinking dose of 6 J cm^{-2} for the first and 3 J cm^{-2} for the second layer.

6 Dynamic Characterization

6.1 Tracking-Probe Diffusion

6.1.1 Introduction

Studying the diffusion of particles inside a hydrogel gained a lot of interest since this issue^[131] affects the performance of these networks when applied e.g. in drug delivery, cell encapsulation and biosensing. Additionally, the influence of the gel on the particle motion allows for the inference on the properties of the host.

Although PNIPAAm-based gel have commonly been studied for drug delivery applications,^[132] the diffusion of probes inside them is still subject to extensive research.^[133–135] The quantity of factors influencing the diffusion and the interdependencies between probe and host are poorly understood. However, the role of the relation between diffusant size and mesh size is widely accepted.

Firstly physical PNIPAAm networks in ethanol were investigated by fluorescence correlation spectroscopy (FCS), as their concentration dependent mesh size can be determined by photon correlation spectroscopy (PCS). FCS was employed to probe both the local and the global transient polymer network dynamics. These information about tracer diffusion in transient gels can then be utilized to provide structural information of grafted chemically crosslinked PNIPAAm films of different crosslinking densities. The different crosslinking densities can be put in relation to the different concentrations of the physical networks.

To enhance this approach, PCS can be used to study the diffusion of non-fluorescent but intensely scattering probes in physical, transient gels as well.

The diffusion of non-fluorescent and weakly scattering probes on a much larger length scale can be achieved by the spectroscopy of surface plasmons and optical waveguides as well, as introduced in section 5.1.

6.1.2 FCS of Rhodamine 6G Diffusion

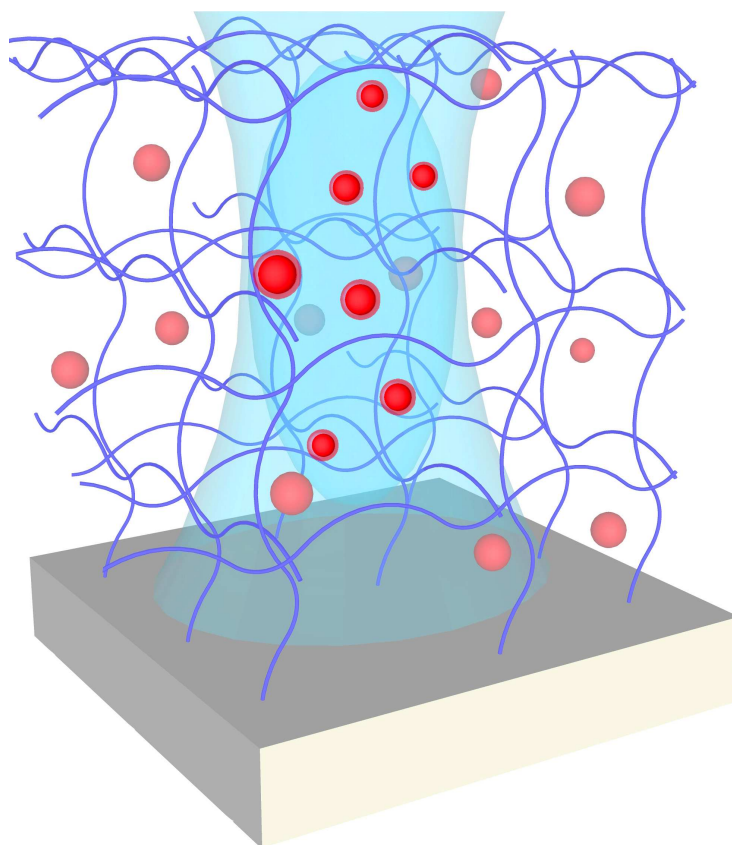


Fig. 6.1: Schematic illustration of the focal volume of a confocal FCS measurement inside a grafted crosslinked gel. Courtesy of Fabian Roskamp.

The investigation of diffusion inside the transient and crosslinked hydrogel by FCS was a cooperation with Maria Gianneli who performed the measurements, Patrick Beines who initially provided the hydrogel, Kaloian Koynov, Georg Fytas and Wolfgang Knoll. More details can be found in the published paper.^[59]

FCS^[76,136,137] can be used to determine the dynamics of supported PNIPAAm network films by measuring the diffusion of fluorescent particles. This method has been successfully utilized to study transport properties in various biological environments,^[76,136,137] however, the transfer to other systems was only recently achieved.^[138–144] FCS features a very small detection volume in the order of femtoliters and a high sensitivity. This enables studying single tracer diffusion in thin, supported gels and the respective free polymer as presented below.

6.1.2.1 Diffusion in the Free Polymer

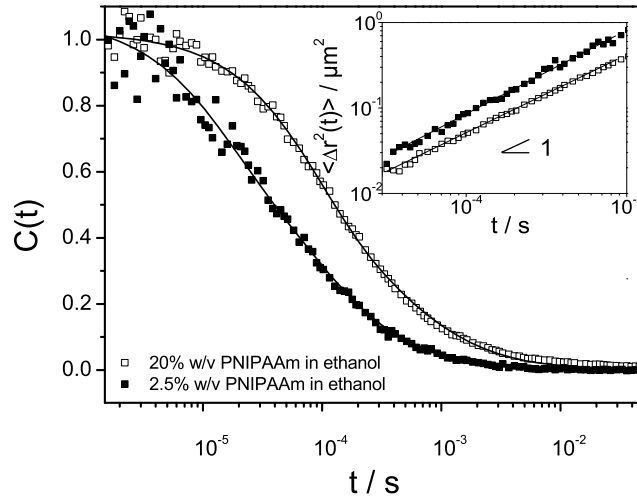


Fig. 6.2: Normalized fluorescence intensity correlation function $C(t)$ of Rh6G in two ethanolic PNIPAAm solutions in the semidilute regime and the respective fits (solid lines). The diffusive mean square displacement (slope one in a double log plot) is shown in the inset.

To compare the diffusion coefficient of Rh6G inside a transient gel and its mesh size, FCS of Rh6G in differently concentrated ethanolic PNIPAAm solutions was measured. Figure 6.2 shows the net experimental normalized correlation functions $C(t)=G(t)-1$ for the diffusion of Rh6G in two ethanolic PNIPAAm solutions in the semidilute regime at 20°C . The concentration was near and well above the overlap concentration c^* (~ 0.4 w%). The function was fitted assuming a single component according to equation 2.24 in section 2.4.1. The inset to Figure 6.2 displays the mean square displacement $\langle \Delta r^2(t) \rangle$ of the small dye as a function of time t , excluding the initial decay times. The slope 1 implies that $\langle \Delta r^2(t) \rangle \sim t$, which indicates a purely random Brownian diffusion, though the high concentration slightly deviates. The experimental diffusion time τ_D is directly translated to the self-diffusion $D_s(c)$ of the Rh6G in ethanolic PNIPAAm solutions for concentration from 1×10^{-4} to 0.2 g/cm³.

For a probe that does not interact with the polymer segments and given that the particle size (b) is smaller than the size of the polymer chain, D_s can be expressed as a function of the relevant length scales of the system, namely the mesh size (ξ) of the polymer network and the particle size (b). However, in the proposed scaling behavior $D_s \sim \exp(-b/\xi)$, there was no independent information on the mesh size. This characteristic size of a transient polymer network at $c > c^*$

is approximately the correlation length $\xi(c)$ representing the average distance between two adjacent contacts. PCS enables the determination of $\xi(c)$ and was therefor performed with the same ethanolic PNIPAAm solutions in the following.

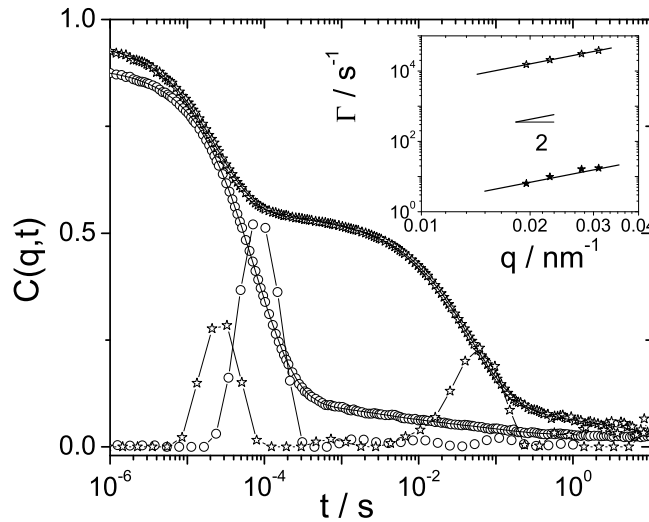


Fig. 6.3: PCS relaxation function $C(q,t)$ of the concentration fluctuations in dilute (circles, $c = 2.4 \times 10^{-3} \text{ g/cm}^3$) and semidilute (stars, $c = 5.4 \times 10^{-2} \text{ g/cm}^3$) ethanolic PNIPAAm solutions at $q = 0.031 \text{ nm}^{-1}$ and the respective relaxation time distributions. The inset shows the two diffusive (slope 2) relaxation rates for the semidilute solution.

Figure 6.3 left displays the relaxation function $C(q,t)$ for the concentration fluctuations at a wavevector $q = 0.031 \text{ nm}^{-1}$ in ethanolic PNIPAAm solutions for two concentrations in the dilute and semidilute regime. To analyze the relaxation function $C(q,t)$, the inverse Laplace transformation was applied to yield the distribution of relaxation times. The peak positions of a relaxation time gives the relaxation rate and the area under the peak defines the intensity associated with the particular process. In dilute solutions, $C(q,t)$ displays a single process associated with the translational diffusion $D_0 = \Gamma/q^2$ of the PNIPAAm. This process becomes the cooperative diffusion D_{coop} in the semidilute regime where a second slower process appears. Both exhibit a diffusive (q^2 dependent) rate as well, which can be recognized from the slope 2 in the double log plot in the inset of Figure 6.3 left.

The slow process might relate to the self-diffusion of PNIPAAm (PCS active due to polydispersity^[145]) or most likely to cluster diffusion^[146] and will be discussed in chapter 6.3.2. In the semidilute regime, $D_{coop}(c) (= k_B T / (6\pi\eta_s \xi))$ defines the mesh size $\xi(c)$ of the polymer network.

For the diffusion of Rh6G in ethanolic polymer solutions measured by FCS the plot of τ_D/η versus concentration in Figure 6.4 shows that the solution viscosity $\eta(c)$ increases much stronger with c than the dye self-diffusion time, $\tau_D(c)$.

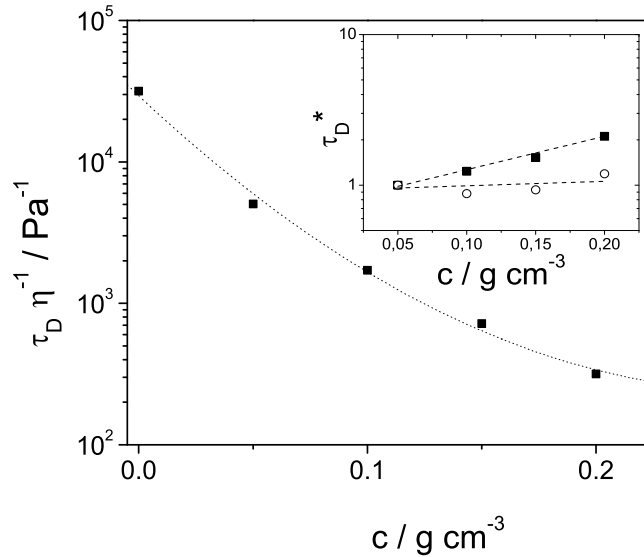


Fig. 6.4: Diffusion time τ_D of Rh6G in ethanolic PNIPAAm solutions normalized to the solution viscosity as a function of the PNIPAAm concentration. The inset shows the two proposed relations for the reduced diffusion time τ_D^* with the mesh size ζ as a function of the polymer concentration: $\tau_D(c)\exp(-b/\zeta(c))$ (solid) and $\tau_D(c)(\zeta(c)/b)^{5/3}$ (open).

The reduced diffusion time, $\tau_D^* \equiv \tau_D(c)\exp(-b/\zeta(c))$,^[147,148] should be virtually independent of the polymer concentration. Apparently, this is not the case since τ_D^* increases by a factor of 2 in the examined concentration range as shown (solid symbols) in the inset of Figure 6.4.

Transferring the physical picture of Rouse chains^[147] from polymer melts to semi-dilute solutions in good solvents, one obtains the scaling $\tau_D^* \equiv \tau_D(c)(\zeta(c)/b)^{5/3}$ with $\tau_D(c) \propto b(b/\zeta(c))^{5/3}$ which should be insensitive to the variation of polymer concentration. In fact, this τ_D^* (open points in the inset to Figure 6.4) displays a much weaker concentration dependence as compared with the alternative exponential relation. This corroborates the notion that the observed slowing down of the small probe diffusion, roughly by a factor of five, is mainly due to the reduction of the mesh size with polymer concentration. In the following chapter 6.1.2.2, this relation will be utilized to estimate an effective mesh size in chemically cross-linked and grafted gels.

6.1.2.2 Diffusion in the Crosslinked Hydrogel

FCS is employed to measure the tracer diffusion time τ_D to estimate an effective mesh size in grafted crosslinked PNIPAAm. To compare the concentration of a transient gel with the crosslinking density via volume fraction calculation, the swelling ratio κ has to be determined. This can be achieved for the gels cross-linked for a given UV exposure time T_{UV} through scanning of the probed volume from the glass substrate to the bulk solvent. The swelling ratio κ was defined as ratio between the thickness of the dry gel and the thickness of the grafted gel in the swollen state, which was between 4 and 8 μm ($\pm 1 \mu\text{m}$) for the examined crosslinking densities.

The normalized correlation functions for the diffusion of Rh6G in two differently crosslinked grafted PNIPAAm gels (cartoon in the inset) swollen in ethanol is depicted in figure 6.5. The swelling ration κ was 10.9 and 4.5 respectively for $T_{UV} = 15 \text{ min}$ and 4 h. In this range it was found that $\kappa \sim T_{UV}^{-0.3}$. Figure 6.5 shows the slowing down of the probe with T_{UV} , which origins in the reduced swelling ratio and therefore smaller mesh size.

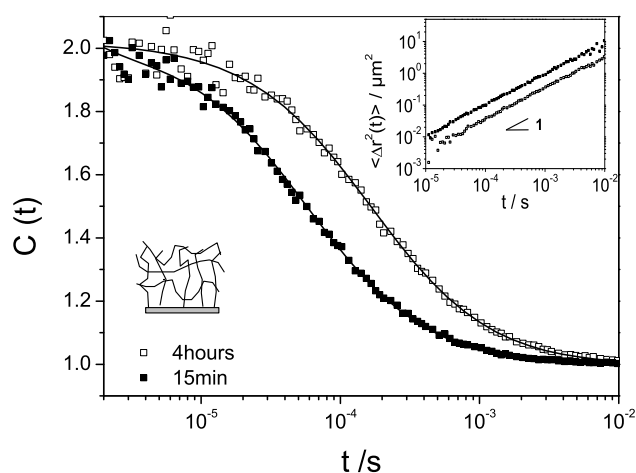


Fig. 6.5: Normalized fluorescence intensity correlation function $C(t)$ for Rh6G in two grafted highly and low crosslinked PNIPAAm films (lower inset) swollen in ethanol. The mean square displacement of the single Rh6G is diffusive (slope one in double log plot) as shown in the inset.

Interestingly enough, the crosslinking time does not affect the purely diffusive random translation of the probe as indicated by the slope of one in the upper inset to Figure 6.5. The same behavior was found for different concentrations of the semidilute solutions of Figure 6.2. This is a pertinent finding given the, in general, inhomogeneous structure of gels^[149–151] but might be related to the short

time interval of the small dye in V_{obs} (eq 2.23 in section 2.4.1).^[144] The diffusion time $\tau_D(T_{UV})$ obtained from the representation of $C(t)$ by eq. 2.24 (section 2.4.1) is plotted in Figure 6.6 for five PNIPAAm gels prepared with different crosslinking times T_{UV} . The characteristic average mesh size ζ of these gels can be estimated assuming the relation $\tau_D(c) \sim (\zeta(c)/b)^{-5/3}$ used for the semidilute ethanolic PNIPAAm solutions (inset in Figure 6.4). With this assumption, the average mesh size plotted in Figure 6.6 decreases from 4.4 nm for a 15 min crosslinked to 2.7 nm for a crosslinking time of about 4 h. Longer T_{UV} exposure times do not seem to lead to a significant increase of the crosslinking density.

The presented PNIPAAm gels swollen in ethanol followed the relation $\tau_D \sim \kappa^{-1}$ over the examined T_{UV} range. Given the complexity of the gels, this relation should depend on their preparation as well as on the swelling conditions, for example solvent quality and temperature, since it reflects inhomogeneities in the gels.

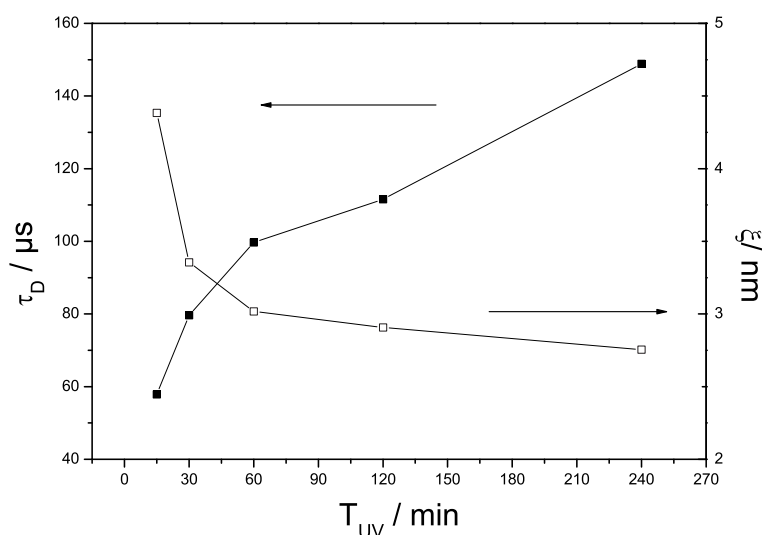


Fig. 6.6: Diffusion time τ_D (solid of Rh6G in grafted crosslinked PNIPAAm gels swollen in ethanol) as a function of the crosslinking time T_{UV} . The calculated average mesh size ζ (open) is decreasing with T_{UV} .

Beside the determination of the mesh size, tracking probes gives insight into the gels rheology. The elastic modulus $G(c) \sim k_B T / \zeta^3(c)$ can be estimated from $\tau_D(c)$. In fact, it was recently reported that there is a linear correlation between the diffusion of a small dye and the elastic modulus of crosslinked poly(vinyl alcohol) gels.^[141]

6.1.3 FRET-excited FCS

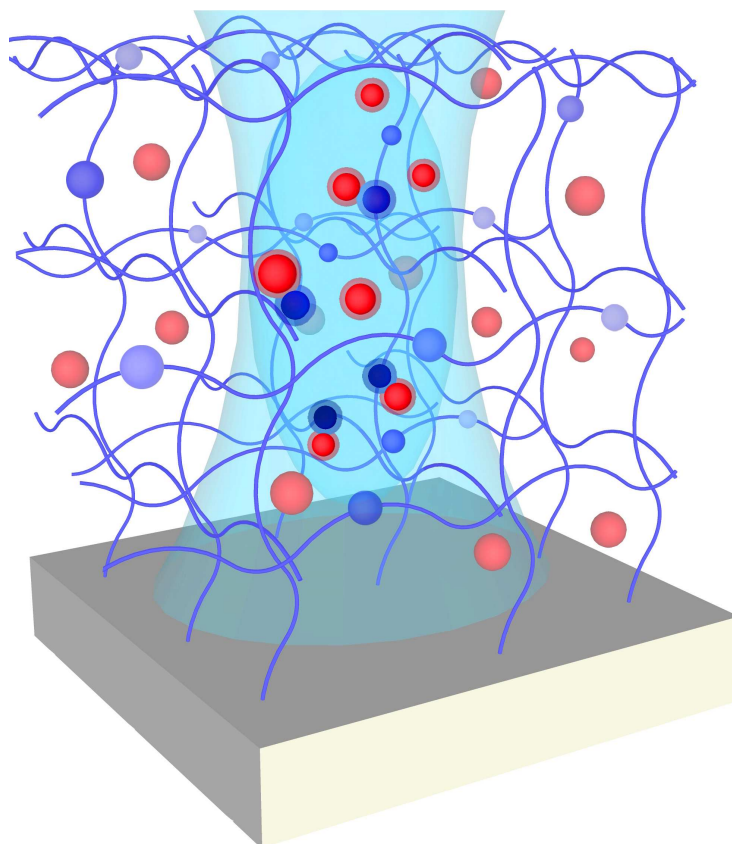


Fig. 6.7: Scheme of the principle of FRET excited FCS. The energy is transferred from the diffusing to the attached fluorophores within the Förster-radius. Courtesy of Fabian Roskamp.

The detection volume limited by a confocal objective in the case of confocal FCS can be further decreased to gain higher sensitivity and enable investigation on smaller length scales. This can be achieved by objectives with higher aperture, however limited by diffraction. To overcome this limit fluorescence resonance energy transfer (FRET) will be applied to excite a second fluorophore with a first being excited by conventional confocal FCS (see fig. 6.7). This pair of fluorophores, referred to as donor and acceptor, has to fulfill certain criteria. First, the absorption spectra of the acceptor must overlap with the emission spectra of the donor, the degree of overlap is called spectral overlap integral (J). Second, the transition dipoles orientation needs to be parallel, but assuming that the pair is compatible, the main factor is the distance r between them. The energy transfer efficiency is given by

$$E_{trans, eff} = \frac{R_0^6}{R_0^6 + r^6} \quad (6.1)$$

The Förster-radius R_0 is the distance where 50 % of the energy is transferred according to eq. 6.2:

$$R_0 = (8.8 \times 10^{23} \kappa^2 n^{-4} Q_D J)^{1/6} \text{ \AA} \quad (6.2)$$

Equation 6.2:

κ - dipole orientation factor; n - refractive index of the solvent; Q_D - fluorescent quantum yield of the donor in the absence of the acceptor.

Typical values are in the order of 1 to 10 nm.

By carefully choosing the fluorophore pair and attaching one of them to the hydrogel or the respective terpolymer, the detection volume will be reduced to the order of 10^{-24} L. This might allow for the investigation of diffusion at the typical confocal FCS length scale with the diffusing dye and at the same time at a length scale in the order of few nanometer via FRET to the attached dye.

The acceptor dye, connected to the hydrogel has to meet two important requirements. First, it must not absorb light in the UV range, as the labeled terpolymer has to be crosslinked. Second, it must not adsorb light from the FCS laser, as this would cause a high level of noise and a bleaching of the dye. For these reasons Alexa 647 cadaverine, which fulfills both criteria, was covalently attached to the terpolymer (see experimental part), employing active ester coupling with EDC/PFP activation, as described in section 3.4. The fluorescence spectra of Alexa 647 (blue, absorption dashed, fluorescence solid line) and Alexa 488 (green, absorption dashed, fluorescence solid line) as possible mobile donor are depicted in figure 6.8, showing the required overlap and the absence of absorption of the acceptor (Alexa 647) in the UV range.

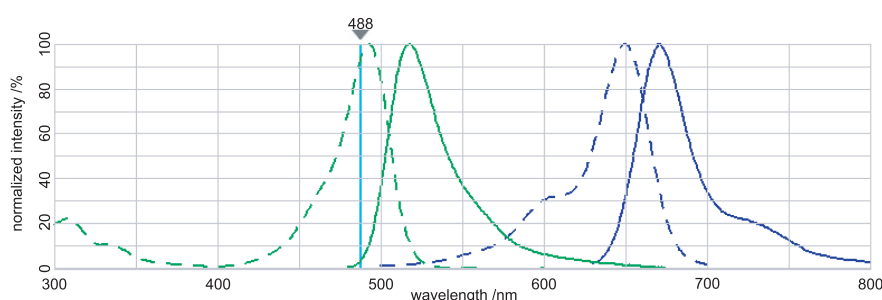


Fig. 6.8: The absorption (dashed) fluorescence spectra (solid) of Alexa 647 (blue), Alexa 488 (green) as possible mobile donor and the FCS laser wavelength of 488 nm, taken from invitrogen.com.

This project recently left the stage of synthesis and is now tested for implementation to FCS by Riccardo Raccis in our working group, hence only the preparation is presented here.

6.1.4 PCS of embedded Gold-Nanoparticles

Complementary to FCS, PCS can be employed to study the diffusion of analytes inside a network. For a network that scatters light itself like the hydrogel, a tracer has to be identified whose scattering intensity can dominate the whole system and therefore allow for the negligence of the scattering host. Although the scattering intensity depends on the size, gold-nanoparticles exhibit an intense scattering power and can be functionalized with a shell that interacts with the network. That gives rise to the investigation of diffusion inside the hydrogel via PCS of very diluted probe solutions in a host that scatters itself.

In the first experiments presented here, the interaction of Au-nanoparticles with the uncrosslinked terpolymer was studied. The Au-nanoparticles were synthesized on stock and were functionalized with different ligands (neutral, positive, and negative charged) by Marcus Schmelzeisen and enable non-charged as well as charge interaction. The laser wavelength of $\lambda=633$ nm was chosen to avoid absorption by the Au-nanoparticles, which would lead to a temperature increase within the sample. As these are preliminary results, only a qualitative discussion is accomplished.

At first, the influence of the polymer concentration on the polymer/particle mixture in the good solvent ethanol was investigated. Probing semidilute terpolymer solutions, which represent transient gels compared with measurements in covalently crosslinked gels allow for determining the structural differences of the two systems. Additional concentration dependent measurements are needed to include the concentration dependent friction, similar to the procedure performed in section 6.1.2. Furthermore, the diffusion of functionalized nanoparticles in dilute terpolymer solutions reveal the specific interaction between probe and host.

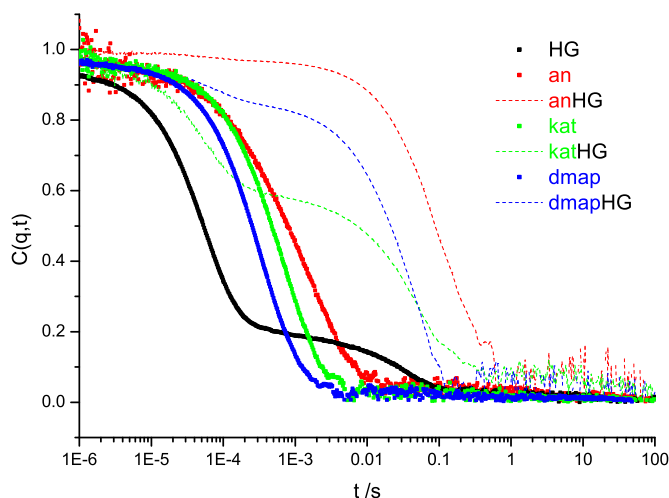


Fig. 6.9: Normalized relaxation functions $C(q = 0.019, t)$ of the concentration fluctuations of a semidilute ethanolic terpolymer solution (HG, $c = 79 \text{ g/cm}^3$), dilute ethanolic nanoparticle solutions ($c = 4 \times 10^{-8} \text{ mol/L}$, an: negative, kat: positive, and dmap: non-charged) and the corresponding mixtures (dashed lines).

Figure 6.9 shows the relaxation function of the semidilute ($c = 79 \text{ mg/cm}^3$) terpolymer (HG, black dots) with the two processes assigned to a fast cooperative diffusion and a slow cluster diffusion as discussed in section 6.1.2.1. The Au-nanoparticles in this ethanolic terpolymer solution are slowed down, compared to the polymer-free solution, to a relaxation rate in the order of the cluster diffusion process. The anionic charged particles (anHG, red dots) are more affected than the cationic (katHG, green dots) and the uncharged (dmapHG, blue dots). These relaxation functions still exhibit the fast process corresponding to the terpolymer. Even at these low Au-nanoparticles concentrations ($c = 4 \times 10^{-8} \text{ mol/L}$), they significantly increase the relative intensity of the slow rate whereas the cooperative diffusion rate of the terpolymer is unaffected. The scattering intensity of the terpolymer solution was 140 kHz, whereas the scattering intensity of the particles was 460 kHz for the anionic, 320 kHz for the cationic and 1000 kHz for the uncharged. The cationic and uncharged particles increase the relative scattering intensity of the particle/terpolymer mixture in relation according to their own scattering power. In contrast, the anionic particles created a much stronger scattering intensity. They might have formed bigger clusters as the slower rate, the intensity increase by a factor of 15 and a strong q -dependence suggests.

In dilute ethanolic terpolymer solutions (HGdilute, $c = 1.6 \text{ mg/cm}^3$), the Au-nanoparticles show a behavior that differs from the one in the semidilute regime.

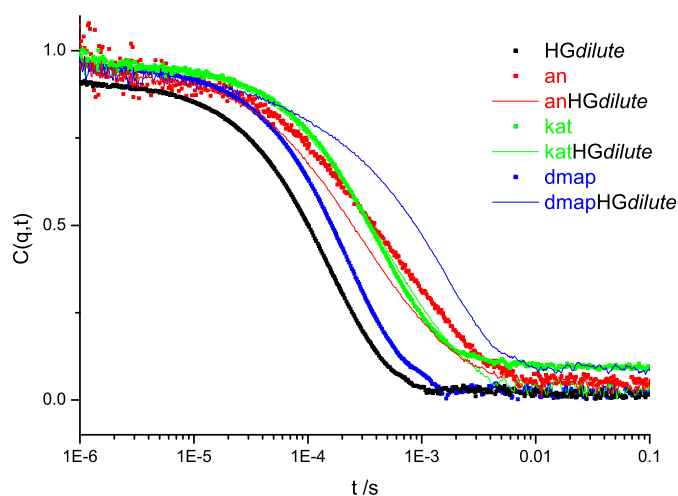


Fig. 6.10: Normalized relaxation functions $C(q = 0.023, t)$ of the concentration fluctuations of a dilute ethanolic terpolymer solution (HGdilute , $c = 1.6 \text{ mg/cm}^3$), dilute ethanolic nanoparticle solutions ($c = 4 \times 10^{-8} \text{ mol/L}$) and the corresponding mixtures (solid lines).

The relaxation function of the dilute ethanolic terpolymer solution exhibits only one process (see fig. 6.10) as described in section 6.1.2.1 with a scattering intensity of 85 kHz. The Au-nanoparticles experienced different effects, depending on their charge, caused by the terpolymer. The relaxation process of the uncharged (dmapHGdilute , blue line) particles was slowed down by a factor of ten, though the scattering intensity was decreased by a factor of 4 to 260 kHz compared to the ethanolic solution (dmap , blue line). In contrast, an increase in relaxation time was detected for the anionic (anHGdilute , red line), again accompanied by a decrease in scattering intensity to 170 kHz. The relaxation time of the cationic (katHGdilute , green line) is widely unaffected, but the scattering intensity decreased to 210 kHz, in the range of the other solutions. The interaction of the uncharged particles with the polymer might be higher than the cationic due to hydrogen bonding being stronger than ionic interaction in ethanol, as counter ions are condensed to the ionic groups. The clustered anionic particles might have been broken up by the polymer.

Secondly, the influence of the Au-nanoparticle concentration on a dilute ethanolic terpolymer/particle mixture was studied.

Compared to the relaxation function of the dilute ethanolic terpolymer solution as reference, by adding a low concentration ($c = 8 \times 10^{-10} \text{ mol/L}$) of anionic particles (diluteanHG), the process shift to a longer decay time and slightly increases the scattering intensity.

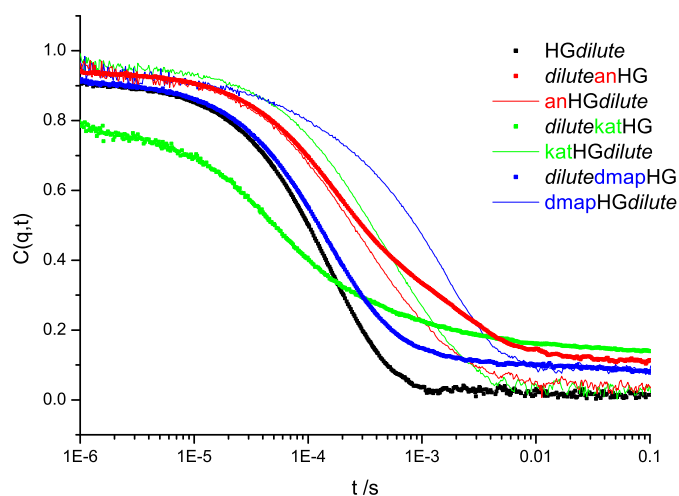


Fig. 6.11: Normalized relaxation functions $C(q = 0.023, t)$ of the concentration fluctuations of a dilute ethanolic terpolymer solution (HG_{dilute} , $c = 1.6 \text{ mg/cm}^3$), a mixture with low Au-nanoparticle concentration ($c = 8 \times 10^{-10} \text{ mol/L}$, e.g. $diluteanHG$), and a mixture with high particle concentration ($c = 4 \times 10^{-8} \text{ mol/L}$, e.g. $anHG_{dilute}$).

The addition of a low concentration of cationic particles ($dilutekatHG$) shows the contrary effect on decay time and scattering intensity. Adding a low concentration of uncharged particles ($dilutedmapHG$) only has a minimal effect on both values. Raising the particle concentration ($c = 4 \times 10^{-8} \text{ mol/L}$), however, strongly effects the relaxation process ($dmapHG_{dilute}$), that is being slowed down. With respect to the mixtures with a low concentration of particles the decay time of the cationic particles/polymer mixture ($katHG_{dilute}$) shifts to longer times whereas the decay time of the anionic particles/polymer mixture ($anHG_{dilute}$) slightly shifts to shorter times, thus having a faster relaxation process.

Additionally, the interaction between Au-nanoparticles and the terpolymer was analyzed in water, to enhance the charge effect of the particles with the ionic ligands.

Figure 6.12 shows the relaxation function of the dilute terpolymer solution in water. Its relaxation time is decreased by a factor of 15 compared to the ethanolic solution and its scattering intensity is increased by a factor of 20. Both indicate larger aggregates of the terpolymer in the solution and the scattering of the aggregates now exceeds the scattering of the Au-nanoparticles very clearly. The particles exhibit a shorter decay time compared to the polymer, in aqueous media (e.g. $aqan$, red squares) as well as in a mixture with the polymer (e.g. $aqanHG_{dilute}$, red dashed line).

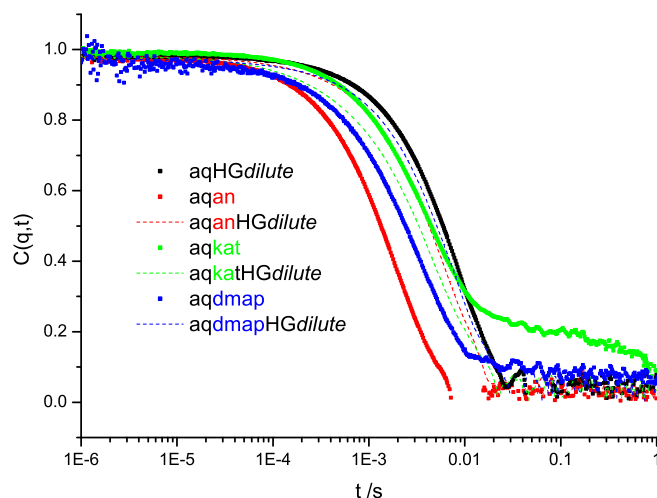


Fig. 6.12: Normalized relaxation functions $C(q = 0.013, t)$ of the concentration fluctuations of a dilute aqueous terpolymer solution (*HGdilute*, $c = 1.6 \text{ mg/cm}^3$), dilute aqueous nanoparticle solutions ($c = 2 \times 10^{-8} \text{ mol/L}$) and the corresponding mixtures (dashed lines).

Upon addition of cationic charged Au-nanoparticles to the dilute polymer solution (*aqkatHGdilute*, green dashed line), the relaxation process shifts to shorter times compared to the free particle (*aqkat*, green squares), whereas the addition of anionic and uncharged particles caused a shift to longer times.

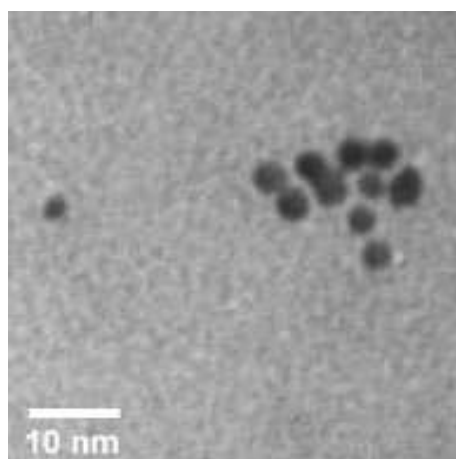


Fig. 6.13: TEM-image of the stock Au-nanoparticles.

If one compares the size of the nanoparticles in the TEM-images (see fig. 6.13) of roughly 4 nm with their relaxation times in PCS, it becomes clear, that a more detailed study has to be performed with particle solutions, being separated from their aggregates.

However, it was shown, that the investigation of diffusion phenomena by PCS in a scattering host, enabling Au-nanoparticles as strong scatterer, is feasible. In the good solvent ethanol, the scattering intensity of the particles exceeded the intensity of the terpolymer. This is not the case for aqueous solutions due to the formation of bigger terpolymer aggregates, which shows the limits of this approach.

For future experiments, studying a grafted gel, a terpolymer/particle mixture was spincoated on a glass slide and dark field images were taken. They nicely show the dominant scattering intensity of the Au-nanoparticles as showcased in figure 6.14.

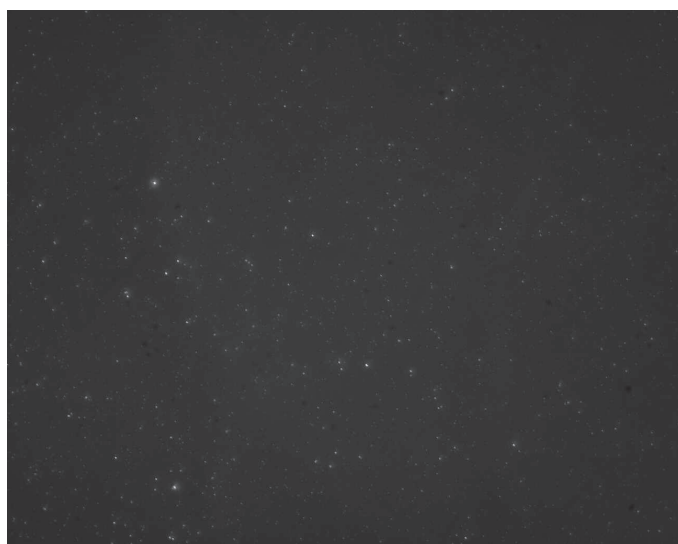


Fig. 6.14: Dark field image of Au-nanoparticles in a grafted and 60 min crosslinked hydrogel.

6.1.5 WKB-assisted SPR/OWS of Polymer Diffusion

In section 5.1 coupled long range surface plasmon were introduced to investigate the diffusion in thin hydrogel films of non-fluorescent probes with a similar or lower scattering power compared to the hydrogel, using the example of the protein BSA. For sufficiently thick enough films (> 600 nm) SPR/OWS can be employed. The waveguide modes exhibit additional electromagnetic fields with corresponding ‘penetration depths’ – the transition points of the respective mode (see section 2.3.1). These can, with the help of the WKB-approximation, provide a more detailed view on diffusion phenomena. Furthermore, this approach allows for studying diffusion in complex structures like gradients, whose optical characterization were described in section 5.2. Again, the readout of the coupling angles was performed with custom software coded by Andreas Unger, the WKB-calculations were conducted by Bernhard Menges.

Polyethylene glycol (PEG) with a molecular mass of $M_n = 20.000$ g/mol and a respective hydrodynamic radius of $R_h \approx 4.1$ nm in the order of the mesh size (see section 6.1.2.2) was used as tracer to grant a sufficiently slow diffusion. However, the diffusion time into the hydrogel detected by SPR kinetic (see fig. 6.15) was shorter than the time for a SPR/OWS scan.^[152] The delay between the addition of PEG and its detection by the field of the surface plasmon is caused by the diffusion through the $15\ \mu\text{m}$ thick hydrogel down to the penetration depth of the surface plasmon.

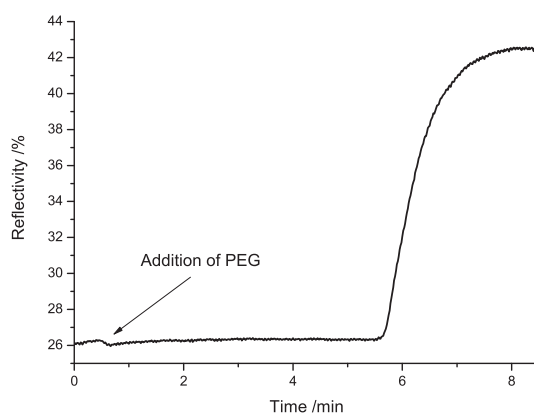


Fig. 6.15: Diffusion of PEG ($M_n = 20$ kg/mol) into a $15\ \mu\text{m}$ thick hydrogel with artificial gradient, discussed in section 5.2, detected by SPR.

Instead, the diffusion of PEG out of three different hydrogel layers was investigated by repeated angular scans. A low crosslinked ($T_{UV} = 30$ min), a highly crosslinked ($T_{UV} = 60$ min) and a hydrogel with an artificial gradient containing both crosslinking densities (see section 5.2) were loaded with PEG from a

250 mg/mL aqueous solution. By a continuous flow of pure water through the chamber, the diffusion of the PEG out of the gel was initiated. As reference the film prior loading ($t = -30$ min) and right before rinsing with pure water ($t = 0$ min) was measured. The shift of the coupling angle of the T_M modes for each film were plotted against time and evaluated using the WKB-approximation.

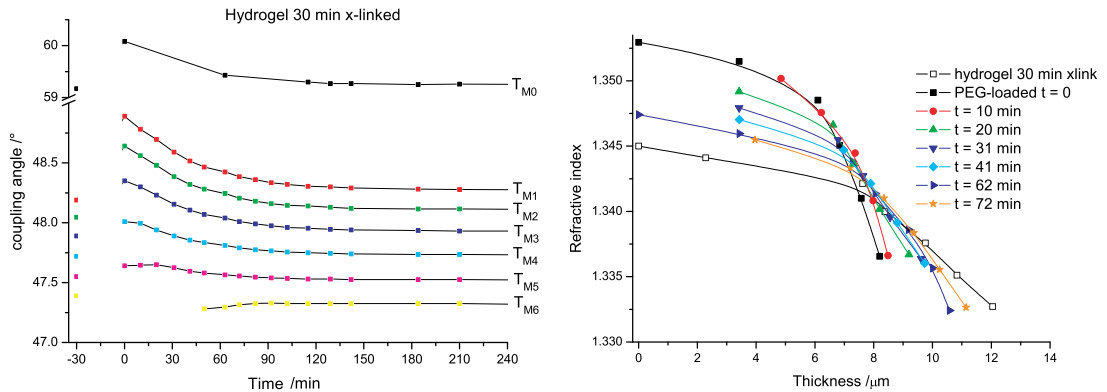


Fig. 6.16: Coupling angles of all T_M modes upon diffusion of PEG out of a 30 min crosslinked hydrogel (left) and the corresponding refractive index gradients calculated with the help of the WKB-approximation (right). All lines are to guide the eye.

Figure 6.16 depicts the diffusion of PEG out of a 30 min crosslinked film. The progress was visualized by the shift of the coupling angle with time. The change of the refractive index gradient with time was determined from the coupling angles with the help of the WKB-approximation. Interestingly enough, upon loading the gel with PEG beside the rising of the refractive index, the gel collapses to roughly 65% of the thickness of the PEG free film. While the PEG diffuses out, the gel returns to the thickness and refractive index before loading with PEG.

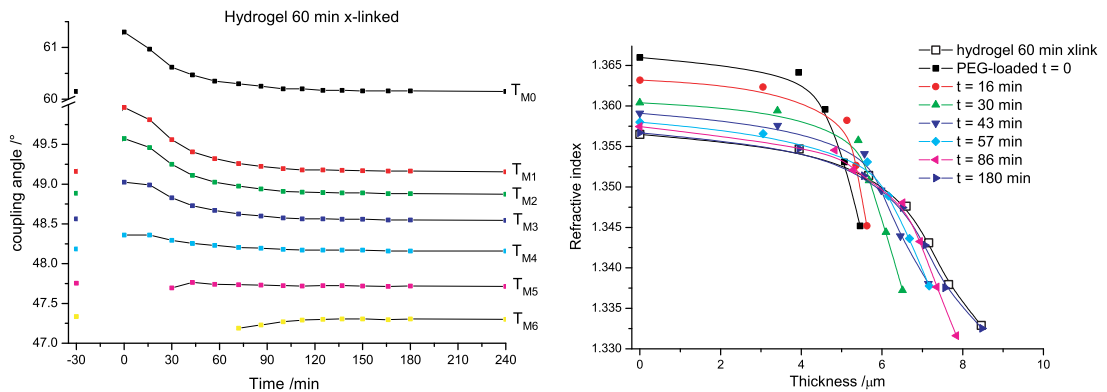


Fig. 6.17: Coupling angles of all T_M modes upon diffusion of PEG out of a 60 min crosslinked hydrogel (left) and the corresponding refractive index gradients calculated with the help of the WKB-approximation (right).

The same behavior was observed when loading a 60 min crosslinked film (see

fig. 6.17). The differences in crosslinking density can clearly be noticed from the sharper, more box-like gradient of the higher crosslinked gel.

The diffusion of PEG inside a hydrogel with an artificial gradient – a two layer system, crosslinked for 60 and 30 min respectively – can be shown by WKB-assisted SPR/OWS as well. Upon loading both layers take up PEG causing an increase of their refractive indices and collapsing to an extend similar to the respective one layer systems. Due to the shifting of the modes positions, the step-like gradient of the pure hydrogel (see fig. 5.7 in section 5.2 as well) is not visible anymore. However, since the slope between the data points (straight lines with $t=0$) and the reversibility of the loading indicates a persistence of the step, it was denoted by the lines to guide the eye. The position of the step was extrapolated from the measurement of the 60 min crosslinked gel.

The step-like gradient allows for a direct comparison of the two crosslinking densities in terms of their behavior upon taking up the PEG. If one contrasts the step height of the PEG-free gel with the loaded, a clear decrease is visible. The change in refractive index of low crosslinked layer exceeds the change of the highly crosslinked by 25%, which reveals the structural difference between the two crosslinking densities.

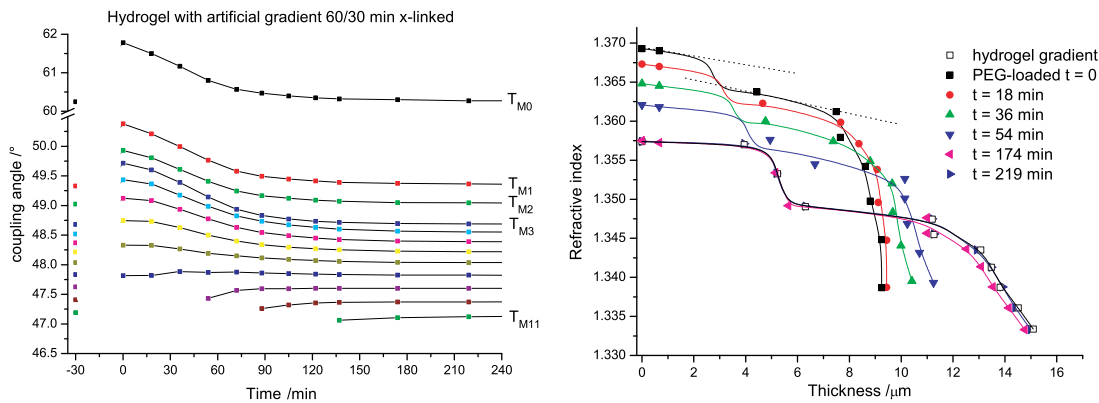


Fig. 6.18: Coupling angles of all T_M modes upon diffusion of PEG out of the hydrogel with the artificial gradient (60 min crosslinked in the lower layer, 30 min in the upper, see section 5.2) (left) and the corresponding refractive index gradients calculated with the help of the WKB-approximation (right). The dashed lines with $t=0$ indicate the presence of a step-like gradient from the comparison of the two slopes.

Derived from these angular scan measurements, the changes in the corresponding refractive indices detected by the T_{M1} -mode were plotted against the time. For the gradient gel in addition to the T_{M1} -mode, the T_{M4} -mode was plotted. Here, the T_{M1} -mode detects changes in the highly crosslinked layer close to the metal interface, whereas the T_{M4} -mode senses in the upper low crosslinked part

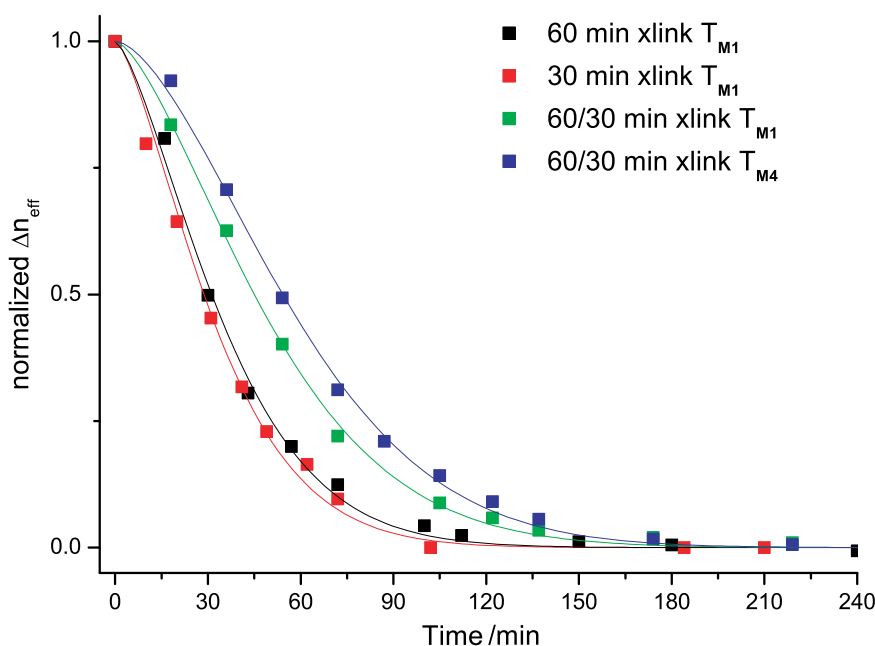


Fig. 6.19: Evolution of the normalized effective refractive indices of the systems described above – the 60 min crosslinked (black), the 30 min crosslinked (red) and the two layer system with the lower 60 min crosslinked layer (green) and the upper 30 min crosslinked layer (blue) – with time. The lines are to guide the eye.

of the film. This allows to compare the effects of diffusion in the highly and low crosslinked layers.

The normalized changes in the refractive indices of the corresponding films, while the PEG is diffusing out of them, are depicted in figure 6.19. These changes include all the effects on the hydrogels caused by the diffusing PEG. The decreasing concentration of PEG lowers the refractive index and at the same time the gel reswells which lowers the refractive index as well. Beside, the reswelling increases the mesh size and should hence increase the diffusion coefficient of the PEG. The diffusion process in the gel with the artificial gradient exhibits a delay between the two layers. This is caused by the PEG diffusing from the lower, highly crosslinked layer (green squares) into the upper, low crosslinked layer (blue squares).

With the described method, the process of diffusion of such large probes can be displayed as good as with waveguide mode tracking (kinetic mode) measurements. In addition, more information about the behavior of the whole gel are gained by the repeated angular scans, which enables for example the determination of mass distribution by effective medium theory. These scan revealed the partial collapsing of the gels upon loading. However, a model which takes all the described effects into account has to be developed. Therefore it was resigned to quantitatively assign parameters and to compare the different systems.

6.1.6 Conclusion and Outlook

Tracking probe diffusion by FCS was used to evaluate the mesh size of the grafted and crosslinked hydrogel. The assumption of a size dependent friction allows to infer from the probe diffusion in crosslinked gels to the mesh size in transient gels. First, PCS was used to obtain an evaluation of the mesh size of a transient gel based on its cooperative diffusion time. Then, by using FCS, tracer diffusion times in the same transient gels were compared to tracer diffusion times in crosslinked gels. Thus a scaling relation could be established for crosslinked gels by associating diffusion times to corresponding mesh sizes which were independently measured for transient gels. In this relation, different crosslinking densities correspond to different concentrations via volume fraction calculation. To refine the resolution of FCS, first steps were made towards a decrease of the focal volume. A dye-labeled gel was synthesized that allows for the excitation of the attached dyes via FRET from the diffusant dyes.

The diffusion of gold nanoparticles in transient and diluted gels was studied by PCS. In contrast to FCS, not the probes self-diffusion but the relative motion of the scatterers, the collective diffusion is detected. Gold nanoparticles can dominate the scattering of the gel in a good solvent and thus giving insight to tracer diffusion by PCS.

By employing WKB-assisted SPR/OWS access was gained to measuring the diffusion of nonfluorescent and weakly scattering probes inside the grafted and crosslinked hydrogel. Regarding the detection of biomolecules this approach is of higher practical relevance, as the labeling of biomolecules might disturb their functionality and free dyes can influence FCS measurements. Furthermore, for sensor applications, a labeling of the analyte is impracticable.

Beside this, WKB-assisted SPR/OWS allowed for a more detailed look on loading phenomena. The evaluation of the angular scans clearly showed a collapsing of the gels upon loading with PEG. Furthermore, they indicate, that the counterintuitive finding in section 5.1, that a higher crosslinked gel can take up more BSA than a lower crosslinked might have its origin in a concurrent collapse with the take up of the diffusant as described above. This behavior is neglected in a simple angular scan.

Predicting a size dependent mobility associated to the mesh size of the network can be useful for the utility of hydrogels as matrix for biosensor applications. The thermal motion of dispersed noninteracting probes depends on the structure and dynamics of the network host on microscopic length scales as well, which is investigated in section 6.3.

6.1.7 Experimental Part

Sample Preparation

For the FCS studies, PNIPAAm gels were prepared on round glass microscope cover slides (Menzel- Glaser, Germany). The gel adhesion was promoted by first treating them with 4-(3-chlorodimethylsilyl)propoxybenzophenone. The silane was chemisorbed on the glass surface at room temperature from a toluene solution (20 mL of a 0.025 molar solution) using triethylamine (4 mL) as catalyst and acid scavenger. The solution with the glass substrates was left to stand overnight. Then, the samples were cleaned by successively rinsing with dichloromethane, methanol, toluene, and again dichloromethane. After each rinsing step, the sample was blown dry with nitrogen. Hydrogel-polymer films of about 1 μm thickness were prepared by spincoating from a 10 w% ethanolic solutions onto the silanized microscope slides. Hydrogel films were investigated with different crosslinking densities prepared by irradiating the hydrogel-polymer films from 1.0 J cm^2 to 24.0 J cm^2 .

Dye-labeled Hydrogel

To covalently attach an Alexa 647 dye, a PNIPAAm sample was first activated with EDC/PFP and then labeled with Alexa 647 cadaverine. The activation was performed in DMF at room temperature for 3 h in the presence of triethylamine. Coupling of the Alexa 647 cadaverine to the activated polymer was achieved by stirring in DMF at 50°C for 20 h. In order to remove nonbound dye molecules, EDC and pentafluorophenol, the polymer solution was subjected to dialysis in DMF (MWCO of 14.000 g/mol) for 2 weeks.

Au-Nanoparticles

The Au-nanoparticles were prepared by Marcus Schmelzeisen according to Lennox *et al.*^[153] with the cationic ligands synthesized following a procedure of Whitesides *et al.*^[154] at the MPIP. The anionic and DMAP-coated particles were transferred to ethanol by centrifugation and redispersion, the cationic were kept in the ethanol water mixture.

TOA-Au-Nanoparticles

Upon adding an aqueous solution of hydrogen tetrachloroaurate (500 mg in 40 mL MilliQ) to a solution of tetraoctylammoniumbromide (TOA, 3.06 g) in

100 mL toluene, the aurate is transferred to the organic phase, coloring it deep orange. The gold nanoparticles are formed by reduction with sodium borohydride (525 mg in 30 mL MilliQ), turning the color to a dark red. The organic phase is extracted in sequence with 0.1 mol/L sulfuric acid, 0.1 mol/L sodium hydroxide and MilliQ. The Dispersion is diluted to 250 mL and subject to further synthesis described below.

DMAP-Au-nanoparticles

To prepare DMAP coated Au-nanoparticles, an aqueous solution of 4-(dimethylamino)pyridine (DMAP, 3.05 g in 250 mL MilliQ) is added to the toluene dispersion. The DMAP-Au-nanoparticles are transferred to the aqueous phase, giving a concentration of ~ 1 mg/mL.

Anionic Au-Nanoparticles

Ligand exchange to an anionic shell is performed by mixing a suspension of DMAP-Au-nanoparticles (20 mL, ~ 1 mg/mL in MilliQ) with deprotonated 11-mercaptopundecanoic acid (4.42 mg in 45 mL ethanol and 0.5 mL MilliQ, pH = 10) over night.

Cationic-Au-Nanoparticles

The exchange to a cationic shell is performed by stirring a suspension of DMAP-Au-nanoparticles (20 mL, ~ 1 mg/mL in MilliQ) with *N,N,N*-trimethyl(11-mercaptopundecyl)ammonium chloride (5.69 mg in 45 mL ethanol and 0.5 mL MilliQ, pH = 10) over night.

***N,N,N*-Trimethyl-10-undecenylammonium bromide** Undecenyl bromide (12.5 mL) is reacted with trimethylamine (10 g) in methanol at RT. After 2 d the volatiles were distilled off, the solid were taken up in DCM and precipitated in hexane. The yield was 11.85 g (78%) of a colorless solid.

$^1\text{H-NMR}$ (300 MHz, CD_3OD): δ (ppm) = 5.80 (m, 1H,C9), 4.94 (m, 2H, C10), 3.34 (m, 2H, C1), 3.14 (s, 9H, NMe_3), 2.04 (m, 2H, C8), 1.79 (m, 2H,C2), 1.37 (m, 12H,C3-7).

***N,N,N*-Trimethyl(11-mercaptopundecyl)ammonium chloride** To a solution of *N,N,N*-trimethyl-10-undecenylammonium bromide (2.92 g) in chloroform thioacetate (2.28 g) and AIBN (100 mg) were added and refluxed for 20 h. The

volatiles were distilled off and the remaining yellow solid was washed with ice cold diethylether. The dry solid was refluxed with 10 % hydrochloric acid for 1 h, dried and recrystallized from MilliQ with activated charcoal, giving 0.8 g (24%) of a colorless solid.

$^1\text{H-NMR}$ (300 MHz, D_2O): δ (ppm) = 3.29 (m, 2H, C1), 3.08 (s, 9H, NMe_3), 2.53 (t, 2H, C11, $^3J_{11;10} = 8.0$ Hz), 1.77 (m, 2H, C2), 1.59 (m, 2H, C10), 1.32 (m, 14H, C3-9).

6.2 Tracking-Probes with various Sizes and Charges

6.2.1 Introduction

The diffusion of various tracking-probes within the hydrogel or semidilute hydrogel-polymer solutions has been investigated in chapter 6.1. Their drawback, however, is their limitation towards the variation of their parameters in terms of charge and size. Suitable dyes are available only in a narrow window of parameters, nanoparticles can be tuned in size but bear multiple charges, and most common polymers are neither fluorescent nor do they scatter enough light for employment in PCS or FCS. Applying SPR/OWS to overcome these limitations, however does not allow for the investigation of diffusion phenomena on such short length and time scales and can not reach the accuracy of PCS and FCS. A dye-labeled polymer, as presented in chapter 6.3.2 allows for variations in size via the chain length, tuning the non charged interaction with the host via the polymer type, and for the adjustment of charge via functionalized end groups. However, a more defined polymer in terms of size distribution and chemistry has to be employed.

6.2.2 PEG-Dye

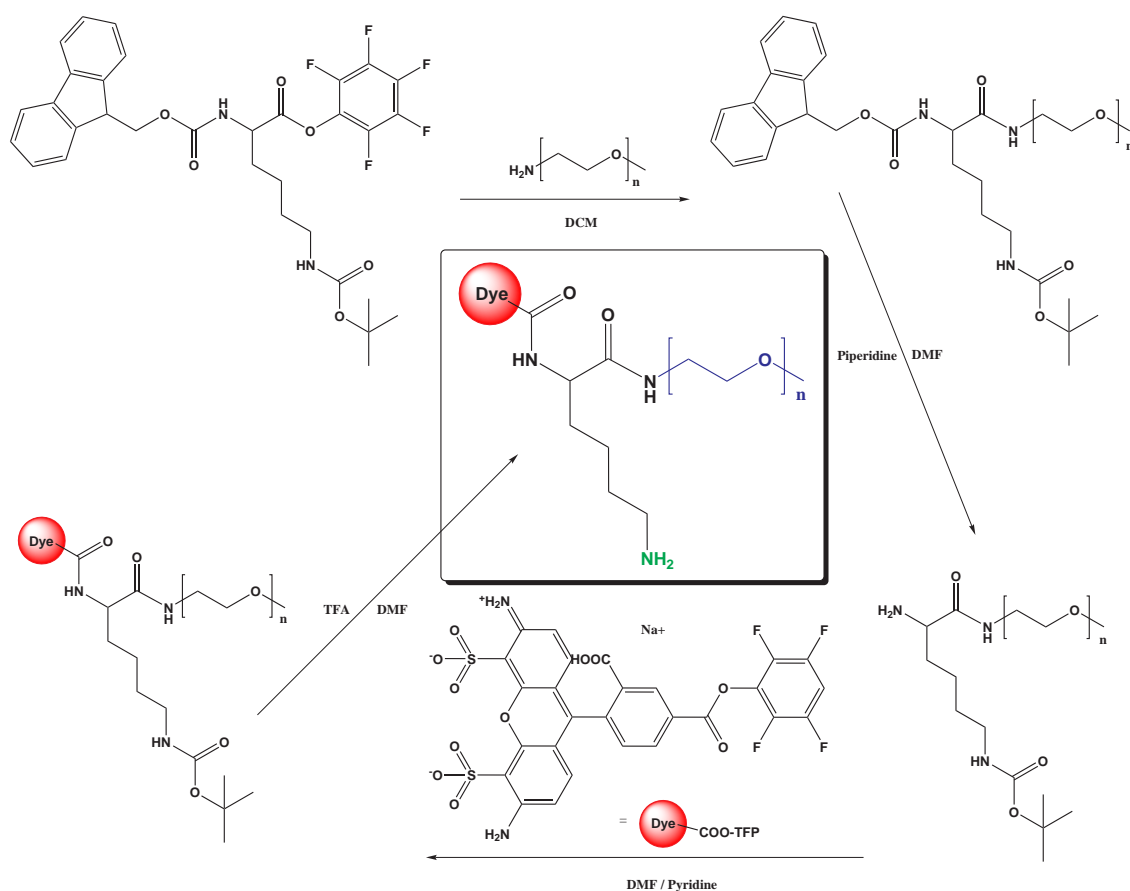


Fig. 6.20: Reaction sequence to synthesize a dye with attached PEG-chain and pH dependent charge carrier.

PEG was chosen as polymeric probe as it is non charged but soluble in water and ethanol. Furthermore, it is available with very narrow size distributions and can be endfunctionalized as well. Such PEGs of various chain lengths ($M_n = 750 \text{ g/mol}$, 10 kg/mol and 20 kg/mol) were attached to a lysine derivative as it can provide a linkage to a dye and a position for charge modification. The synthesis sequence of the tracking-probe depicted in figure 6.20 was planned based on active ester and protective group chemistry. Therefore, the lysine derivative employed was the commercial available pentafluorophenyl ester with Fmoc and Boc protected amines (Fmoc-Lys(Boc)-O-PFP).

In a first step the respective amino-PEG was bound to the activated lysine derivative giving its amide. Figure 6.21 shows the $^1\text{H-NMR}$ of the product and the structure in the inset. The $^1\text{H-NMR}$ shows the peaks corresponding to the attached PEG as well as its $\alpha\text{-CH}_2$ group around 3.45 ppm, shifted upon binding.

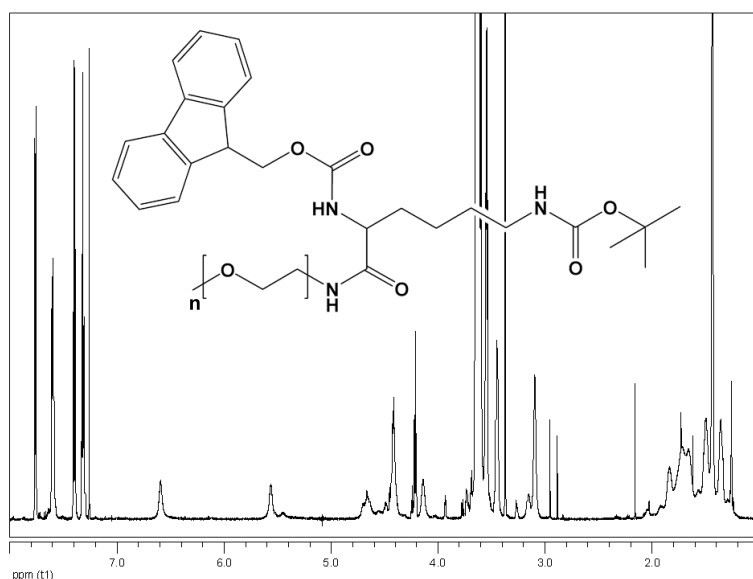


Fig. 6.21: $^1\text{H-NMR}$ in CDCl_3 of a 750 g/mol amino-PEG bound to the protected lysine derivative, as shown in the inset. The PEG peak is dominant at ~ 3.6 ppm and the protective groups are visible in the aromatic regime (FMOC) and at ~ 1.4 ppm (Boc).

The FMOC and the Boc group were unaffected, since the aromatic and the *tert.* butanol peaks (~ 1.4 ppm) respectively remained.

To provide access of an amine to the reactive ester dye, FMOC was cleaved by piperidine. The vanishing of the peaks in $^1\text{H-NMR}$ corresponding to FMOC (see fig. 6.22) as well as the distinct reactions with hydrazine (Ruhemann's purple, Kaiser test)^[155,156] proved the presence of the free amine.

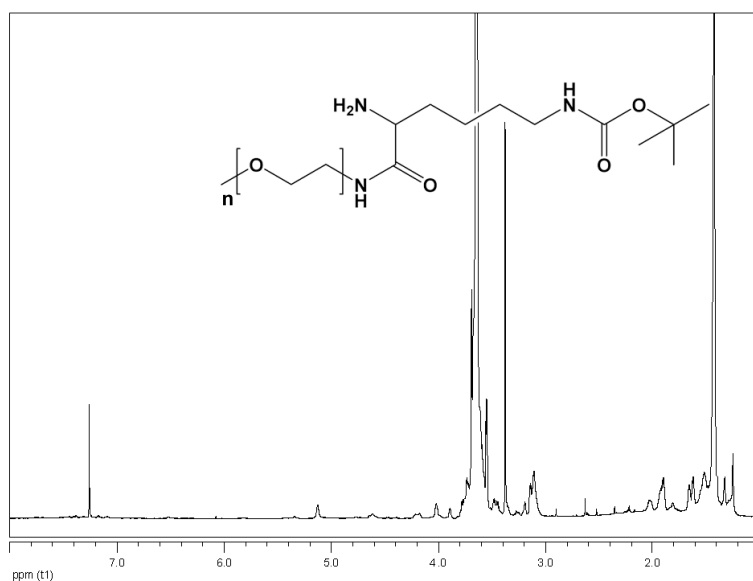


Fig. 6.22: $^1\text{H-NMR}$ in CDCl_3 of a 750 g/mol amino-PEG attached to the protected lysine derivative with one deprotected amine, as shown in the inset. The Boc-group ~ 1.4 ppm remained.

Two active ester derivatives of Alexa 488 were tested for the binding to the pegylated lysine, tetrafluorophenol (TFP) and dichlorophenol sulfonate (DCPS). Both, however failed or had a yield below 5 %. In FCS, used to investigate the product, almost only free Alexa 488 was present.

In the last step, the Boc protected amine of the lysine derivative was deprotected by trifluoroacetic acid. The reaction was considered successful, when the *tert.* butyl group in the $^1\text{H-NMR}$ disappeared (see fig. 6.23).

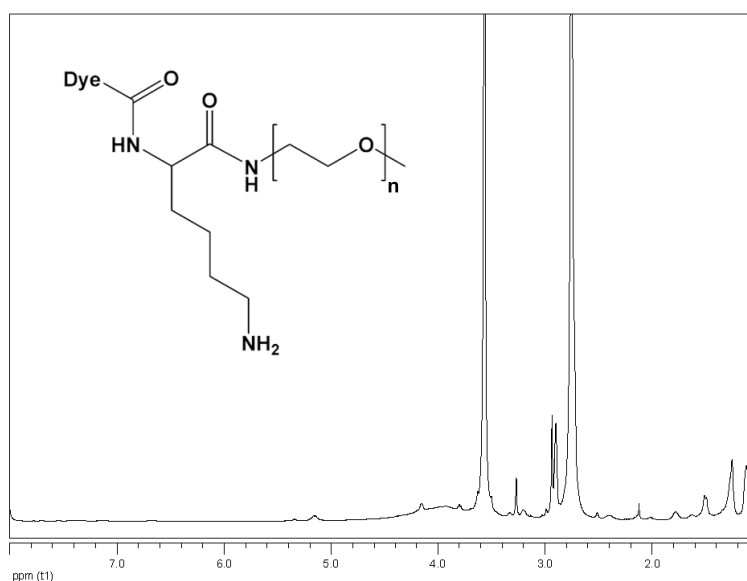


Fig. 6.23: $^1\text{H-NMR}$ in CDCl_3 of a 750 g/mol amino-PEG attached to lysine. The Boc-group around 1.4 ppm disappeared.

6.2.3 Conclusion and Outlook

After all, it was not possible to address the previously Fmoc-protected amine with the active ester dye. Ongoing experiments suggest, that the proximity to the amide reduces the nucleophilicity of this amine, hindering the reaction. As consequence, the synthesis plan was reorganized to attach the dye to the former Boc-protected amine. The results are expected shortly.

6.2.4 Experimental Part

The PEG with terminal amine group ($PDI \leq 1.1$) were purchased from Rapp Polymere GmbH, Germany, the lysine derivative from BACHEM, Switzerland.

PEG-Dye Synthesis

For the NMR evaluation see paragraph PEG₇₅₀-Dye, as for the two other molecular weights, the broad PEG-peak conceals important peaks like the discussed α -CH₂-peak of the PEG.

PEG_{20K}-Dye

FMOC-Lys(Boc)-N-PEG To PEG-amine (1.05 g, 20 kg/mol, 0.05 mmol) in DCM FMOC-Lys(Boc)-O-PFP (232 mg, 0.37 mmol) was added. The progress was frequently checked for the reaction of the PEG-amine with ninhydrin to disappear. After 6 d stirring at 50°C, the DCM was replaced with THF and the solution was precipitated in heptane, yielding 970 mg (92%) product.

H₂N-Lys(Boc)-N-PEG After reacting possible leftover active esters with ethanolamine (1 mL), the FMOC protection group was cleaved by adding piperidine (5 ml $\hat{=}$ 25 vol%) to FMOC-Lys(Boc)-N-PEG (500 mg) in dry DMF. Having stirred the solution for 3 d at 50°C, volatiles were removed in vacuum followed by precipitating from THF in cyclohexane. The peaks in ¹H-NMR corresponding to the FMOC-group had disappeared and the yield was 270 mg (54%).

Dye-N-Lys(Boc)-N-PEG H₂N-Lys(Boc)-N-PEG (15 mg) in dry DMF, dry pyridine (1 mL) and Alexa 488 TFP (0.5 mg) were unified and stirred for 5 d at 30°C. After drying in vacuum, the attachment of the dye was checked with FCS, which shows only free Alexa 488.

Dye-N-Lys(NH₂)-N-PEG Dye-N-Lys(Boc)-N-PEG was stirred in a mixture of TFA and dry DMF (TFA 1 : DMF 2) for 13 d at RT. The disappearance of the *tert.* butyl group in the ¹H-NMR proved the success.

PEG_{10K}-dye

FMOC-Lys(Boc)-N-PEG To PEG-amine (1 g, 10 kg/mol, 0.1 mmol) in DCM FMOC-Lys(Boc)-O-PFP (1.1 g, 1.75 mmol) was added. The progress was frequently checked for the reaction of the PEG-amine with ninhydrin to disappear. After 7 d stirring at 35°C, the DCM was replaced with THF and the solution was precipitated in heptane, yielding 1100 mg (97%) product.

H₂N-Lys(Boc)-N-PEG After reacting possible leftover active esters with ethanolamine (1 mL), the Fmoc protection group was cleaved by adding piperidine (5 mL, \cong 25 vol%) to Fmoc-Lys(Boc)-N-PEG (500 mg) in dry DMF. Having stirred the solution for 7 d at 35°C, volatiles were removed in vacuum followed by precipitating from THF in cyclohexane. The peaks in ¹H-NMR corresponding to the Fmoc-group had disappeared and the yield was 320 mg (65%).

Dye-N-Lys(Boc)-N-PEG H₂N-Lys(Boc)-N-PEG (10 mg) in dry DMF, dry pyridine (1 mL) and Alexa 488 TFP (1 mg) were unified and stirred for 9 d at 35°C. After drying in vacuum, the attachment of the dye was checked with FCS, which shows almost no attached Alexa 488.

Dye-N-Lys(Boc)-N-PEG H₂N-Lys(Boc)-N-PEG (10 mg) in dry DMF, dry pyridine (1 mL) and Alexa 488 DCPS (1 mg) were unified and stirred for 9 d at 35°C. After drying in vacuum, the attachment of the dye was checked with FCS, which shows only free Alexa 488.

PEG₇₅₀-Dye

Fmoc-Lys(Boc)-N-PEG To PEG-amine (1 g, 750 g/mol, 1.33 mmol) in DCM Fmoc-Lys(Boc)-O-PFP (1.1 g, 1.75 mmol) was added. The progress was frequently checked for the reaction of the PEG-amine with ninhydrin to disappear. After 2 d stirring at RT, the volatiles were distilled off and the product was obtained by freeze desalination in acetone with a yield of 520 mg (25%).

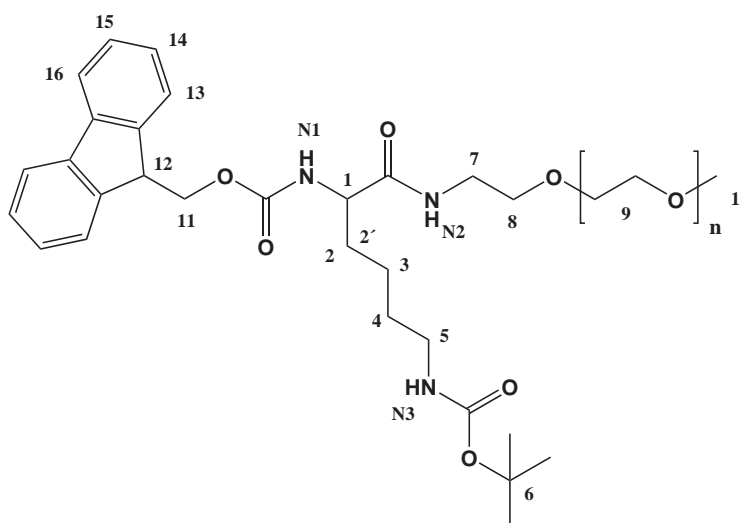


Fig. 6.24: Fmoc-Lys(Boc)-N-PEG, the ¹H-NMR is depicted in figure 6.21.

$^1\text{H-NMR}$ (700 MHz, CDCl_3): δ (ppm) = 7.76 (d, 2H, H_{16} , $^3\text{J}_{16;15} = 7.5$), 7.60 (d, 2H, H_{13} , $^3\text{J}_{13;14} = 7.3$ Hz), 7.40 (t, 2H, H_{15} , $^3\text{J}_{15;16,14} = 7.3$ Hz), 7.31 (t, 2H, H_{14} , $^3\text{J}_{14;15,13} = 7.4$ Hz), 6.59 (bs, 1H, N_2), 5.56 (bs, 1H, N_1), 4.66 (bs, 1H, N_3), 4.42 (d, 1H, H_{11} , $^3\text{J}_{11;12} = 6.9$), 4.21 (t, 1H, H_{12} , $^3\text{J}_{12;11} = 6.9$ Hz), 4.14 (bs, 1H, H_1), 3.67 - 3.58 (m, 76H, H_9), 3.54 (m, 4H, $\text{H}_9 + \text{H}_8$), 3.45 (m, 2H, H_7), 3.38 (s, 3H, H_{10}), 3.10 (b, 2H, H_5), 1.84 (bs, 1H, H_2), 1.66 (b, 1H, H_2), 1.50 (b, 2H, H_4), 1.44 (s, 9H, H_6), 1.37 (b, 2H, H_3).

$\text{H}_2\text{N-Lys(Boc)-N-PEG}$ After reacting possible leftover active esters with ethan-
olamine (200 μL), the Fmoc protection group was cleaved by adding piperidine
(1.3 ml, $\hat{=}$ 25 vol%) to Fmoc-Lys(Boc)-N-PEG (200 mg) in dry acetone. Having
stirred the solution for 24 h at RT, volatiles were removed in vacuum followed by
precipitating from DCM in cyclohexane. The peaks in $^1\text{H-NMR}$ corresponding to
the Fmoc-group had disappeared and the yield was 120 mg (72%).

6.3 Gel Dynamics

6.3.1 Introduction

To characterize the diffusion through a hydrogel network, the dynamic behavior of fluorescent probes has been studied by FCS. Since the thermal motion of such a probe depends on the structure and dynamics of the host network as well, this chapter focuses on the development of an useful method and its exploitation to investigate the dynamics of thin layers of anchored crosslinked hydrogel. These were basically not investigated so far, due to the lack of experimental techniques to study the molecular motions in thin films. Dynamic light scattering,^[72,73] X-ray photon correlation^[157] and fluorescence spectroscopy^[74,75] have been applied frequently to study polymer dynamics in submicron thick films. First, the dynamics of dye-labeled PNIPAAm were investigated by FCS in section 6.3.2. The label-free exploration of the gel dynamics was performed by micro photon correlation spectroscopy (μ PCS), as presented in section 6.3.3.

6.3.2 FCS of Dye-labeled Hydrogel

The investigation of the dye-labeled PNIPAAm-based terpolymer (PNIPAAm for simplification) by FCS was a cooperation with Maria Gianneli who performed the measurements, Patrick Beines, Kaloian Koynov, Georg Fytas and Wolfgang Knoll. More details can be found in the published paper.^[59]

When studying the dynamic properties of a polymeric system, the self-diffusion coefficient of polymers is prevalently subject to research. So far, investigations were performed by pulse-field gradient NMR,^[158–160] optical grating techniques,^[161–164] and, under some specific optical contrast conditions, photon correlation spectroscopy.^[135,145] FCS^[76,136,137] has been applied to synthetic polymers only recently,^[138–144] therefore only limited information are available. In the case of labeled PNIPAAm, the molecular mass of the tracer $M_t \approx M_m$, the molecular mass of the matrix. Hence, D is close to the self-diffusion and is expected to sense the global dynamics of the PNIPAAm nondilute solutions as reflected in the solution viscosity $\eta(c)$.

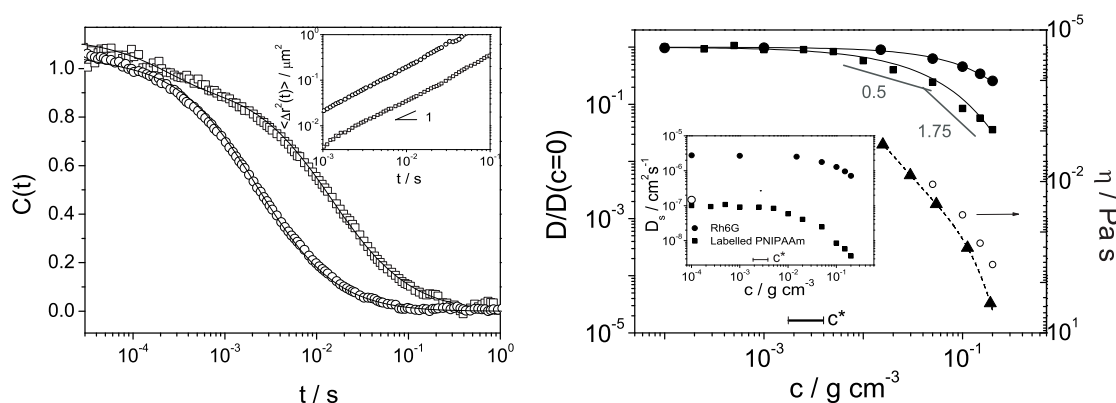


Fig. 6.25: Left: Normalized fluorescence intensity correlation function $C(t)$ for labeled PNIPAAm in two ethanolic PNIPAAm solutions ($c = 0.02$ g/mL (circles) and $c = 0.15$ g/mL (squares)) in the semidilute regime. The mean square displacement of the single fluorescent PNIPAAm chain indicates Brownian diffusion (slope one in double log plot) as shown in the inset.

Right: Normalized self-diffusion coefficient of Rh6G (solid circle) and labeled PNIPAAm (solid squares) below and above the overlap concentration c^* . The solid lines represent a two parameter stretched exponential fit $\exp(-\beta c^*)$. For comparison, the solution viscosity (open circle) and the cluster diffusion coefficient (solid triangles) from section 6.1.2.1 are shown as a function of concentration. The dashed line is to guide the eye. The corresponding data from PCS (section 6.1.2.1) are shown in the inset: the experimental self-diffusion coefficient of the two dyes (solid symbols) and the translational diffusion coefficient of PNIPAAm (single open circle).

The diffusion of the labeled PNIPAAm for two concentrations in the nondilute regime is displayed as normalized fluorescent intensity autocorrelation function

$C(t)$ in figure 6.25 left. These functions are clearly much slower than the corresponding decay functions for the small probe (Rh6G) in figure 6.2 (section 6.1.2.1) at similar polymer matrix concentrations. The initial decay of $C(t)$ (between 0.1 and 0.4 ms) might be due to the presence of a small amount of free dye (see figure 6.2). Excluding this initial decay, the tracer mean square displacement (inset to fig. 6.25 left) conforms to a random Brownian diffusive motion even at the highest concentration. This result is in agreement with forced Rayleigh scattering experiments in polystyrene nondilute solutions.^[163] The inset to figure 6.25 right shows the diffusion coefficients D of the small Rh6G and the larger labeled PNIPAAm measured by FCS along with the translational diffusion (open circle) of PNIPAAm measured by PCS. The latter is about 10% faster because of its slightly lower R_h compared with the labeled chain. The good agreement between FCS and PCS in dilute solutions is to be expected for correct experiments.^[144] The vastly different Einstein diffusion coefficient D_0 of the small and large probe in the dilute regime reflects the difference in their sizes. For a clear presentation of the concentration dependence, figure 6.25 right displays the normalized diffusion coefficients relative to the corresponding (D_0) values at the lowest PNIPAAm concentration. The large probe diffusion clearly exhibits stronger concentration dependence than the small probe^[147,161,163] and resembles that of the solution viscosity (open circles) shown in figure 6.25 for comparison. The concentration dependence of $D(c)$ for the large probe in a matrix with similar size should resemble the concentration dependence of the self-diffusion coefficient. Hence, the scaling predictions -0.5 and -1.75 respectively for unentangled and entangled semidilute solutions in a good solvent are drawn for comparison. The solution viscosity (open circles) should exhibit stronger concentration dependence than the self-diffusion with corresponding scaling predictions 2 and 3.9 in the two semidilute regimes.^[165] Experimentally, the specific viscosity, $\eta(c) - \eta_s \sim c^{3.4}$, in the highest concentration region is closer to the scaling exponent for entangled polymers in good solvents. The conformity to the scaling predictions up to the highest concentration suggests that the local friction does not play a significant role up to 20 vol%; that means, the solution is still semidilute in spite of the high T_g ($\sim 140^\circ\text{C}$) of PNIPAAm.

Comparing the different diffusion data in figure 6.25 right, obtained from the two complementary experimental techniques clearly disputes the assignment of the slow diffusion process in the PCS experiment (figure 6.3, section 6.1.2.1) to the self-diffusion.^[146] Instead, this process relates to the diffusion of a cluster of PNIPAAm chains, which closely follow the macroscopic solution viscosity. This as-

signment is further supported by the observation of the slow process in the semidilute solutions $c > c^*$. As consequence, the self-diffusion in semidilute homopolymers can be safely measured only by FCS and not PCS, but both techniques can be complementarily employed. In the case of this hydrogel, FCS measures both local dynamics associated with length scales in the order of the mesh size ζ and global dynamics over the size of the used probe in the semidilute entangled regime well above c^* . On the other hand PCS can safely measure the mesh size $\zeta(c)$ and the concentration dependence of $\eta(c)$ via the slow cluster mode. In the very dilute regime ($c \ll c^*$), both techniques measure the chain translational diffusion with FCS being applicable even at extremely dilute conditions.

However, it was not possible to investigate the dynamics of the crosslinked hydrogel by FCS. The dye-labeled and crosslinked polymer chains did not create a correlation function, as their translational movement does not exceed the dimensions of the focal volume within the time window of the experiment.

6.3.3 μ PCS of the Hydrogel

The investigation of the dynamics of the PNIPAAm-based terpolymer by μ PCS was a cooperation with Maria Gianneli and Benoit Loppinet who performed the measurements, Ulrich Jonas, Georg Fytas and Wolfgang Knoll. More details can be found in the published paper.^[60]

So far, μ PCS has been used in films of strong scattering media like liquid crystals near the nematic transition.^[166] Recently a scanning microscope light scattering set-up^[73] with a beam diameter of only a few μm at the scattering volume was used to investigate the dynamics of polyacrylamide gels in the bulk. The significant interest in spatial and temporal resolution renders the micro scattering techniques very important.

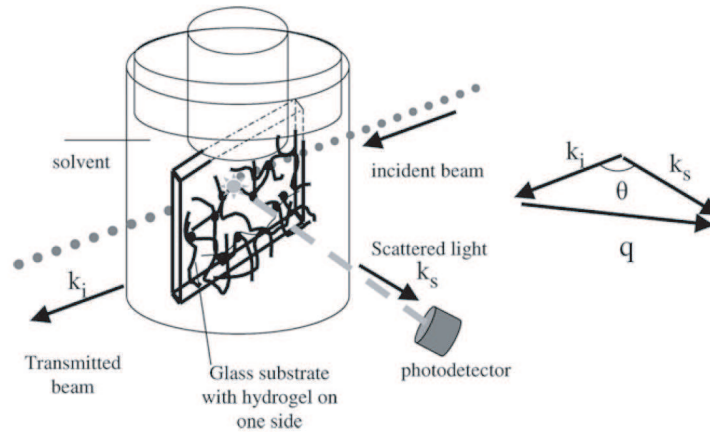


Fig. 6.26: Experimental geometry of the sample cell used for the light scattering measurements along with the scattering wavevector $q = k_s - k_i$ and the wavevector of the incident (k_i) and the scattered light (k_s).

Hydrogel layers with three different crosslinking densities were prepared, their dynamics at thermal equilibrium swollen in ethanol are manifested in the relaxation function

$$C(q, t) = \sqrt{[G(q, t) - at]/f^*} \quad (6.3)$$

Equation 6.3:

$f^* < 1$ - an instrumental factor; at - the base line of $G(q, t)$ at long times ($\sim 1s$).

$G(q, t)$ is recorded under heterodyne conditions by means of the photon correlation spectroscopy configuration shown in figure 6.26. The correlation function $G(q, t)$ saturates at short times ($< \mu\text{s}$) to $b = 2\langle I \rangle_E / I_c$ where I_c denotes the

elastic contribution from the laser beam and the frozen fluctuations (static heterogeneities) and $\langle I \rangle_E$ is the ensemble average scattering intensity from the gel layer.^[167,168]

The relaxation functions of the concentration fluctuations in figure 6.27 exhibits two distinct decays. Interestingly enough the slow process relaxes within the experimental time window ($t < 100$ s). This relaxation pattern is ergodic, i.e. insensitive to variations of the probed spots in the films. In addition, there exist much slower fluctuations at decay times beyond 10 s. Since they do not affect the characteristics of the two faster relaxation processes, they were not included in $f(q, t)$.

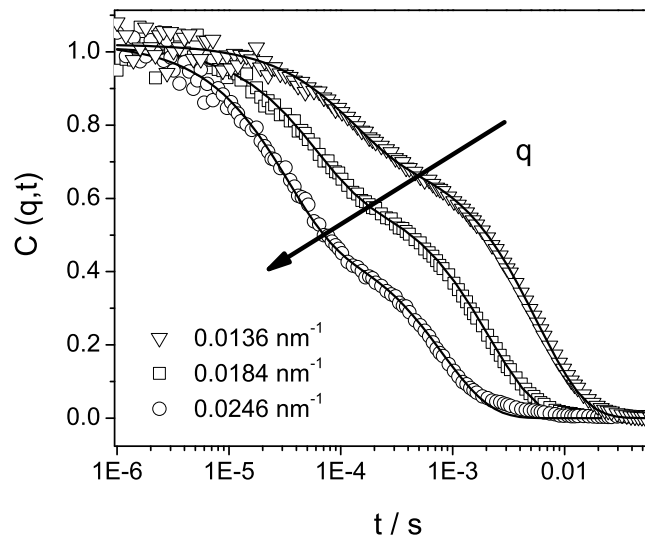


Fig. 6.27: Normalized autocorrelation function $C(q, t)$ at different scattering wavevectors q of a 1.6 J cm^{-2} crosslinked gel swollen in ethanol.

The existence of two separate processes was observed for all gel films with different crosslinking densities. The temporal separation of the two processes allowed fitting $f(q, t)$ with a double exponential decay function:

$$f(q, t) = a \exp(-\Gamma_f t) + (1 - a) \exp(-\Gamma_s t) + a' \quad (6.4)$$

Equation 6.4:

a - the amplitude; Γ_f - the relaxation rate of the fast process; Γ_s - the relaxation rate of the slow process; a' - the base line of $G(q, t)$ at long times (~ 1 s).

This simple expression represents well the experimental $C(q, t)$ as indicated by the solid lines in figure 6.27. Both relaxation modes are q -dependent and show

pure isotropic diffusive ($\Gamma \sim q^2$) behavior as indicated by slope 2 in the double logarithmic plot in figure 6.28 for the three films with different crosslinking densities. The scattered intensity in $f(q, t)$ is approximately given by $\langle I(q) \rangle = I_0 b$ where I_0 is the averaged intensity over the measurement time. While the dynamic intensity $I_f = a \langle I(q) \rangle$ associated with the fast process is q -independent, the dynamic intensity $I_s(q) = (1 - a) \langle I(q) \rangle$ associated with the slow mode was found to increase with decreasing q . The former suggests a small correlation length, which was found for the concentration fluctuations in semidilute polymer solutions that exemplify physical networks as well (see section 6.1.2.1). Hence, the fast process was assigned to the cooperative diffusion with $D_{coop.} = \Gamma_f(q)/q^2$, driven by the osmotic pressure of the system. The strong q -dependence of $I_s(q)$ of the slow diffusive process implies long correlation lengths for these slow concentration fluctuations. Typical, slow processes in 3D gels are reported to relax outside the experimental window and therefore exhibit non-ergodic behavior.^[77,151,167,168]

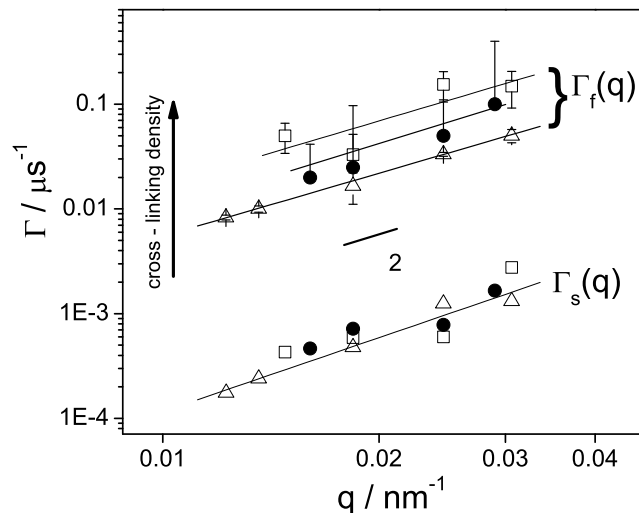


Fig. 6.28: Relaxation rates Γ for the two diffusive (slope 2) processes (fig. 6.27) versus the scattering vector q . The fast Γ_f represent the decay rates of the collective concentration fluctuations. Comparing the crosslinking doses 1.6 (open triangle), 6.3 (solid circles) and 12.6 J cm^{-2} (open squares) reveal the crosslinking density dependence of Γ_f and the independence of the slow rate Γ_s .

6.3.3.1 Fast Mode Relaxation

The diffusion coefficient D_{coop} (the relaxation rate Γ_f respectively) of the fast cooperative mode increases with crosslinking density as figure 6.28 reveals. An

increase of the crosslinking density can be compared with an increase of concentration in semidilute polymer solutions. There the increase of D_{coop} with polymer concentration (c) is due to the concurrent decrease of the mesh size $\xi(c)$.^[165] Figure 6.29 displays the increase of D_{coop} of the crosslinked gel films swollen in ethanol with the effective concentration, i.e. effective volume fractions ϕ of 0.092, 0.145 and 0.169 correspond to a crosslinking dose of 1.6, 6.3 and 12.6 J cm⁻² respectively (black circles). For comparison, the concentration dependence of the cooperative diffusion in semidilute PNIPAAm solutions in ethanol is depicted as well (black squares).^[59] This reveals a much stronger increase of D_{coop} with the effective concentration in the chemically crosslinked gels than in the physical network of the semidilute solutions. Finding a clear distinction between the physical network and the chemically crosslinked network layer anchored on the substrate indicates structural differences between the two types of network.

At low volume fractions below 0.1, D_{coop} in the anchored gel converges to that of the semidilute polymer solutions. Even lower volume fractions for the gel layers are experimentally not accessible as the crosslinking density would become lower than one per chain.

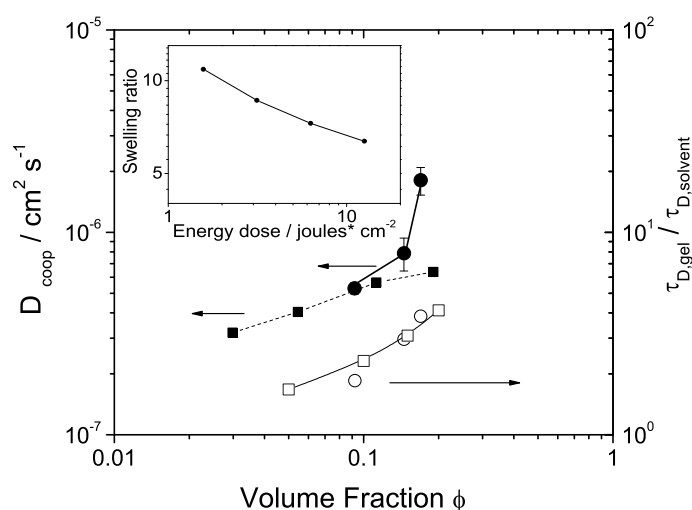


Fig. 6.29: Cooperative diffusion coefficient D_{coop} , plotted as a function of the effective volume fraction ϕ for PNIPAAm gels. The black circles correspond to gel of the three crosslinking densities swollen in ethanol. The black squares are the D_{coop} of semidilute ethanolic solutions of PNIPAAm for different concentrations, taken from ^[59]. The normalized (to the neat solvent) dye diffusion time $\tau_{D,gel} / \tau_{D,solvent}$ is shown as a function of the PNIPAAm concentration in the crosslinked films (open circles) and in semidilute PNIPAAm solutions (open squares). The swelling ratio of the gel films in ethanol as a function of the irradiation dose is shown in the inset. All lines are to guide the eye.

To investigate the local dynamics, figure 6.29 shows the diffusion time τ_D of Rh6 G (with $R_h = 0.8$ nm) measured by fluorescence correlation spectroscopy as a

function of volume in both systems. Within experimental error, τ_D in the gel layers (open circles) compares very well with the diffusion of the same dye in physical PNIPAAm networks (open squares)(see section 6.1.2).^[59] Since the diffusion time $\tau_D(\phi)$ of small dyes ($R_h < \xi$) depends only on the polymer concentration and not on the polymer molar mass,^[59] this finding suggests that the local dynamics are virtually the same in both systems and further supports the estimation of the volume fraction in the gel layers under the condition of uniaxial swelling.

Thus FCS and DLS of gel layers yield complementary dynamic and structural information. FCS measures the local friction but since $D_{coop}(c)$ of transient and permanent networks are, in general, different (see fig. 6.29), the effective mesh size ξ of gels can only be reliably obtained from the DLS experiment and not via the scaling relationships from FCS. For the gel layers of figure 6.29, ξ decreases from 3.4 nm for the shortest to 1 nm for the longest crosslinking time. These numbers are rather low compared to mesh sizes for transient networks and lower than the values determined for gel layers by FCS (see section 6.1.2), supporting the conclusions drawn on the structural differences between the two systems.

6.3.3.2 Slow Mode Relaxation

The slow diffusive process in the present anchored crosslinked gel layers (fig. 6.27 and 6.28) exhibits a diffusion coefficient of $D_s = \Gamma_s(q)/q^2 (\sim 1.5 \times 10^{-8} \text{ cm}^2 \text{ s}^{-1})$ and differs significantly from the slow dynamics in polymer systems reported so far. First it is ‘faster’ and ergodic in contrast to the very slow, non-ergodic process in a 3D gel, as seen in the well-resolved baseline of the functions of figure 6.27.^[77,151,167,168] Second, D_s seems to be virtually insensitive to the variation of the crosslinking density, i.e. volume fraction (fig. 6.28), contrary to the slow mode observed in the corresponding (non-crosslinked) semidilute solutions (see section 6.1.2.1).^[59] There, D_s was found to exhibit a strong decrease with increasing concentration and was attributed to the self-diffusion of polymer clusters.^[59,169] For crosslinked anchored gel layers, however, an analog description is hardly conceivable.

The origin of the slow mode in semidilute homopolymer solution is still discussed controversially.^[169] For chemically crosslinked gels, only one report^[168] was found, where the slow mode decays within the experimental time window. The slow mode in the grafted crosslinked gels features a large correlation length (in the sub-micrometer range) that can be assigned to long wavelength concentra-

tion fluctuations. Hence, this slow ergodic process might sense the connectivity of the network with the elasticity of the network probably acting as a restoring force. Its relation to the fast process has to be investigated and so far, its origin remains elusive.

6.3.4 Conclusion and Outlook

The translational motion of the dye-labeled PNIPAAm acting as large macromolecular tracer in a transient PNIPAAm network (i.e. semidilute solution) observed in FCS exhibited brownian diffusion independent of the concentration. The strong concentration dependence of the normalized diffusion coefficient is in line with the enhanced friction in semidilute entangled polymer solutions. These findings on self-diffusion show the complementarity with those obtained by PCS in section 6.1.2.1. Applying FCS to explore the self-diffusion of permanent PNIPAAm networks, however, failed. The motion of the attached dyes did not exceed the dimensions of the focal volume within the time window of the experiment. Therefore a new light scattering technique probing the crosslinked and grafted gel was employed. The fast cooperative diffusion was assigned to the motion associated with the effective mesh size of the network, analog to the case of the physical network of uncrosslinked PNIPAAm chains in section 6.1.2. In the crosslinked network, the cooperative diffusion increases faster with increasing volume fraction in the swollen gel layers than in the uncrosslinked PNIPAAm semidilute solutions, given uniaxial swelling. Hence, for a correct characterization of the effective mesh size the measurements need to be performed in the anchored crosslinked layers. The volume fractions calculated assuming uniaxial swelling were verified by the comparable tracer diffusion times observed in both systems via FCS.

Interestingly enough, the tethered crosslinked gel layers reveal a second, slow diffusive process, which is fully relaxed in the measurable time window. It was allocated to the relaxation of the concentration fluctuations, which may be connected to the mechanical properties of the gel. In contrast to the physical network of the semidilute terpolymer solution (see section 6.1.2.1), this process is virtually insensitive to the concentration, i.e. crosslinking density. Its unusual short relaxation rate might relate to dynamic heterogeneities, but its nature is still unknown.

6.3.5 Experimental Part

Sample Preparation

For the μ PCS studies microscope glass slides were functionalized with BP-silane and subsequently spincoated with a 10 w% ethanolic hydrogel-polymer solution. The $\sim 1 \mu\text{m}$ thick films were crosslinked for 15 min, 60 min and 120 min with a resulting irradiation dose of 1.6, 6.3 and 12.6 J cm^{-2} .

Dye-labeled Hydrogel

To covalently attach a tetramethylrhodamine dye, a PNIPAAm sample was first activated with trifluoroacetyl-*N*-succinimidyl ester and then labeled with tetramethylrhodamine cadaverine. The activation was performed in dichloromethane at room temperature for 3 h in the presence of triethylamine. Purification was achieved by precipitation in diethylether twice. Addition of the tetramethylrhodamine cadaverine to the activated polymer was achieved by stirring in ethanol at 50°C for 20 h. In order to remove unbound dye molecules, the polymer solution was dialyzed in ethanol (MWCO of 3500 g/mol for the utilized tube) for 2 weeks.

7 Application

7.1 Biosensor Matrix

7.1.1 Introduction

Hydrogels can be modified with proteins and other biomolecules to provide specific functionality for controlled drug release,^[170] defined interactions with cells,^[171] or the capture of target analyte molecules.^[28,172] Hence, employing the network of a hydrogel is a promising approach as matrix for biosensing. In addition, thermal responsive gels can be used for the design of advanced biosensor binding matrices. They can swell in an aqueous sample (e.g. blood sample) and capture a target analyte in the sample by a specific motive, immobilized at the hydrogel-polymer backbone. Upon an external stimulus, the gel collapse (e.g. by a temperature increase^[99]) can be triggered, expelling the liquid and unbound species from the hydrogel matrix. At the same time the specifically bound analyte would be concentrated at the sensor-substrate interface and therefore allow for its effective detection by SPR/OWS as introduced in section 1.2.

Thin films of the PNIPAAm-based hydrogel presented in this thesis were investigated by various optical methods including surface plasmon resonance (SPR) and optical waveguide mode spectroscopy (OWS).^[58,99] These techniques were applied to study the structural and swelling characteristics.

In this section, SPR/OWS is employed for the quantitative time-resolved characterization of mass changes and the swelling behavior of protein-functionalized hydrogel films. This allows for the detection of specific and unspecific adsorption of proteins inside the gel. This project was a cooperation with Alena Aulasevich who performed the SPR/OWS measurement, Jakub Dostálek, Ulrich Jonas, Bernhard Menges and Wolfgang Knoll and is already published.^[61]

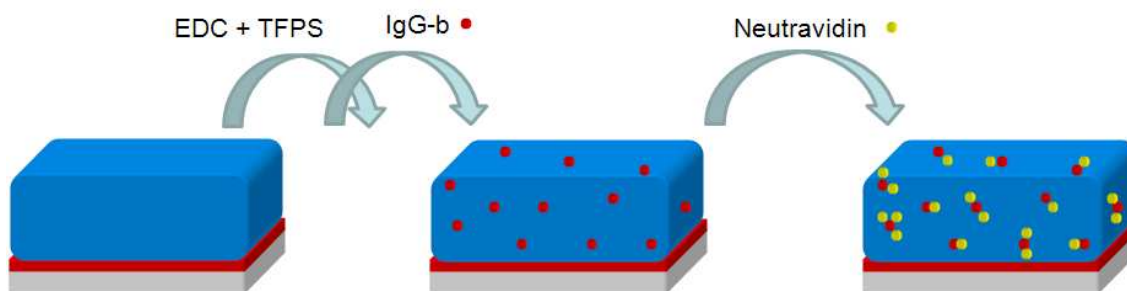


Fig. 7.1: Schematic illustration of the hydrogel being prepared and used as sensor matrix for the monitoring of the affinity binding of NA to biotinylated IgG.

The sensor matrix was functionalized by coupling immunoglobulin G (IgG) *in situ* covalently to the hydrogel by using active ester chemistry. Compared to other methods,^[28,173] this approach enables the covalent coupling of IgG molecules under mild conditions. As antifouling is an important property of a sensor matrix, the interaction of the protein functionalized hydrogel network with blood plasma was investigated. The potential application of the gel as a sensor matrix was demonstrated monitoring the kinetics of the affinity binding of neutraavidin (NA) molecules to the immobilized biotinylated IgG (IgG-b)(see fig. 7.1). SPR and OWS were applied simultaneously to detect the changes in refractive index and thickness. The optical characteristics of the setup are described in figure 7.2.

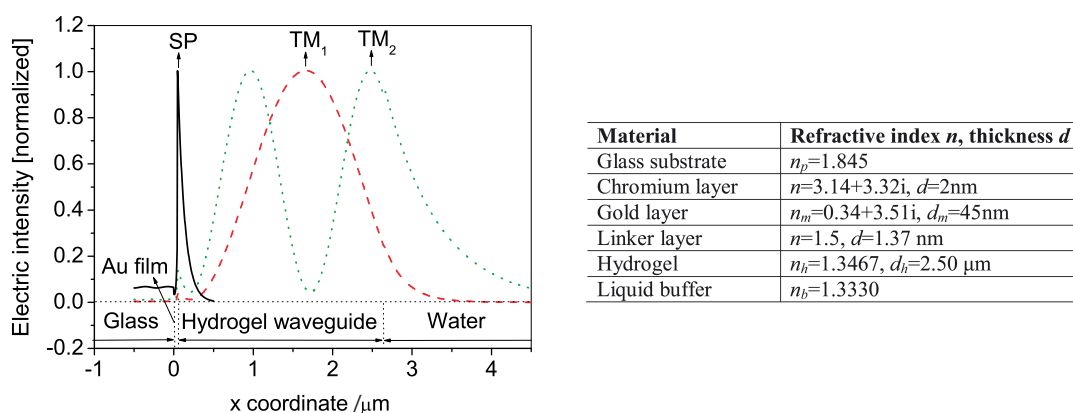


Fig. 7.2: Left: Simulation of the profile of the electric field intensity of the surface plasmon and the guided waves. Right: Parameters for the simulation shown on the left.

7.1.2 Immobilization of BSA

To identify the most promising method for the functionalization with biotinylated IgG, several of the active esters and activation methods, introduced in section 3.4, were tested for the immobilization of BSA within the hydrogel. The hydrophilic sodium tetrafluoropenol sulfonate (TFPS) and acetonoxime (AO) and the hydrophobic *N*-hydroxysuccinimide (NHS) and pentafluorophenol (PFP) were tested partly *in situ* and *ex situ*. For the *in situ* activation EDC and the respective alcohol (e.g. ECD-NHS) were reacted in aqueous media in the flow cell. For the *ex situ* functionalization the sensor chip was exposed to the trifluoroacetate esters (e.g. TFA-PFP) in dichloromethane in a vial. The results are summarized in Table 7.1. It reveals that only the hydrophilic active esters were successful and that the acetonoxime active ester is only accessible via TFA-acetonoxime. The TFPS was most effective as charge interaction was already found to be decisive for the diffusion into the gel.^[58,174]

Table 7.1: Comparison of the mass of a bovine serum albumin (BSA) immobilized into the swollen NIPAAm-based gel by using different active esters. The thickness of swollen gel in acetate (ACT) buffer was $d_h \approx 1 \mu\text{m}$

Active ester	Activation in solvent	Immobilization in buffer with pH	Surf. mass density of loaded protein / $\text{ng}\times\text{mm}^{-2}$
TFA-AO	DCM	4	9
TFA-NHS	DCM	4-5	0
TFA-PFP	DCM	4-5	0
EDC-AO	Water	4-6	0
EDC-NHS	Water	4	0
EDC-TFPS	Water	4	63

7.1.3 Antifouling Properties

To investigate the nonfouling properties of the sensor matrix the TFPS activated hydrogel was functionalized with IgG and exposed to blood plasma. Firstly, a SPR/OWS spectra was taken of the reference, the gel swollen in PBS (spectra IV in fig. 7.3). Subsequent, the swollen gel was incubated in serum (spectra V in fig. 7.3). After rinsing with PBS (spectra VI in fig. 7.3), an increase of surface mass density of $\Delta\Gamma = 5 \text{ ng mm}^{-2}$ compared to the mass prior exposure to the serum was determined (see fig. 7.3 and table 7.5). This corresponds to very little attached plasma.

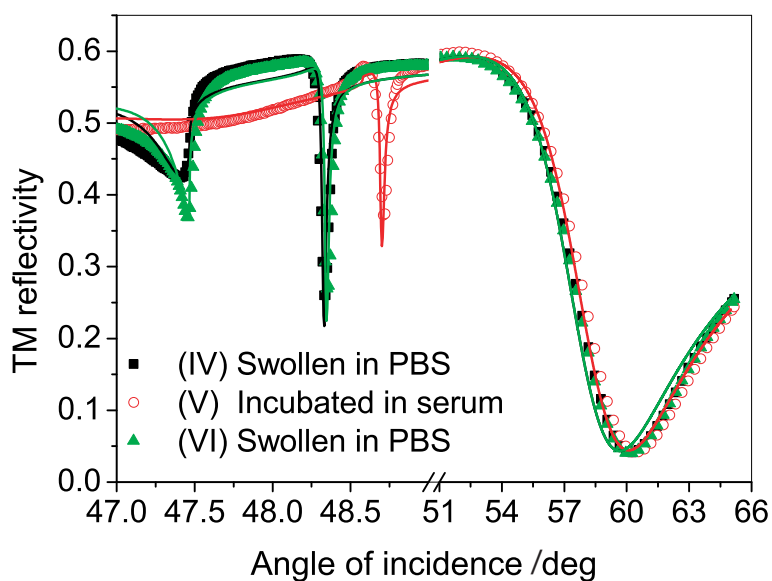


Fig. 7.3: Reflectivity spectra for the gel swollen in PBS (square), exposed to blood serum (circle), and after subsequent rinsing with PBS (triangle). The lines are the corresponding fits.

7.1.4 Detection of Neutravidin

To demonstrate that the functionalized hydrogel can be used as a sensor matrix, the affinity binding of NA to biotinylated IgG was studied. As depicted in figure 7.1, first, the attachment of IgG-b to the TFPS activated hydrogel was accomplished and monitored as shown in Fig 7.4.

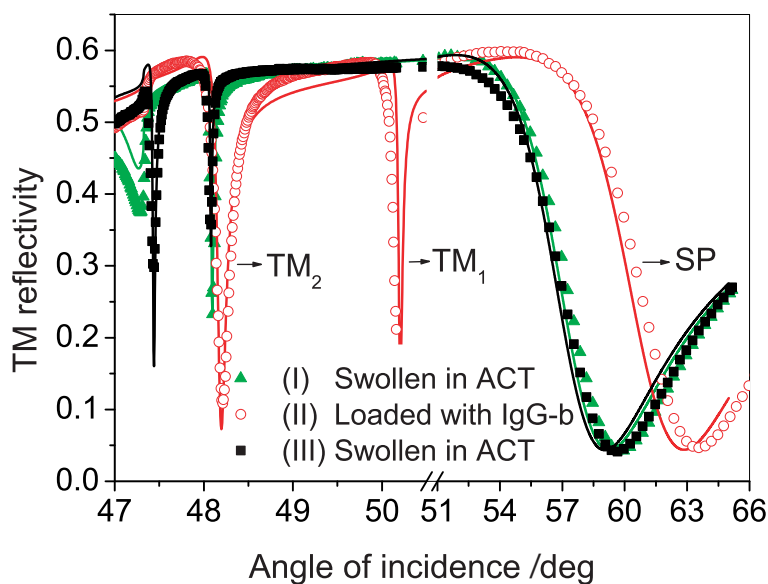
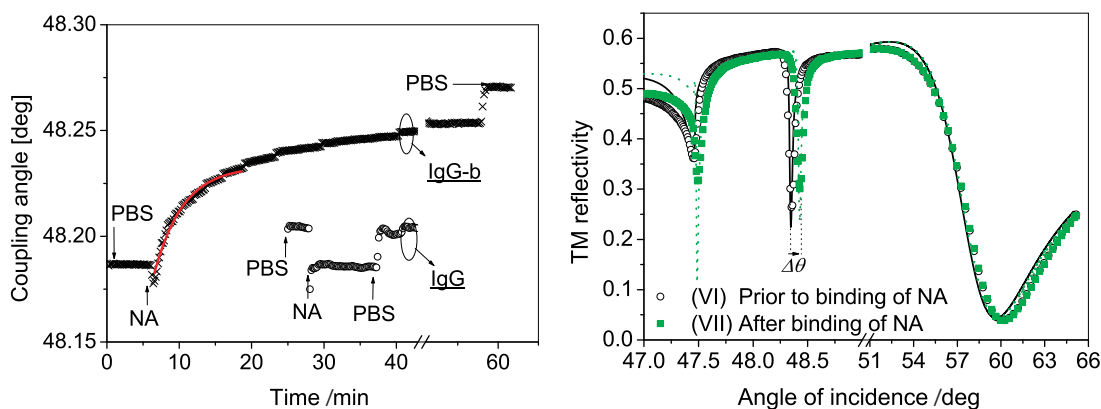


Fig. 7.4: Reflectivity spectra measured for the hydrogel film swollen in acetate (ACT) buffer (square), loaded with IgG-b (circle), and after incubation with ethanolamine and rinsing (triangle).

Figure 7.5 shows the time evolution of the angular position of the TM_1 resonant dip upon binding of NA to the functionalized hydrogel film. It was observed as a gradual increase of the coupling angle, which reached its saturation after approximately 40 min after addition of the NA dissolved in PBS. In the control experiment (same figure), no binding of NA was observed in the gel that was modified by IgG molecules without biotin tags.



	n_b	d_h [μm]	n_h	Γ [$\text{ng}\times\text{mm}^{-2}$]
(I) Swollen in ACT	1.3330	2.50	1.3467	171
(II) Loaded with IgG-b	1.3330	1.94	1.3757	407
(III) After passivation	1.3330	3.20	1.3449	190
(IV) Swollen in PBS	1.3347	2.38	1.3500	182
(V) Incubated in plasma	1.3480	2.20	1.3535	-
(VI) Swollen in PBS	1.3347	2.44	1.3500	187
(VII) After NA binding	1.3347	2.53	1.3507	203

Fig. 7.5: Left: Time evolution of the TM_1 coupling angle associated with the binding of NA to the gel modified with IgG-b and IgG. Right: Reflectivity spectra before (circle) and after (square) the affinity binding of NA to IgG-b modified gel and the corresponding fits (line). Bottom: Characteristics of the hydrogel film upon its modifications.

The diffusion characteristics as well as the association and dissociation binding constants of the reaction can be determined by fitting the measured kinetics with an appropriate model.^[175] The obtained association rate for NA ($\approx 10^3 \text{ M}^{-1}\text{s}^{-1}$) is two orders of magnitude lower than for the interaction between (strept)avidin derivatives and biotin ($\approx 10^5 \text{ M}^{-1}\text{s}^{-1}$ ^[176]). This slow down indicates that the binding in the gel was strongly diffusion controlled. Analyzing the angular spectra (VI to VII) in Figure 7.5 allocates the increase in the surface mass density to the specific binding of NA of 16 ng mm^{-2} (the mass density of immobilized IgG-b was 11 ng mm^{-2}). Taking the molecular weight of IgG (MW = 150 kDa) into account, which is 2.5-fold higher than that of NA (MW = 60 kDa), the av-

average number of NA molecules captured by an IgG-b molecule was determined to be 4.6 ± 1.1 . This result is within the expected range (3 to 6 biotin tags are anchored to an individual IgG molecule), and supports the concept of coupling IgG-b molecules to flexible polymer chains in a swollen hydrogel network to enable the efficient binding of the affinity partner molecules.

7.1.5 Conclusion and Outlook

A combination of surface plasmon resonance and optical waveguide modes spectroscopy (SPR/OWS) was employed for the time-resolved and quantitative study of affinity binding inside hydrogel films. SPR/OWS allows for the observation of changes in mass distribution in the network by the simultaneous and independent measurement of its thickness and refractive index. This technique was applied for the investigation of the coupling of protein molecules to the hydrogel film, by using a novel charge-attraction scheme based on a tetrafluorophenol sulfonate active ester. This strategy was employed as charge interaction was found to be decisive for the diffusion into the gel^[58,174] and active ester chemistry enables covalent attachment without exposing the protein to harsh conditions.

The functionalized hydrogel was used as a sensor matrix into which protein molecules can diffuse and affinity bind to the immobilized catcher molecules. The low unspecific binding of blood plasma and the NA control experiment reveals its good antifouling properties.

This proves the hydrogel to be a good candidate for potential applications in affinity biosensors.

7.1.6 Experimental Part

Film preparation A thin hydrogel film was deposited on a BP-thiol modified gold surface by spincoating from a 4 w% polymer solution in ethanol to obtain a 300 nm thick layer. The coating was UV-crosslinked with a dose of 2 J cm^{-2} .

Ex situ activation in dichloromethane sensor chips with attached hydrogel film were put into dichloromethane (DCM) with TFA-AO, TFA-NHS or TFA-PFP dissolved at 1 M concentration. After 15 hours incubation at room temperature, the sensor chips with activated hydrogels were rinsed with DCM, dried and mounted into the setup.

***In situ* activation in water** The carboxylic groups in the swollen gel were activated by 90 min incubation in a solution with TFPS and EDC, NHS and EDC or AO and EDC dissolved in water at a concentration of 21 and 75 mg mL⁻¹, respectively. Afterwards, the surface was rinsed with acetate (ACT) buffer (10⁻² M, pH 4) for 3 min and the solution with IgG-b (concentration of 100 mg mL⁻¹) was pumped through the cell for 75 min.

Functionalization with Proteins IgG, IgG-b and BSA (100 µg mL⁻¹) respectively were dissolved in ACT buffer at pH 4, which is below their isoelectric points, resulting in a positively charge and therefore a strong Coulomb attraction into the hydrogel in case of the TFPS active ester being used. The solutions were pumped through the cell for 75 min followed by rinsing with ACT buffer for 10 min. In case of IgG and IgG-b the remaining active esters where quenched with ethanolamine and the hydrogel washed again with ACT buffer for 15 min.

Affinity binding of NA After a stabile baseline was established in flowing PBS, a solution of NA dissolved in PBS at a concentration of 100 mg mL⁻¹ was flowed for 50 min. Unbound NA was removed by rinsing with PBS.

7.2 Cell-resistant Implant Coatings

7.2.1 Introduction

Glaucoma is a disease caused by an intraocular overpressure leading to a permanent damage of the optic nerve that can end in a loss of the visual field or even blindness. Typically, the inner pressure of the eye is between 10 and 21 mm Hg, resulting from an equilibrium between the production of aqueous humor by the ciliary body of the eye and its drainage. A reduced or blocked flow causes an overpressure which has to be corrected surgically.

Nowadays, stands with valves, such as the Ahmed valve (see fig. 7.6 right), are implanted to regulate the pressure and to avoid a collapse of the eye. Disadvantageously, these valves have a major drawback. Within a few weeks a fibrous capsule can form around them as can be seen in the lower left image of figure 7.6. Especially the young suffer from this body reaction to the implant, due to their higher metabolism.^[177,178]

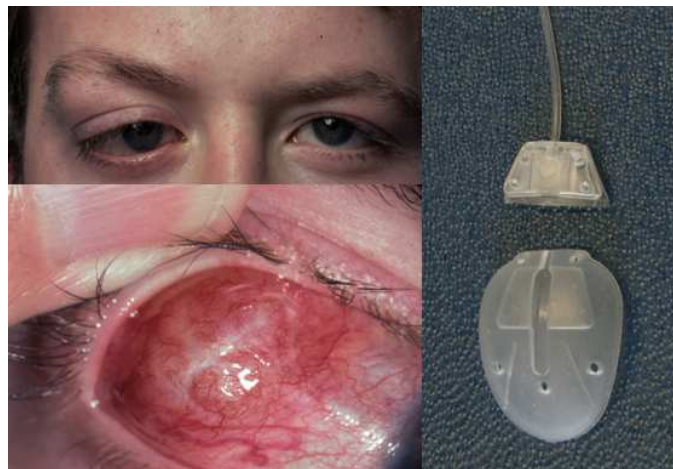


Fig. 7.6: The Ahmed valve (right) and the implanted Ahmed valve being encapsulated by fibroplasts (left). Courtesy of Lars Choritz.

To avoid this reaction, the pocket formed during surgery is treated with cytostatic drugs or cytotoxic antibiotics like paclitaxel and mitomycin. These drugs, being used in cancer therapy as well, hinder the body reaction but at the same time can damage the epithelial cells causing turbidity in the view.

To reduce the amount of therapeutics, the employment of hydrogel coatings on the valve as drug delivery agent was investigated.^[179] Even more desirable

would be a coating that decreases or inhibits the proliferation of tenonfibroblasts without using drugs.

Beyond the drug delivery, hydrogels exhibit a soft surface that might reduce the irritation of the surrounding tissue. However, a hydrogel has to be identified that can resist the attachment of cells. In the following, the PNIPAAm-based hydrogel is investigated on this issue.

PNIPAAm gels of various architectures are known from literature for their switchable interaction with cells.^[89,90,95,96] Their responsive behavior was used to attract cells above LCST and repel them in the swollen state. Only recently extremely dense PNIPAAm brushes showed repulsive interaction with cells above LCST.^[89] An overview about this discussion can be found in section 7.3 and in a recent review.^[56]

Most of these approaches had the problem of permanent adhesion due to the incomplete surface coverage by these sub-micron thick films. Contrary to these coatings, our hydrogel provides a complete coverage and micrometer thick film but on the same hand a surface softness, which is controllable by the crosslinking density.

7.2.2 Cell Experiments

In cooperation with Lars Choritz from the university hospital in Mainz who performed the cell experiments, hydrogel coated (see chapter 3) and non-coated PE petri-dishes were exposed to a solution of tenonfibroblasts, taken from patients during surgery, at a physiological temperature of 36°C. The evaluation and the images were performed with transmission light microscopy. The left image of figure 7.7 clearly shows the antiproliferative effect of the hydrogel coating. In comparison to the right image, where one can see the proliferated fibroblasts in the untreated petri-dish, the left image shows cells of spherical shape that do not proliferate or undergo cell division during the examined time of 48 h.

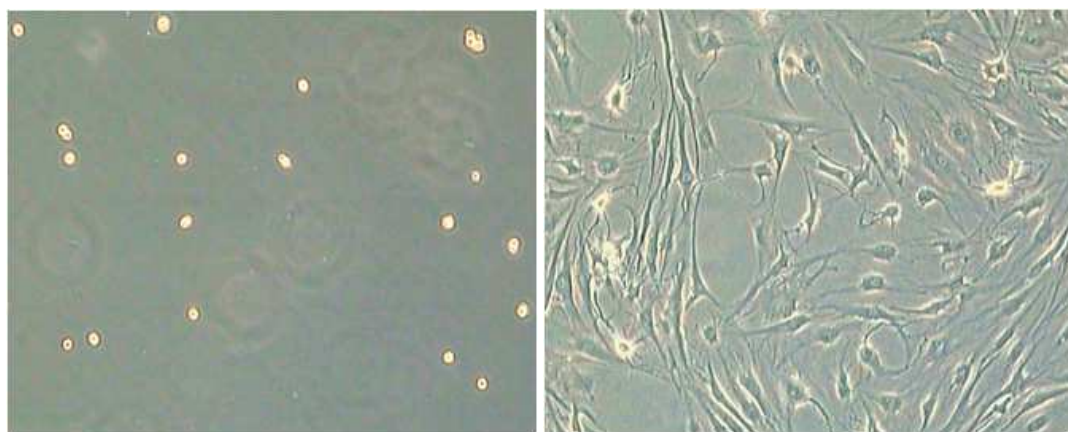


Fig. 7.7: Left: Non-proliferating fibroblasts on top of a hydrogel coated PE petri-dish.
Right: Proliferating fibroblasts on top of an uncoated petri-dish as reference.

As the Ahmed valve is made of silicone, it was tried to attach the hydrogel to silicone in form of a silicone coated petri-dish. Adhesion was achieved by the preliminary functionalization of the silicone with the BP-silane. The left image of figure 7.8 indicates the same behavior as for the hydrogel on the bare petri-dish, whereas the silicone coating (see fig. 7.8 right) seems to be less favored by the fibroblast compared to the PE surface of the bare petri-dish.

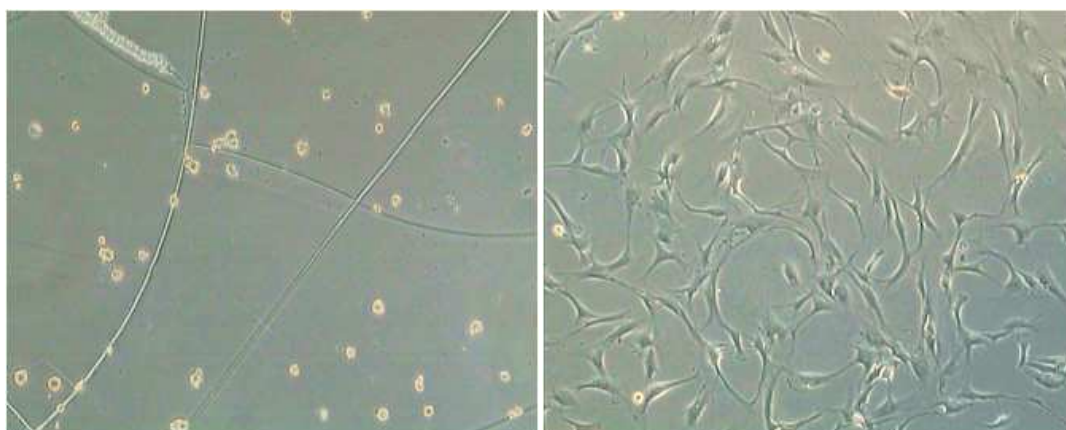


Fig. 7.8: Left: Non-proliferating fibroblasts on top of a hydrogel coated silicone petri-dish.
Right: Proliferating fibroblasts on top of an uncoated silicone petri-dish as reference.

The small ruptures visible in the left image of figure 7.8 were originated in the plasma treatment of the silicone prior to the functionalization with the BP-silane. A too long and harsh treatment caused heating and cracking of the silicone film. A plasma pretreatment under milder conditions is already developed.^[180] Interestingly enough, the cells on the hydrogel coating are neither necrotic nor apoptotic. Reseeded on a uncoated petri-dish they start proliferating again as can be seen in figure 7.9. This is highly desirable since cells that do not attach due to necrosis can cause inflammatory reactions on or in the neighborhood to the implant as known from coronal stands.^[54]

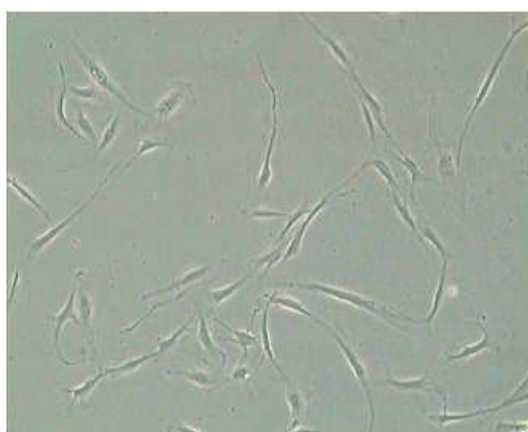


Fig. 7.9: Fibroblasts taken from the hydrogel coated petri-dish proliferating after being reseeded on an uncoated petri-dish.

7.2.3 Conclusion and Outlook

Contrary to literature the PNIPAAm-based hydrogel applied as coating prevents the attachment and proliferation on or above the surface under physiological conditions in the collapsed state. This property was under investigation using tenonfibroblasts, very robust cells and responsible for the keloid enclosing implants. These results indicate, that the chemical properties of a coating are not the only factor responsible for the interaction with biomaterial. Furthermore, they led to the implementation of the hydrogel in the joint research group of MPIP and Uniklinik Mainz on biomaterials, tissues and cells in surgery (BiomaTiCS). Employing the hydrogel where cell attachments has to be avoided and a supple surface is desirable as in soft tissues is therefore under ongoing investigation. In a next step the coating of the stand itself has to be achieved and the tolerance of a living organism towards the coated implant needs to be investigated. More detailed studies with very promising results on the viability of the fibroblasts, like flow cytometry and Alamar Blue assays are performed at the moment in our working group by Maria Wegner within the scope of her diploma thesis. Furthermore, the effect of less aggressive pharmaceuticals loaded into the gel to suppress the proliferation of the tenonfibroblasts is tested.

7.2.4 Experimental Part

Pretreatment The PE-dishes were processed in a plasma cleaner at 300 W with a partial pressure of 0.9 mbar Ar and 0.1 mbar O₂ for 1 min and 10 min for the dishes with a silicone coated bottom, respectively. This treatment enhanced the contact of the polymer mixture with the PE-dishes and enabled the functionalization of the silicone surface with the BP-silane, which was performed as described in section 3.2.

Dish coating The bottoms of the pretreated petri-dishes were covered with a mixture of 1.3 mL ethanol, 0.2 mL MilliQ and 0.5 ml of a 2 w% ethanolic hydrogel-polymer solution. The mixture was allowed to evaporate slowly and finally dried in a vacuum oven at 50°C over night. The coating was crosslinked with a dose of 6 J cm⁻².

7.3 Protein-resistant Coatings: A ToF-SIMS Study

7.3.1 Introduction

The unspecific adsorption of proteins and cells at interfaces is undesirable in many applications, because it reduces the performance of medical devices or biosensors and leads to encapsulation of implants.^[35,181–184] Such adsorption can be diminished by applying nonfouling coatings. During the last decade coatings with stimuli responsive behavior gained more and more interest. Especially poly-*N*-isopropylacrylamide (PNIPAAm) coatings were investigated for their use in drug delivery^[185,186] and their switchable interaction with proteins and cells. Various coating techniques were employed: brushes grafted from the surface by *in situ* free radical polymerization^[87,88] or by controlled radical polymerization techniques^[89–92] as well as grafting of functionalized PNIPAAm to a modified substrate.^[91,93,94] Others used e-beam^[95] and plasma polymerization.^[96–98] All these coatings showed the same behavior in terms of nonfouling: in the swollen state (below their LCST which is around 32°C) no adsorption of proteins or cells was observed whereas in the collapsed state (above their LCST) attraction of the biomaterial was found. These switchable properties were applied for channel coatings, tissue engineering and purification.^[38,39,91,94,95]

In many cases it was observed that some adsorbed material did not desorb while switching back from attractive to repulsive interaction.^[97,98,187,188] Cole *et al.*^[56] suggested this was caused by incomplete coating of the substrate by the polymer chains in the collapsed state. A similar phenomena was discussed earlier for PEG brushes.^[189–191] It was concluded that the adhesion properties of the coatings were governed by their structural properties rather than their chemistry. Okano *et al.*^[89] for instance found that on their PNIPAAm brushes above LCST the cell adsorption decreased with increasing brush density. Such nonfouling coatings at physiological conditions are highly desirable for implant coatings especially for those that have to maintain percolation.^[181,183,184] In addition one can only exploit its switching behavior to the full extent if it is nonfouling in both states.

This chapter presents the nonfouling properties of the crosslinked PNIPAAm-based hydrogel films in the swollen as well as the collapsed state. For two cross-linking densities, the repulsion of the proteins human serum albumin (HSA) and lysozyme (Lys) at room temperature in the swollen state as well as in the collapsed state at 37°C (see fig. 7.10) was proven by ToF-SIMS in cooperation with Marek Jasieniak and Hans Griesser at the Ian Wark Research Institute in Adelaide.

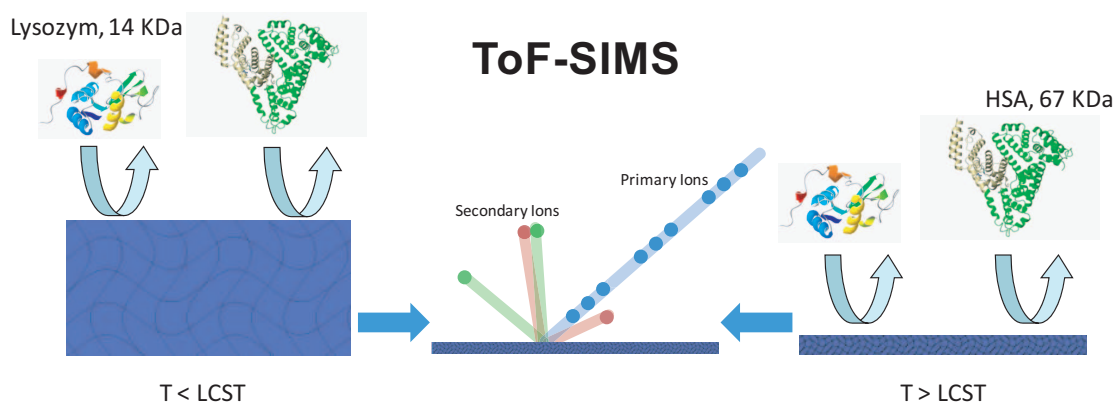


Fig. 7.10: Illustration of the protein repellent properties of the hydrogel in the swollen and collapsed state, investigated by ToF-SIMS.

An introduction to ToF-SIMS can be found in section 2.6 and in literature.^[81] The hydrogel films were exposed to proteins solutions in the swollen and collapsed state, subsequently rinsed and dried. These samples were characterized by ten positive and five negative mass spectra collected from different, non-overlapping areas. The limit of detection of a ToF-SIMS measurement is known to be in the order of a few ng/cm².^[192] Due to the complexity and amount of data obtained, principle component analysis (PCA) and analysis of means were employed to evaluate the sets of measurements.^[193,194]

7.3.2 ToF-SIMS Measurements

7.3.2.1 Evaluation of Negative Ionized Fragments

The adsorption of proteins was determined by evaluating the presence or absence of sulfur peaks in the negative (\ominus) ToF-SIMS spectra since the hydrogel coating contains no sulfur. In contrast the used proteins contain sulfur due to cysteine and methionine in their sequence. As a reference, hydrogel coated slides were exposed to phosphate buffered saline (PBS) according to the procedure for proteins as described above for both crosslinking densities (30 min (HG-30+PBS) and 60 min (HG-60+PBS) crosslinked).

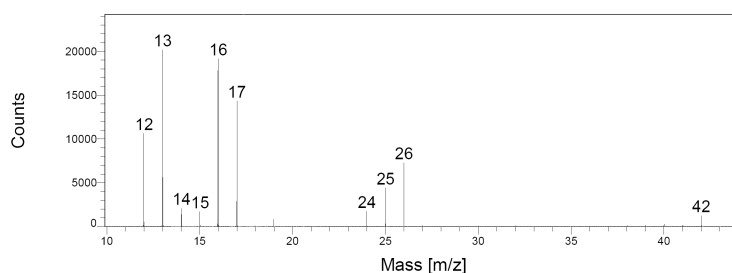


Fig. 7.11: ToF-SIMS (\ominus) spectra of 60 min crosslinked hydrogel coating (HG-60+PBS).

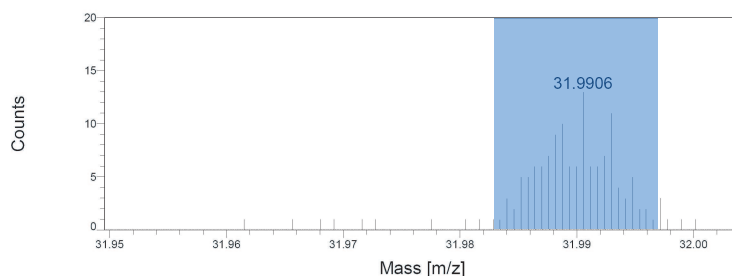


Fig. 7.12: Enlargement of figure 7.11. $m/z = 31.9898$: oxygen peaks (blue).

The ToF-SIMS spectrum of the negative ionized fragments of a highly crosslinked coating (see fig. 7.11) shows the characteristic fragments of a PNIPAAm coating like NH ($m/z = 15.011$), CN ($m/z = 26.002$) and CNO ($m/z = 41.996$). The enlargement (see fig. 7.12) shows the peaks for oxygen around $m/z = 31.99$ and no peaks corresponding to sulfur around $m/z = 31.97$. Figures 7.13 and 7.14 in contrast show the respective spectra for HSA and lysozyme with additional peaks around $m/z = 31.97$ which are characteristic for sulfur.

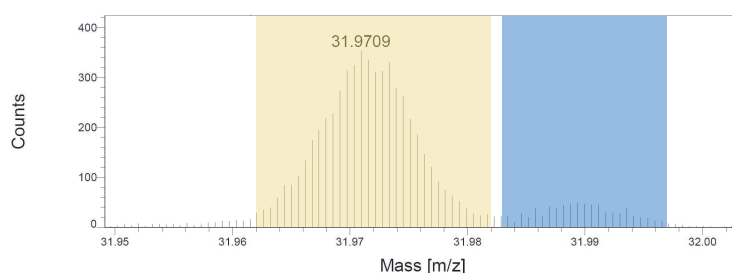


Fig. 7.13: ToF-SIMS (\ominus) spectra of HSA. $m/z = 31.9721$: sulfur peaks (yellow), $m/z = 31.9898$: oxygen peaks (blue).

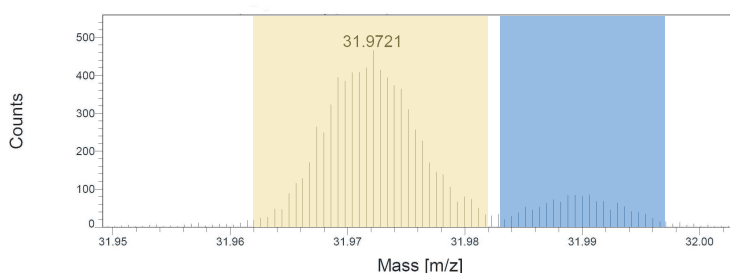


Fig. 7.14: ToF-SIMS (\ominus) spectra of lysozyme. $m/z = 31.9721$: sulfur peaks (yellow), $m/z = 31.9898$: oxygen peaks (blue).

After the hydrogels were exposed to proteins (see figs. 7.15 - 7.18) none of the measured spectra showed a significant increase of counts around $m/z = 31.97$ corresponding to sulfur. The spectra of the collapsed hydrogels even showed a slight decrease. The absence of sulfur revealed the protein repelling properties of the PNIPAAm-based coatings below and above their LCST.

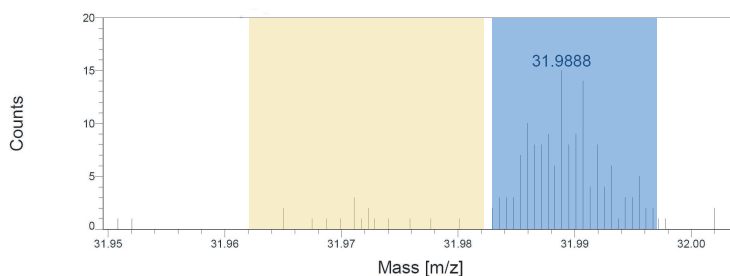


Fig. 7.15: ToF-SIMS (\ominus) spectra of HG-60 after exposure to HSA in the swollen state at RT (HG-60+HSA 20°C).

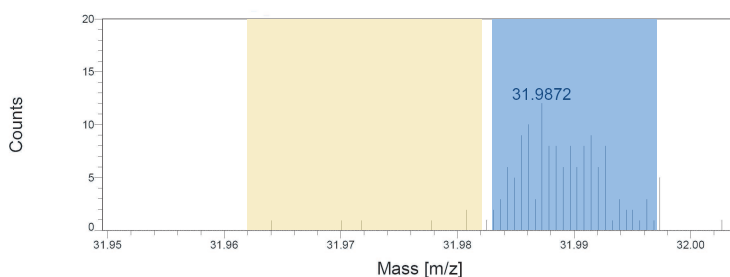


Fig. 7.16: ToF-SIMS (\ominus) spectra of HG-60 after exposure to HSA in the collapsed state at 37°C (HG-60+HSA 37°C).

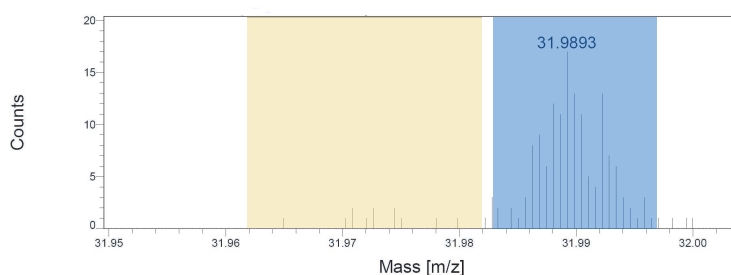


Fig. 7.17: ToF-SIMS (\ominus) spectra of HG-60 after exposure to lysozyme in the swollen state at RT (HG-60+Lys 20°C).

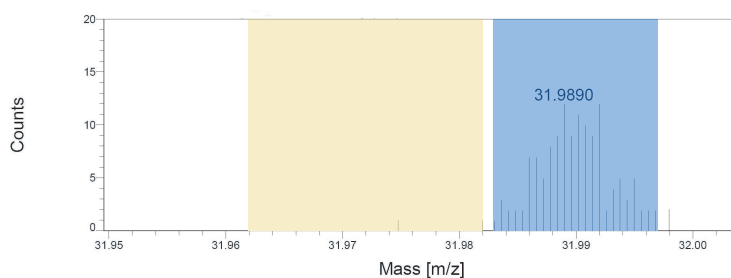


Fig. 7.18: ToF-SIMS (\ominus) spectra of HG-60 after exposure to lysozyme in the collapsed state at 37°C (HG-60+Lys 37°C).

A summary of the measurements can be found in figure 7.19. It shows the counts of the sulfur signal of the references (HG-30+PBS and HG-60+PBS) and the samples exposed to the proteins at 20°C and 37°C respectively, normalized to the overall counts.

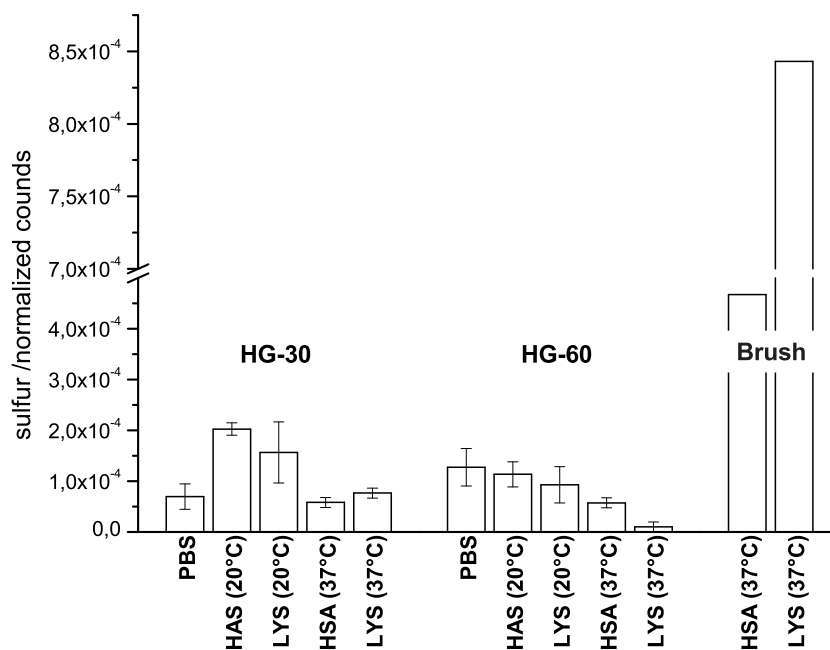


Fig. 7.19: Comparison of the measured counts of sulfur in ToF-SIMS (\ominus) normalized to the overall counts. The reference for proteins adsorbed on a PNIPAAm brush was kindly provided by Martin Cole.

The spectra recorded on low crosslinked hydrogel coatings indicated the same behavior for the collapsed gels. In the swollen gels a slightly higher amount of sulfur was detected. We believe this is due to more careful rinsing of the very soft coating, since Dostálek *et al.* already reported on the nonfouling properties of the swollen hydrogel presented here.^[58,61] To underline the quality of the nonfouling property, the adsorption of proteins on a PNIPAAm brush at 37°C is depicted for comparison. The data of the PNIPAAm brush were kindly provided by Martin Cole from the Ian Wark Research Institute in Adelaide.^[88,195]

7.3.2.2 Evaluation of Positive Ionized Fragments

The determination of protein adsorption measured within the positive (\oplus) fragments of ToF-SIMS was done by comparing the signal intensity of certain mass fragments before and after the exposure to proteins. In order to decrease the amount of data only peaks corresponding to known protein fragments were evaluated.^[196] The fragments and the corresponding proteins are stated in the respective graph in figure 7.20.

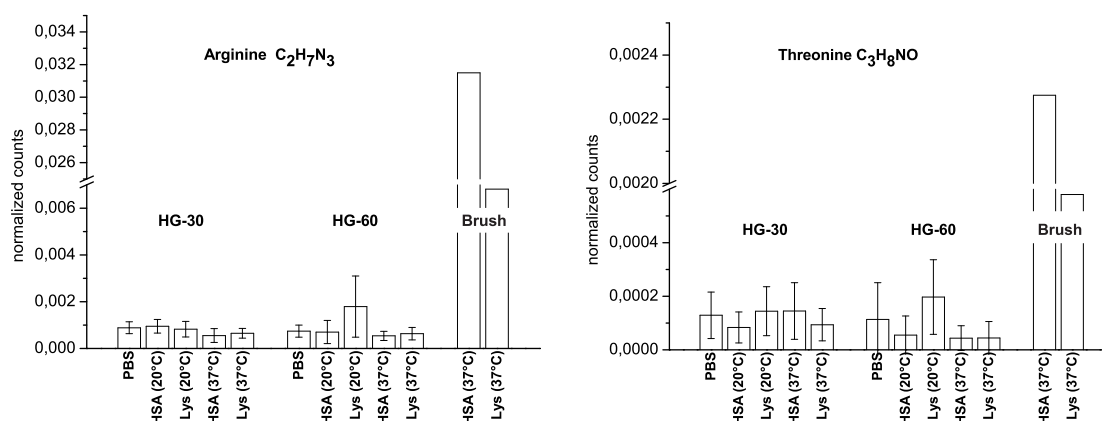


Fig. 7.20: Comparison of the counts measured for the respective fragment in ToF-SIMS (\oplus) normalized to the overall counts. The reference for proteins adsorbed on a PNIPAAm brush was kindly provided by Martin Cole.

The graphs in figure 7.20 show the measurements before and after exposure to proteins as described for negative fragments above. They depict the counts, normalized to the overall counts, of fragments corresponding to arginine and threonine. Fragments of glycine, alanine, valine, asparagine, proline, and glutamic acid were found as well, but showed even less fluctuation. None of the mass fragments showed a significant increase in intensity after contact with proteins, which confirms the results of the negative fragments in ToF-SIMS that no adsorption of proteins took place in the swollen or collapsed state. The adsorption of proteins

on a PNIPAAm brush at 37°C is depicted for comparison and were kindly provided by Martin Cole from the Ian Wark Research Institute in Adelaide.^[88,195]

7.3.2.3 Evaluation by Principle Component Analysis

In addition to the evaluation of positive mass fragments described above, PCA was employed to retrieve changes in the hydrogel coatings after exposure to proteins. In PCA the intensity of groups of peaks (e.g. corresponding to CH_2^+) for each measured spectra is collected in a matrix. The first most significant 'principal component' (PC1) considers as much variability of this matrix as possible, so does the second (PC2), perpendicular to the first and therefore uncorrelated. Thus, this method does not compare single mass fragments but a set of fragments representative for the sample as a whole. Each measurement is represented by a sign (score) in the score plot.

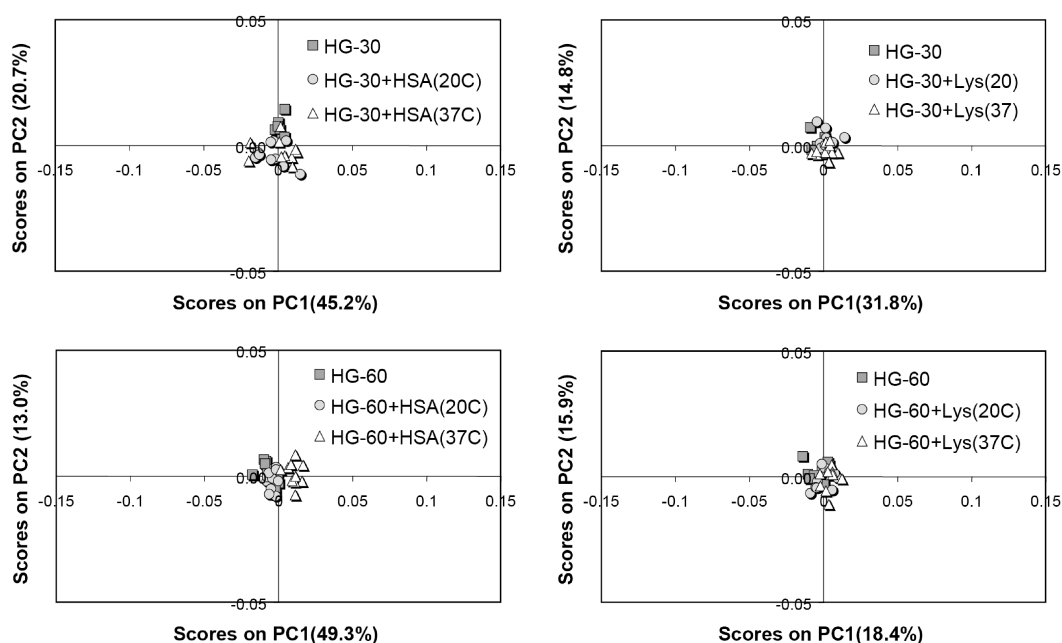


Fig. 7.21: Score plots of positive fragments by PCA.

The score plots in figure 7.21 describe the similarity between the reference samples and the respective exposed ones for the two proteins (HSA and lysozyme), temperatures, and crosslinking densities. Its axis PC1 and PC2 represent the majority of the variation within the data, condensing 35 % to 65 % (addition of the scores) of the ToF-SIMS spectra information. The score plots show an overlapping or close proximity of the data sets. More important than the value on the axis is

the comparison between the scattering of the scores (cluster) of one sample and the distance to the scores of an other sample. Score plots that indicate strong adsorption show a distinct separation of the cluster, as can be found for PNIPAAm brushes in literature.^[195] Hence, figure 7.21 indicates there is no significant difference between the investigated samples, which implicates no adsorption of proteins regardless of temperature, crosslinking density and protein.

7.3.3 Conclusion and Outlook

Contrary to literature the applied hydrogel exhibits protein repelling properties in the swollen as well as in the collapsed state.^[87,88,90-96] The interaction with proteins described above is in line with the behavior of very dense PNIPAAm brushes reported by Okano *et al.*^[89] Their behavior, however, was explained by the brushes losing their ability to collapse with increasing density as can be recognized by the changes in the contact angle. For the highest density they reported a contact angle in "collapsed" state below 36° , which is contrary to other reports that state a static contact angle for water above LCST of higher than 70° .^[88,92,197] Our hydrogel exhibits a contact angle above LCST of $74.8^\circ \pm 2.6^\circ$. It swells and collapses with a change in thickness up to a factor of 10 depending on the irradiation dose,^[60] nevertheless maintaining a complete surface coverage due to its thickness and network structure. This ability to take up and release a large amount of solvent combined with nonfouling in both states makes this coating a promising candidate for implant coatings combined with local drug delivery and as biosensor matrix.

These results indicate, that the interaction with biomaterials is not solely determined by the surface chemistry of a coating but also by its structural properties like surface coverage. Moreover, as the adsorption of proteins can trigger the growth of cells, they supports the application as implant coating in soft tissue presented in chapter 7.2. It verifies earlier studies on nonfouling properties as well (see sections 5.1 and 7.1).

7.3.4 Experimental Part

A second batch of samples was kindly provided by Coenraad van den Brom.

Film preparation A thin hydrogel film of approximately $1.1\mu\text{m}$ thickness was deposited on a 140 mm^2 silicon chip, functionalized with BP-silane, by spincoat-

ing from a 10 w% ethanolic solution. The coating with a low crosslinking density (HG-30) was irradiated for 30 min with a total energy density of 3.14 J cm^{-2} and 6.28 J cm^{-2} for the 60 min crosslinked (HG-60) respectively.

Exposure to proteins The hydrogel-coated slides were incubated at 20°C with $75 \mu\text{L}$ HSA (67 kD, 0.2 mg/mL in PBS) and lysozyme (Lys, 14 kD, 0.2 mg/mL in PBS) respectively. After 2 h the slides were washed with MilliQ. For the nonfouling investigations at 37°C all solutions and slides were placed in an incubator for at least 4 h before the experiments were carried out inside the incubator as described above.

ToF-SIMS The ToF-SIMS analyses were performed with a PHI TRIFT II (model 2100) spectrometer (PHI Electronics Ltd, USA) equipped with a ^{69}Ga liquid metal ion gun (LMIG). A 15 keV pulsed primary ion beam was used to desorb and ionize species from the sample surface. Pulsed, low energy electrons were used for charge compensation. Mass axis calibration was done with CH_3^+ , C_2H_5^+ and C_3H_7^+ in positive mode and with CH^- , C_2H^- and Cl^- in negative mode of operation.

PCA was carried out using PLS_Toolbox version 3.0 (Eigenvector Research, Inc., Manson, WA) operating on the MATLAB platform (MATLAB version 6.5, The MathWorks Inc., Natic, MA).

7.4 A Hydrogel-supported ptBLM

7.4.1 Introduction

The introduction of a hydrogel-supported protein tethered bilayer lipid membrane (ptBLM) was a cooperation with Asmorom Kibrom who prepared the ITO, established the membrane and performed the measurements, Ulrich Jonas, Bernhard Menges and Renate Naumann.

The lipid bilayer membrane plays a prominent role in many biologically relevant processes, e.g. signal transduction, transport of ions and molecules, biosynthesis, cell adhesion and recognition. Consequently, there is great interest in model systems that would allow for a systematic study of such processes with a reduced amount of variables under controlled conditions. Assembling the membrane on a planar substrate paves the way for a large variety of surface-analytical tools that could then be employed for such investigations. Biomimetic membrane systems have been developed such as solid-supported bilayer lipid membranes (sBLMs), and hybrid bilayer lipid membranes,^[84,198–201] in which the bilayer is directly attached to the substrate. The drawback of these systems is the complete lack of a hydrophilic space that separates the lipid from the support. Proteins incorporated into such a membrane experience denaturation upon contact with the surface. To overcome this drawback, tethered bilayer lipid membranes (tBLMs) were developed, separating the lipid from the support by a short (< 3 nm) spacer.^[83,202–205] These tethers create a small submembrane volume of typically 0.3 nL cm^{-2} . However, this space does not accommodate a sufficiently large amount of water molecules to mimic the cytosolic space. The idea of using macromolecules as a "cushion" to mimic the cytosol/cytoskeleton of the cell to create such a hydrophilic space between membrane and solid support was first introduced by Ringsdorf and Sackmann.^[206–208] Since then, polymer-supported lipid membranes have been widely used, as documented in several major review articles.^[84,209] However, they were mostly applied as a model system of the cell surface rather than a model system for ion transport through proteins. An example of such an approach was presented only recently employing a hydrogel made from P(NIPAAm-co-MaBP), with a swollen thickness of up to 90 nm.^[210] Many of these systems do not exhibit the giga-seal, i.e. a $\text{G}\Omega$ resistance, a requirement known from patch clamp techniques, which limits their application. Employing an electrically high sealing membrane is mandatory to separate the

signal of the receptor from the leak current of the membrane. Highly insulating polymer-supported membranes have been prepared, though in rare cases, given that a very smooth surface of the hydrophilic polymer could be achieved.^[211] Alternatively, specifically designed lipopolymers were employed, which were pre-oriented by the Langmuir-Blodgett technique.^[212,213] However, the electrically sealing of polymer-supported membrane remains a challenge.

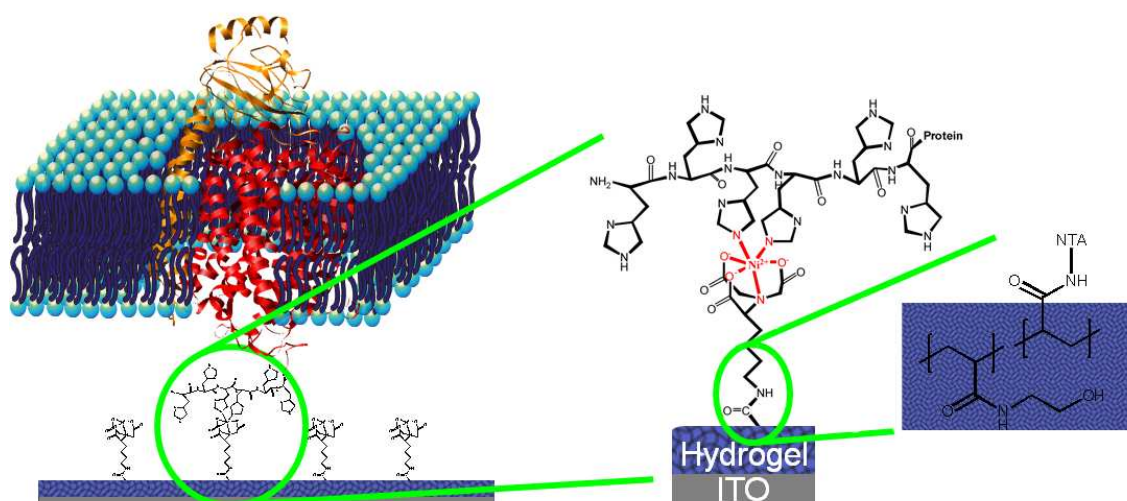


Fig. 7.22: Scheme of the hydrogel-supported ptBLM on ITO.

The approach presented here is to assemble a membrane by immobilizing the protein to be investigated in the first step specifically on the top layer of polymer coated indium-tin oxide (ITO) (see fig. 7.22). This can be achieved by using a hydrogel-polymer layer with mesh sizes smaller than the size of the protein and a functionality that allows to attach a binding motif such as nitrilo-triacetic acid (NTA). Chelated with Ni^{2+} ions, NTA is designed to bind the protein via the well-known his-tag technology. Since the protein is too big to penetrate the gel, it stays on the surface. A lipid bilayer, assembled around the protein, should enable the formation of a defect-free electrically sealing protein-lipid layer. A similar approach has been successfully applied before, but on a short spacer layer rather than a polymer.^[207,214,215] The sealing properties of this so-called protein tethered bilayer lipid membrane (ptBLM) were sufficient to allow for electron and ion transport processes through the cytochrome c oxidase (CcO).

To meet the requirements stated above, the hydrogel employed in the previous chapters of this thesis was adapted by increasing the amount of the functional monomer to maximize the surface-functionality and by increasing the crosslinking density to prevent the protein from diffusing inside the gel. Poly(*N*-(2-hydroxyethyl)acrylamide-co-5-acrylamido-1-carboxypentyl-iminodiacetate-co-4-benzoylphenyl methacrylate) (P(HEAm-co-NTAAm-co-MABP)) was prepared by polymer analogous reactions and offers a NTA moiety to bind CcO via the his-tag technology.

As substrate optically transparent ITO was used, different from previous studies using metal films.^[207,214,215] The advantage of using ITO as a substrate is the possibility to apply a number of surface-analytical techniques such as optical waveguide mode spectroscopy and fluorescence techniques not applicable on metal films. Electrochemical techniques may also be applied, e.g. in order to demonstrate that the protein residing in the hydrogel-supported lipid bilayer is functionally active.

7.4.2 Hydrogel-smoothed ITO

The ITO layers were prepared by DC sputtering on glass slides, with a DC power set to a constant value of 100 W. As the oxidation state of the ITO target influences the properties of the sample, after cleaning by sputtering with pure argon (15 min, $P = 3 \times 10^{-3}$ mbar), pre-sputtering was conducted with a process pressure P of 1×10^{-2} mbar and 10% vol. oxygen for 15 min. Finally, pure argon was used for the deposition on the glass substrates. After a deposition time of usually 10-15 min, a layer thickness of 80-120 nm, measured by step-profiler and ellipsometry, with a sheet resistance R_s of the ITO layer around $20 \Omega/\text{sq}$ was achieved. The sputtering procedure was optimized in terms of good optical and electrochemical properties of the layer, whereby the surface needed to have a low roughness. Previously, this finding led to a similar procedure used to sputter alumina.^[216]

The electrochemical properties and stability of the ITO layer was investigated by EIS. Spectra were recorded in PBS at varying time intervals, showing a decreasing resistance R and increasing capacitance C . After 24 h the equilibrium was reached with $R \sim 55 \text{ k}\Omega \text{ cm}^2$ and $C \sim 13 \mu\text{F}/\text{cm}^2$. An explanation for this behavior can be buffer diffusing into the ITO layer, reaching an equilibrium after ~ 24 h. Since water has a dielectric constant of 80, the capacitance is expected to increase as was observed in this case. The fact that the ITO layer was prepared by sputtering and

the grainy surface structure observed in AFM (see fig. 7.23) support the concept of a nanoporous structure that allows the uptake of buffer. Similar behavior were found for sputtered alumina^[152] and other nanoporous films.^[217,218]

The surface morphology of the ITO was recorded by AFM (see fig. 7.23), showing a smooth surface (Rms = 0.65 nm) with scattered spikes having a diameter of ~ 75 nm and a height of ~ 10 nm. These spikes are a major factor that could decrease the sealing quality of the membrane. Hence, the hydrogel coating on the ITO layers was employed to cover these spikes.

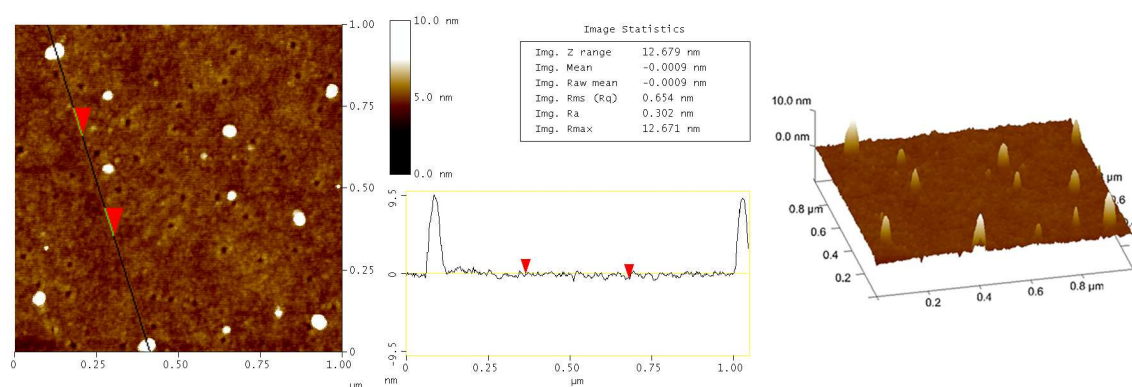


Fig. 7.23: AFM image of the ITO surface exhibiting a good roughness but spikes with a height in the order of 10 nm.

The hydrogel was obtained from highly crosslinked poly(pentafluorophenol acrylate-co-4-benzoylphenyl methacrylate) (P(PFPA-co-MABP)) in a tree step reaction as depicted in figure 7.24.

P(PFPA-co-MABP) was prepared by free radical polymerization from 98 mol% PFPA and 2 mol% MABP, for details see experimental part. In the first step, a 66 nm thick precursor copolymer layer was spincoated on a BP-silane functionalized (see section 3.2) ITO surface and UV-crosslinked. Thereby, the ITO was planarized and a chemically and physically durable surface was provided with a

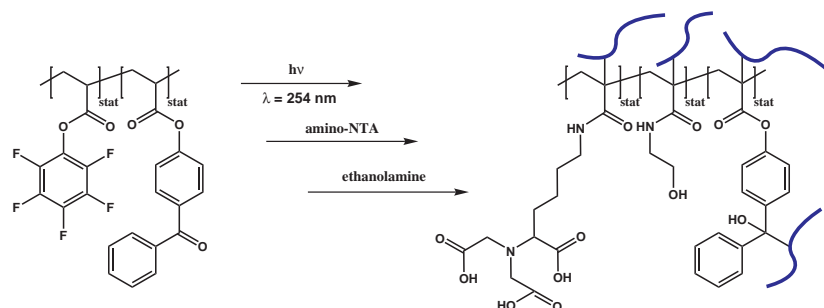


Fig. 7.24: Preparation of the PHEAm-hydrogel with attached NTA (P(HEAm-co-NTAAm-co-MABP)) from the precursor polymer P(PFPA-co-MABP).

high density of the hydrophobic pentafluorophenol active ester. These functional groups exhibit a high reactivity towards amines and prevent the swelling during the coupling of amino-NTA in aqueous media in the second step. This led to a NTA-functionalization preferentially at the polymer-water interface. Moreover, the subsequent reaction with ethanolamine turns the copolymer to the hydrogel. Such a coating fulfills the criteria mentioned in the introduction, namely providing a stable, smooth, hydrophilic and reactive surface. Stability and surface roughness can be influenced by molecular weight and amount of crosslinker. The employed copolymer was optimized in this regard, resulting in a durable coating of low roughness (see fig. 7.25).

The AFM measurements, depicted in figure 7.25, showed the protrusions on the ITO layer almost completely covered by the polymer layer. Furthermore, the coating exhibit a mean roughness of $R_{ms} = 0.49$ nm, which is of high importance for the assembly of a membrane with excellent sealing qualities.

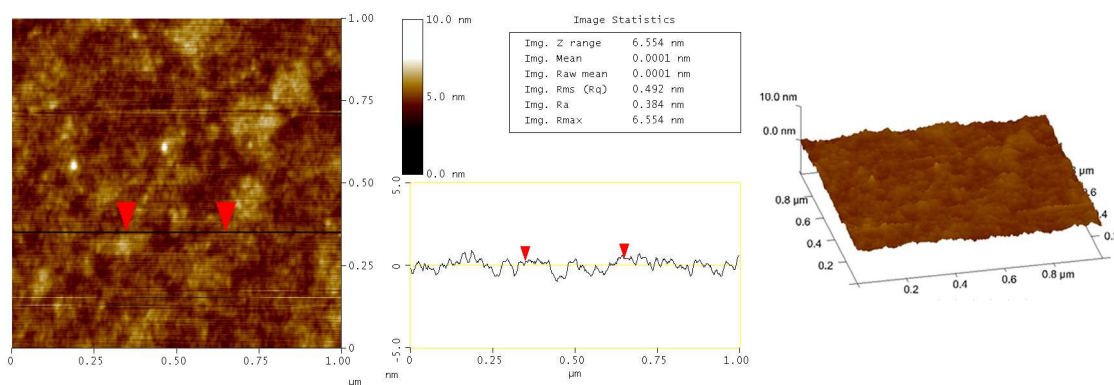


Fig. 7.25: AFM image of the hydrogel coating covering the spikes and flattening the ITO-surface.

Electrochemical impedance spectra showed a dramatic increase of the capacitance and a decrease of the resistance due to the functionalization of the precursor polymer (see fig 7.26). The lower capacitance and the higher resistance of the P(PFPA-co-MABP) can be explained by the hydrophobic active ester functionalities, resulting in a very low concentration of buffer inside the polymer layer. The capacitance of the layer structure is thus determined by the space charge capacitance of the semiconductor.

When the active ester was functionalized with hydrophilic groups such as NTA and OH, the buffer concentration inside the polymer layer increased. The gel formed a Guy-Chapman-like electrical double layer with capacitances in the order of $13\text{--}15 \mu\text{F}/\text{cm}^2$, actual values depend on the particular preparation. The resistance of this layer was in the range of few $10 \text{ k}\Omega \text{ cm}^2$.

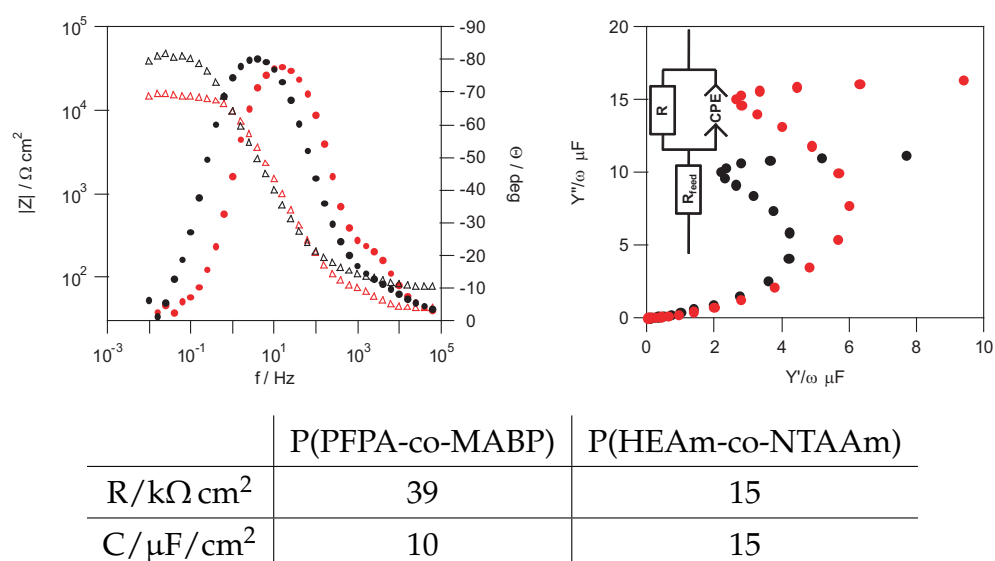


Fig. 7.26: Electrochemical properties of the polymer coated ITO before (black) and after (red) conversion with ANTA and ethanolamine in Bode-plot (left) and admittance-plot (right). The fitted values are depicted in the table below the spectra and the employed equivalent circuit is shown in the inset of the admittance-plot.

7.4.3 Formation of the Supported Membrane

The NTA functionalities were converted to the Ni-NTA chelate by immersion of the gel layer into a buffered Ni₂SO₄ solution. The excess of nickel ions were removed by rinsing with an acetate buffer solution (pH=5.5). Subsequently, a solution in detergent (n-dodecyl-β-D-maltoside, DDM) of Cytochrome c oxidase from Rh. Sphaeroidis with a his-tag attached to subunit II was added to the bathing solution. Finally, the lipid bilayer was formed by adding a phospholipid (DPhyPC) and biobeads in a DDM solution to the CcO layer. Biobeads are macroporous polystyrene beads of ~ 0.5 mm diameter that adsorb the DDM, hence triggering the formation of the membrane.

7.4.3.1 EIS-Measurements

As can be observed in figure 7.27, the formation of the protein layer (black) did not change the impedance or the capacitance of the system significantly. However, when DiPhyPC was added (blue), the resistance increased by two orders of magnitude to reach values around 1 MΩ cm². This indicates the insertion of lipid bilayer patches between the CcO molecules, i.e. the formation of a ptBLM. EIS data are collected in the table below the plots. The resistance in the order of 1 MΩ cm² is in accordance with results obtained for ptBLMs on smooth gold

films without a gel layer.^[51,207,215] The resistance is known to be a very critical indicator for a defect-free lipid bilayer. Values in the order of magnitude of $M\Omega\text{ cm}^2$ are known from BLMs and tBLMs, whereas for polymer-supported bilayers such high sealing resistances were hard to achieve. The capacitance was not affected strongly since it is dominated by the capacitance of the gel as well as the protein layer, which are expected to be in the same order of magnitude. The high resistance after dialysis indicates that CcO molecules were bound mainly to the surface layer rather than inside the gel layer, as they can only form a closed protein-lipid layer when attached leveled.

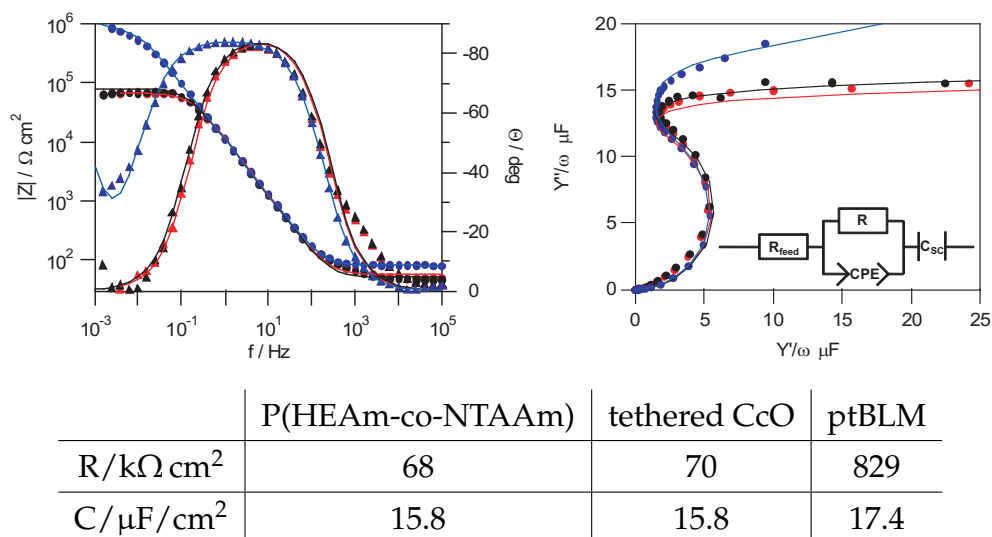


Fig. 7.27: Evolution of the electrochemical properties of the system while establishing the ptBLM on the hydrogel coating (red). The evaluation of the Bode- (left) and the admittance-plot (right) of tethering the CcO (black) and the ptBLM (blue) was performed using the equivalent circuit shown in the inset of the admittance-plot. The fitted values are depicted in the table below the spectra.

Finally, the enzymatic activity of the CcO was probed by EIS upon adding reduced cyt c to the hydrogel-supported ptBLM, as previously performed on a ptBLM without polymer cushion.^[51] When CcO – in the conformation used in this study – oxidizes the reduced cyt c, protons are pumped from outside the membrane to the submembrane area, resulting in a decreasing resistance. Indeed, after the cyt c was added, the resistance decreased at least by an order of magnitude and could be restored by removing the cyt c via rinsing with fresh buffer as the Bode-plot in figure 7.28 shows.

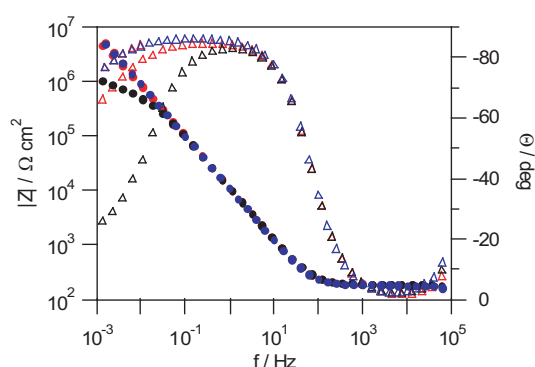


Fig. 7.28: Changes in the impedance (Bode-plot) of the hydrogel-supported ptBLM (blue) upon addition of cyt c (black). After rinsing with buffer to remove the cyt c (red), the impedance is mostly restored.

These data proved the functionality of the protein inside the lipid bilayer as can be concluded from the almost complete restoration of the resistance after removal of cyt c and are very well comparable to previous measurements with the ptBLM on gold surfaces.^[51]

7.4.4 Conclusion and Outlook

A gel-supported ptBLM was formed by attaching the protein to a pentafluorophenol-based copolymer. The very hydrophobic PFP-groups were converted into hydrophilic NTA and OH functionalities. The former were shown to bind the protein via the his-tag technology, whereas the latter provide hydrophilic end groups to form a hydrogel. This concept was shown to work in the direction of very robust polymer-supported protein-lipid layers. The polymer was highly crosslinked in order not to allow for a protein the size of the CcO to penetrate the polymer network. The presence of a well-ordered lipid bilayer with functional proteins could be demonstrated by measuring the electric current caused by the oxidation of cyt c by CcO in EIS.

A measurable response of a membrane-supported protein can be employed to detect analytes in the surrounding medium. Hence, such a system might be developed towards an application as biosensor.

7.4.5 Experimental Part

7.4.5.1 Preparation of the Substrate

Sputtering of ITO ITO layer were deposited on float glass (Menzel) by DC sputtering in a Balzer sputtering system. The target used was a 3 inch $\text{In}_2\text{O}_3:\text{SnO}_2$ (90:10) disk from MaTek. The base pressure was 5.5×10^{-6} mbar. Prior deposition the ITO target was pretreated without the samples for 15 min at 1.1×10^{-2} mbar total gas pressure and 100 W DC power. Oxygen partial pressure was kept at 1.7×10^{-3} mbar. Glass slides were cleaned in piranha solution ($\text{H}_2\text{O}:\text{H}_2\text{SO}_4:\text{H}_2\text{O}_2$; 5:1:1 v/v) and rinsed with MilliQ. After precleaning 100 nm ITO were sputtered on top of the glass slides without oxygen using pure argon atmosphere at 2.7×10^{-3} mbar and 100 W. Conductivity of the layer was measured by the four contact method after van-der-Paw. The crystalline structure of the ITO surface was analyzed by AFM and the thickness was verified by profilometer and ellipsometry.

Ellipsometry measurements Ellipsometry measurements were performed using a EP³ System (Nanofilm Technologies). Refractive index and absorption coefficient of the ITO layer were measured by scanning at angles close to the Brewster angle of ITO (62°). The data were analyzed using the EP³ View software (v2.3). The thickness of the ITO layer was estimated by profilometer. The refractive index n_g of the glass substrate was taken to be 1.55.

Polymerization of PFPA-co-MABP The reactive copolymer was polymerized from 98 mol% PFPA and 2 mol% MABP by free radical polymerization with 0.2 mol% AIBN in dioxane at 60°C for 48 h. It was precipitated in methanol and obtained with a yield of 78% after reprecipitating three times from benzene in methanol. The molecular weight M_n was determined by GPC (in THF with PMMA as standard) to be ~ 14.000 g/mol and the molecular weight distribution was ~ 2.1 . The $^1\text{H-NMR}$ shows the peaks of the PFPA and the MABP with a ratio of 98 : 2 as intended by the monomer mixture. $^1\text{H-NMR}$ (700 MHz, CD_2Cl_2): (ppm) = 7.45 (br m, 9H, benzophenone), 3.11 (br s, 1H, CH, backbone), 2.15 (br s, 2H, CH_2 , backbone), 1.48 (br m, 3H, CH_3 , backbone).

Preparation of the gel layer The BP-silane functionalized ITO slides were spin-coated with the copolymer from chloroform solution (1 w%), dried over night at 50°C under vacuum and crosslinked with a wavelength of 254 nm and a total energy of 60 J cm^{-2} .

AFM measurements Atomic force microscopy was performed using the AFM Dimension 3100CL Olympus (Veeco) in tapping mode and a silicon cantilever. In order to check for large scale variations, three different locations on the surface, each one having an area of $1 \times 1 \mu\text{m}$, were scanned at low resolution. Finally one area in the center of the sample surface was chosen and scanned using the highest resolution (512x512 lines). Using Nanscope (v2.5r) software, the height profile images were analyzed in terms of root mean square (RMS) and height measurement of single features on the surface.

7.4.5.2 Preparation of the Membrane

Functionalization with NTA The polymer coated ITO samples were incubated for 2 h in a 0.15 M amino-NTA solution (pH 9.8, 0.5 M K_2CO_3 buffer). After 2 h the polymer layer was further functionalized for 30 min in the same solution by adding 50 μL ethanolamine. Before assembling the measurement cell, the samples were briefly rinsed with MilliQ.

Membrane assembly The ITO slides were immersed for 30 min in a 40 mM Ni_2SO_4 solution (pH 5.5, 50 mM acetate buffer). The excess Ni was removed by brief rinsing with the same acetate buffer without Ni. Immobilization of CcO to the Ni-chelated NTA surface was performed in a solution of 100 nM CcO in detergent containing phosphate buffer (K_2HPO_4 0.1 M, KCl 0.05 M, pH 8, 0.1 % DDM).^[207] Biobeads (SM-2, mesh 20-50, BIO RAD Lab. Inc.) were added to the lipid detergent containing phosphate buffer (K_2HPO_4 0.1 M, KCl 0.05 M, pH 8, DiPhyPC 0.05 mg/ml, 0.1% DDM) to remove the detergent and to form a lipid bilayer.

EIS measurements Electrochemical measurements were taken in a three-electrode configuration where the ITO slide was used as the working, a self-made Ag/AgCl (sat. KCL) as the reference, and a platinum wire as the counter electrode. Electrochemical impedance measurements were performed using an Autolab instrument (PGSTAT302; Eco Chemie, Utrecht, Netherlands) equipped with a FRA2 module for frequency response analysis, an ECD-module amplifier for low currents and a SCAN-GEN module for analog potential scanning. Spectra were recorded in the frequency range from 100 kHz to 3 mHz using an amplitude of 10 mV. Resulting spectra were analyzed by complex nonlinear fitting of the data to a model circuit in Zview (Version 2.6, Scribner Associates, Southern Pines, NC).

8 Conclusion and Outlook

The work presented here demonstrates the multiple possibilities of employing functional hydrogels. Their properties, like the degree of swelling, the mesh size and interaction with biomolecules, were thoroughly investigated to understand the experimental results and to adapt the functionalization protocols. This enables furthermore the comparison with other materials used in the respective area of application. Various implementations of the hydrogels were achieved, from usage as sensor matrix or biomimetic support of an artificial biomembrane to biocompatible coatings for medical purpose. The success is based on the synthesis of polymers that allow for further functionalization and can hence be adapted to the needs of the field of application.

The hydrogel investigated and employed primarily in this thesis was prepared by free radical polymerization of the functional monomer methacrylic acid, NIPAAm and the UV-crosslinker MABP. The obtained terpolymer was subsequently coated on the desired surface and crosslinked to form the hydrogel.

It was possible to synthesize the terpolymer in large batch sizes, which provides the same polymer for a set of different experiments. The molecular weight and weight distribution was highly reproducible among the batches, just as the chemical composition. The ratio between the monomers in the polymer was determined by comprehensive NMR studies and confirmed by XPS measurements of the prepared films. The results led to the correction of ratios stated earlier. Additionally, the NMR experiments revealed an interaction between the methacrylic acid proton and the NIPAAm amide, which was responsible for previous errors. To functionalize the hydrogel, a library of active ester precursors was synthesized and successfully applied. The covalent attachment of proteins inside the network was enabled by hydrophilic and charged active esters. Their higher efficiency compared to less hydrophilic is due to charge attraction between the active ester and the protein and the providing of a suitable environment for the hydrophilic proteins.

The optical characterization of thin hydrogel films was preformed by cLRSP and SPR/OWS. The spectroscopy of cLRSP was newly developed to reliably investi-

gate films with a thickness below the limit of guiding waves. Additionally, it is possible to measure the diffusion of proteins into the gel, taking benefit from the different penetration depths of the two plasmons. By using SPR/OWS, it is possible to resolve refractive index gradients inside micron-thick films. To interpret the complex spectra, the WKB-approximation was employed to allocate a distance from the metal surface to the refractive index. This method nicely displays the gradient of the refractive index without manual fitting of the spectra and is applicable for artificial step-like gradients as well.

Studying the dynamics of probes diffusing through hydrogel films or the respective transient gels was carried out employing FCS, PCS and SPR/OWS. The probes diffusion behavior measured by FCS enabled the determination of the mesh size, which is large enough for small biomolecules and to study the mechanical properties of the hydrogels. Currently, first steps are done to enhance this method using FRET and to synthesize a library of diffusants. Similar investigations by tracking gold nanoparticles with PCS are launched to obtain complementary information from the relative movement of the scatterers. In addition, a method for probing non fluorescent organic diffusants by SPR/OWS, e.g. for sensor applications was discussed, using PEG as example.

The investigation of the structure and dynamics of the network, which influences the diffusion of the probes, was attempted to perform with FCS on fluorescent labeled gels. As this approach was found to be inherently impossible, μ PCS was introduced to characterize hydrogel films. Beside studying the gels dynamics, μ PCS allows for a more reliable determination of the mesh size of the hydrogel compared to value deduced from the tracer diffusion measured by FCS.

These thorough investigations led to a better understanding of the properties of the hydrogel and paved the way for applications in sensing and medical coatings. The hydrogel network is employed as biosensor matrix for the affinity binding of proteins. The immobilization of the binding moiety was achieved by a charge attracting active ester. Both the functionalization and the binding event were quantitatively monitored *in situ* using SPR/OWS as signal transducer. Besides, the gel showed low unspecific adsorption from blood serum. Hence, combining SPR/OWS with a hydrogel network as platform is a promising approach for biosensor applications.

The investigation of interactions with biomaterials was carried on below and above LCST, i.e. in the swollen and collapsed state. The effect of hydrogel films on cells was studied on coated petri-dishes and the adsorption of proteins was measured by ToF-SIMS. Contrary to literature, the gels showed neither prolifer-

ation of cells nor adsorption of proteins in the collapsed state. Apparently, the interaction with biomaterials is not solely determined by the surface chemistry of a coating but also by structural parameters like surface coverage. These properties render the hydrogel a highly promising candidate for employment in soft tissue implants. Their development towards the actual coating of implants is currently intensely expedited. Moreover, these results support the application in biosensing.

The hydrogel was adapted to the needs of a cushion for artificial biomembranes as well. Introducing a higher degree of functionality facilitates establishing a protein-tethered bilayer lipid membrane on ITO, a chemically susceptible surface of high interest. Furthermore, this hydrogel paves the way to enhance the research on biomembranes and membrane attached proteins by mimicking cytosol and cytoskeleton.

Hence, the present thesis encompasses the whole development of functional hydrogels from design and synthesis, via characterization and adaptation to their application in surgery and biosensing.

Abbreviations

Å	Ångström, 1 Å = 0,1 nm
ac	Alternating current
AFM	Atomic force microscopy
AIBN	Azo-bis-isobutyronitrile
AO	Acetoneoxime
ATR	Attenuated total internal reflection
a.u.	Arbitrary unit
BLM	Bilayer lipid membrane
Boc	<i>tert.</i> -Butyl-carbonate
BSA	Bovine serum albumin
ca	Contact angle
CcO	Cytochrome C oxidase
CD ₂ Cl ₂	Dichloromethane-d2
CDCl ₃	Chloroform-d1
CD ₃ CN	Acetonitrile-d3
cLRSP	Coupled long range surface plasmon
CMC	Critical micelle concentration
cyt c	Cytochrome C
d	Days
Da	Dalton, 1 Da = 1 g/mol
DC	Direct current
DCM	Dichloromethane
DDM	n-Dodecyl-β-D-maltoside
DMAP	4-(Dimethylamino)pyridine
DMF	Dimethylformamide
DMPS	<i>p</i> -Hydroxyphenyldimethylsulfonium methylsulfate
DMSO	Dimethyl sulfoxide
DNA	Deoxyribonucleic acid
D ₂ O	Deuterium oxide, deuterated water
DPhyPC	Diphytanyl-phosphatidylcholin

EDC	1-Ethyl-3-(3-dimethylaminopropyl)carbodiimide
EIS	Electrochemical impedance spectroscopy
eq	Equivalent
F	Farad
FCS	Fluorescence correlation spectroscopy
FD-MS	Field desorption mass spectroscopy
FMOC	Fluorenylmethoxycarbonyl
FRET	Fluorescence resonance energy transfer
g	Gram
GPC	Gel permeation chromatography, also size exclusion chromatography
h	Hour
HEAm	<i>N</i> -(2-Hydroxyethyl)acrylamide
HSA	Human serum albumin
Hz	Hertz
IgG	Immunoglobulin G
IgG-b	Biotinylated IgG
ITO	Indium tin oxide
k	Kilo
L	Liter
LB	Langmuir Blodgett
LCST	Lower critical solution temperature
LRSP	Long range surface plasmon
Lys	Lysozyme
M	Mega
MAA	Methacrylic acid
MABP	4-Benzoylphenyl methacrylate
mbar	Millibar
MeOH	Methanol
μ	Micro
mg	Milligram
MilliQ	Ultra pure water > 18.2 MΩcm ²
min	Minute
mL	Milliliter
mm	Millimeter
mmol	Millimole
M _n	Number average of the molecular weight, $M_n = \frac{\sum N_x M_x}{\sum N_x}$

M_w	Weight average of the molecular weight, $M_w = \frac{\sum N_x M_x^2}{\sum N_x M_x}$
MWCO	Molecular weight cut off
NA	Neutravidine
NBS	<i>N</i> -Bromosuccinimide
NHS	<i>N</i> -Hydroxysuccinimide
NIPAAm	<i>N</i> -Isopropylacrylamide
nm	Nanometer
NMR	Nuclear Magnetic Resonance multiplicity: s singlet, d duplet, t triplet, q quartet, m multiplet, b broad
NTA	Nitrilotriacetic acid
NTAAm	5-Acrylamido-1-carboxypentyl-iminodiacetate
Ω	Ohm
OWFS	Optical waveguide mode fluorescence spectroscopy
OWS	Optical waveguide mode spectroscopy
PBS	Phosphate buffered saline
PCA	Principle component analysis
PCS	Photo correlation spectroscopy
Pd/C	Palladium on char coal
PDI	Polydispersity Index $PDI = \frac{M_w}{M_n}$
PE	Polyethylene
PEG	Polyethylene glycol
PFP	Pentafluorophenol
HEMA	Polyhydroxyethyl methacrylate
PNIPAAm	Poly- <i>N</i> -isopropylacrylamide
ppm	Parts per million
ptBLM	Protein tethered bilayer lipid membrane
QCM	Quarz cristal microbalance
R_f	Retention factor
R_h	Hydrodynamic radius
Rh6G	Rhodamine 6G
Rms	Mean square roughness
rpm	Rotations per minute
RT	Room temperature
s	Second
SA	Self assembly
SAM	Self assembled monolayer
SP	Surface plasmon

SPFS	Surface plasmon fluorescence spectroscopy
SPR	Surface plasmon resonance
tBLM	Tethered bilayer lipid membrane
TEM	Transmission electron microscope
TFA	Trifluoroacetic acid
TFPS	Sodium <i>p</i> -tetrafluorophenol sulfonate
THF	Tetrahydrofurane
TIR	Total internal reflection
TLC	Thin layer chromatography
TMS	Trimethylsilane
ToF-SIMS	Time of flight secondary ion mass spectroscopy
UCST	Upper critical solution temperature
UV	Ultra violet, $\lambda = 400 - 10 \text{ nm}$
W	Watt
WKB	Wentzel-Kramers-Brillouin
XPS	X-ray photoelectron spectroscopy

Bibliography

- [1] Holm, C., Kremer, K. T., and Vilgis, A., *Physikalische Blätter* **1998**, 54, 1013–1016, Polyelektrolyte.
- [2] Machacek, O., *US-Patent 3985593* **1976**, Water gel explosives.
- [3] Wichterle, O., *US-Patent 3408429* **1968**, Method for centrifugal casting a contact lens.
- [4] Buchholz, F. L., *Chemtech* **1994**, 24(9), 38–43, Keeping Dry with Superabsorbent Polymers.
- [5] Rawlings, A. V. and Watkinson, A., *US-Patent 5554366* **1996**, Skin care method and composition.
- [6] Barry, E. F. and Grob, R. L., *Wiley-Interscience* **2007**, Columns for gas chromatography: performance and selection.
- [7] Tanaka, T., *Polymer* **1979**, 20(11), 1404–1412, Phase-Transitions in Gels and a Single Polymer.
- [8] Qiu, Y. and Park, K., *Advanced Drug Delivery Reviews* **2001**, 53(3), 321–339, Environment-sensitive hydrogels for drug delivery.
- [9] Hoffman, A. S., *Advanced Drug Delivery Reviews* **2002**, 54(1), 3–12, Hydrogels for biomedical applications.
- [10] Peppas, N. A., Hilt, J. Z., Khademhosseini, A., and Langer, R., *Advanced Materials* **2006**, 18(11), 1345–1360, Hydrogels in biology and medicine: From molecular principles to bionanotechnology.
- [11] Pennadam, S. S., Firman, K., Alexander, C., and Gdrecki, D. C., *Journal of Nanobiotechnology* **2004**, 2(1), 8, Protein-polymer nano-machines. Towards synthetic control of biological processes.

- [12] Bromberg, L. E. and Ron, E. S., *Advanced Drug Delivery Reviews* **1998**, 31(3), 197–221, Temperature-responsive gels and thermogelling polymer matrices for protein and peptide delivery.
- [13] Bütün, V., Liu, S., Weaver, J. V. M., Bories-Azeau, X., Cai, Y., and Armes, S. P., *Reactive & Functional Polymers* **2006**, 66(1), 157–165, A brief review of 'schizophrenic' block copolymers.
- [14] Zhong, X., Wang, Y. X., and Wang, S. C., *Chemical Engineering Science* **1996**, 51(12), 3235–3239, Pressure dependence of the volume phase-transition of temperature-sensitive gels.
- [15] Firestone, B. A. and Siegel, R. A., *Journal of Applied Polymer Science* **1991**, 43(5), 901–914, Kinetics and Mechanisms of Water Sorption in Hydrophobic, Ionizable Copolymer Gels.
- [16] Brannon-Peppas, L. and Peppas, N. A., *Biomaterials* **1990**, 11(9), 635–644, Dynamic and Equilibrium Swelling Behavior of Ph-Sensitive Hydrogels Containing 2-Hydroxyethyl Methacrylate.
- [17] Khare, A. R. and Peppas, N. A., *Journal of Biomaterials Science-Polymer Edition* **1993**, 4(3), 275–289, Release Behavior of Bioactive Agents from Ph-Sensitive Hydrogels.
- [18] Siegel, R. A., Falamarzian, M., Firestone, B. A., and Moxley, B. C., *Journal of Controlled Release* **1988**, 8(2), 179–182, Ph-Controlled Release from Hydrophobic Poly-Electrolyte Copolymer Hydrogels.
- [19] Patel, V. R. and Amiji, M. M., *Pharmaceutical Research* **1996**, 13(4), 588–593, Preparation and characterization of freeze-dried chitosan-poly(ethylene oxide) hydrogels for site-specific antibiotic delivery in the stomach.
- [20] Mamada, A., Tanaka, T., Kungwachakun, D., and Irie, M., *Macromolecules* **1990**, 23(5), 1517–1519, Photoinduced Phase-Transition of Gels.
- [21] Suzuki, A. and Tanaka, T., *Nature* **1990**, 346(6282), 345–347, Phase-Transition in Polymer Gels Induced by Visible-Light.
- [22] Tanaka, T., Nishio, I., Sun, S. T., and Uenonishio, S., *Science* **1982**, 218(4571), 467–469, Collapse of Gels in an Electric-Field.

- [23] Gong, J. P., Nitta, T., and Osada, Y., *Journal of Physical Chemistry* **1994**, 98(38), 9583–9587, Electrokinetic Modeling of the Contractile Phenomena of Polyelectrolyte Gels - One-Dimensional Capillary Model.
- [24] Shiga, T., Hirose, Y., Okada, A., and Kurauchi, T., *Journal of Applied Polymer Science* **1992**, 46(4), 635–640, Electric Field-Associated Deformation of Polyelectrolyte Gel near a Phase-Transition Point.
- [25] Sawahata, K., Hara, M., Yasunaga, H., and Osada, Y., *Journal of Controlled Release* **1990**, 14(3), 253–262, Electrically Controlled Drug Delivery System Using Polyelectrolyte Gels.
- [26] Kajiwarra, K. and Rossmurphy, S. B., *Nature* **1992**, 355(6357), 208–209, Polymers - Synthetic Gels on the Move.
- [27] Osada, Y., Okuzaki, H., and Hori, H., *Nature* **1992**, 355(6357), 242–244, A Polymer Gel with Electrically Driven Motility.
- [28] Miyata, T., Asami, N., and Uragami, T., *Nature* **1999**, 399(6738), 766–769, A reversibly antigen-responsive hydrogel.
- [29] Lee, S. J. and Park, K., *Journal of Molecular Recognition* **1996**, 9(5-6), 549–557, Synthesis and characterization of sol-gel phase-reversible hydrogels sensitive to glucose.
- [30] Obaidat, A. A. and Park, K., *Pharmaceutical Research* **1996**, 13(7), 989–995, Characterization of glucose dependent gel-sol phase transition of the polymeric glucose-concanavalin A hydrogel system.
- [31] Kim, J. J. and Park, K., *Journal of Controlled Release* **2001**, 77(1-2), 39–47, Modulated insulin delivery from glucose-sensitive hydrogel dosage forms.
- [32] Gauthier, M. A., Gibson, M. I., and Klok, H. A., *Angewandte Chemie-International Edition* **2009**, 48(1), 48–58, Synthesis of Functional Polymers by Post-Polymerization Modification.
- [33] Fuchs, A. D. and Tiller, J. C., *Angewandte Chemie-International Edition* **2006**, 45(40), 6759–6762, Contact-active antimicrobial coatings derived from aqueous suspensions.

- [34] Zolotukhin, M. G., Colquhoun, H. M., Sestiaa, L. G., Rueda, D. R., and Flot, D., *Macromolecules* **2003**, 36(13), 4766–4771, One-pot synthesis and characterization of soluble poly(aryl ether-ketone)s having pendant carboxyl groups.
- [35] Schneider, B. H., Dickinson, E. L., Vach, M. D., Hoiyer, J. V., and Howard, L. V., *Biosensors & Bioelectronics* **2000**, 15(1-2), 13–22, Highly sensitive optical chip immunoassays in human serum.
- [36] Vaisocherova, H., Yang, W., Zhang, Z., Cao, Z. Q., Cheng, G., Piliarik, M., Homola, J., and Jiang, S. Y., *Analytical Chemistry* **2008**, 80(20), 7894–7901, Ultralow fouling and functionalizable surface chemistry based on a zwitterionic polymer enabling sensitive and specific protein detection in undiluted blood plasma.
- [37] Wark, A. W., Lee, H. J., and Corn, R. M., *Analytical Chemistry* **2005**, 77(13), 3904–3907, Long-range surface plasmon resonance imaging for bioaffinity sensors.
- [38] Lakhiari, H., Okano, T., Nurdin, N., Luthi, C., Descouts, P., Muller, D., and Jozefonvicz, J., *Biochimica Et Biophysica Acta-General Subjects* **1998**, 1379(3), 303–313, Temperature-responsive size-exclusion chromatography using poly(N-isopropylacrylamide) grafted silica.
- [39] Kanazawa, H., Yamamoto, K., Matsushima, Y., Takai, N., Kikuchi, A., Sakurai, Y., and Okano, T., *Analytical Chemistry* **1996**, 68(1), 100–105, Temperature-responsive chromatography using poly(N-isopropylacrylamide)-modified silica.
- [40] Gumusderelioglu, M. and Turkoglu, H., *Biomaterials* **2002**, 23(19), 3927–3935, Biomodification of non-woven polyester fabrics by insulin and RGD for use in serum-free cultivation of tissue cells.
- [41] Bhattacharya, S., Eckert, F., Boyko, V., and Pich, A., *Small* **2007**, 3(4), 650–657, Temperature-, pH-, and magnetic-field-sensitive hybrid microgels.
- [42] Xulu, P. M., Filipcsei, G., and Zrinyi, M., *Macromolecules* **2000**, 33(5), 1716–1719, Preparation and responsive properties of magnetically soft poly(N-isopropylacrylamide) gels.
- [43] Schild, H. G., *Progress in Polymer Science* **1992**, 17(2), 163–249, Poly (N-Isopropylacrylamide) - Experiment, Theory and Application.

- [44] Hirotsu, S., Hirokawa, Y., and Tanaka, T., *Journal of Chemical Physics* **1987**, *87*(2), 1392–1395, Volume-Phase Transitions of Ionized N-Isopropylacrylamide Gels.
- [45] Yu, H. and Grainger, D. W., *Journal of Applied Polymer Science* **1993**, *49*(9), 1553–1563, Thermosensitive Swelling Behavior in Cross-Linked N-Isopropylacrylamide Networks - Cationic, Anionic, and Ampholytic Hydrogels.
- [46] Kuckling, D., Harmon, M. E., and Frank, C. W., *Macromolecules* **2002**, *35*(16), 6377–6383, Photo-cross-linkable PNIPAAm copolymers. 1. Synthesis and characterization of constrained temperature-responsive hydrogel layers.
- [47] Harmon, M. E., Kuckling, D., and Frank, C. W., *Macromolecules* **2003**, *36*(1), 162–172, Photo-cross-linkable PNIPAAm copolymers. 2. Effects of constraint on temperature and pH-responsive hydrogel layers.
- [48] Harmon, M. E., Kuckling, D., Pareek, P., and Frank, C. W., *Langmuir* **2003**, *19*(26), 10947–10956, Photo-cross-linkable PNIPAAm copolymers. 4. Effects of copolymerization and cross-linking on the volume-phase transition in constrained hydrogel layers.
- [49] de Bolster, M. W. G., Cammack, R., Coucouvanis, D. R., Reedijk, J., and Veeger, C., *Pure and Applied Chemistry* **1997**, *69*, 1251–1303, Glossary of terms used in bioinorganic chemistry.
- [50] Keizer, H. M., Dorvel, B. R., Andersson, M., Fine, D., Price, R. B., Long, J. R., Dodabalapur, A., Koper, I., Knoll, W., Anderson, P. A. V., and Duran, R. S., *ChemBiochem* **2007**, *8*(11), 1246–1250, Functional ion channels in tethered bilayer membranes - Implications for biosensors.
- [51] Friedrich, M. G., Plum, M. A., Santonicola, M. G., Kirste, V. U., Knoll, W., Ludwig, B., and Naumann, R. L. C., *Biophysical Journal* **2008**, *95*(3), 1500–1510, In situ monitoring of the catalytic activity of cytochrome c oxidase in a biomimetic architecture.
- [52] Anderson, J. M., *Annual Review of Materials Research* **2001**, *31*, 81–110, Biological responses to materials.
- [53] Gong, P. and Grainger, D. W., *Methods in Molecular Biology* **2007**, *381*, 59–92, Nonfouling surfaces - A review of principles and applications for Microarray capture assay designs.

- [54] Pendyala, L., Jabara, R., Robinson, K., and Chronos, N., *Journal of Interventional Cardiology* **2009**, 22(1), 37–48, Passive and Active Polymer Coatings for Intracoronary Stents: Novel Devices to Promote Arterial Healing.
- [55] Grinevich, A., Bacakova, L., Choukourov, A., Boldyryeva, H., Pihosh, Y., Slavinska, D., Noskova, L., Skuciova, M., Lisa, V., and Biedermanl, H., *Journal of Biomedical Materials Research Part A* **2009**, 88A(4), 952–966, Nanocomposite Ti/hydrocarbon plasma polymer films from reactive magnetron sputtering as growth support for osteoblast-like and endothelial cells.
- [56] Cole, M. A., Voelcker, N. H., Thissen, H., and Griesser, H. J., *Biomaterials* **2009**, 30(9), 1827–1850, Stimuli-responsive interfaces and systems for the control of protein-surface and cell-surface interactions.
- [57] Ratner, B. D., Hoffman, A. S., Schoen, F. J., and Lemons, J. E., *Academic press* **2004**, Biomaterials science: an introduction to materials in medicine.
- [58] Dostálek, J., Roskamp, R. F., and Knoll, W., *Sensors and Actuators B* **2009**, 139(1), 9–12, Coupled long range surface plasmons for the investigation of thin films and interfaces.
- [59] Gianneli, M., Beines, P. W., Roskamp, R. F., Koynov, K., Fytas, G., and Knoll, W., *Journal of Physical Chemistry C* **2007**, 111(35), 13205–13211, Local and global dynamics of transient polymer networks and swollen gels anchored on solid surfaces.
- [60] Gianneli, M., Roskamp, R. F., Jonas, U., Loppinet, B., Fytas, G., and Knoll, W., *Soft Matter* **2008**, 4(7), 1443–1447, Dynamics of swollen gel layers anchored to solid surfaces.
- [61] Aulasevich, A., Roskamp, R. F., Jonas, U., Menges, B., Dostálek, J., and Knoll, W., *Macromolecular Rapid Communications* **2009**, 30(9), 872–877, Optical Waveguide Spectroscopy for the Investigation of Protein-Functionalized Hydrogel Films.
- [62] Raether, H., *Academic Press, New York* **1977**, 9, 145, Physics of Thin Films, ed. H.G. F.M. H.R.
- [63] Raether, H., *Springer, Berlin* **1988**, Surface Plasmons on Smooth and Rough Surfaces and on Gratings.

-
- [64] Knoll, W., *Mrs Bulletin* **1991**, 16(7), 29–39, Optical Characterization of Organic Thin-Films and Interfaces with Evanescent Waves.
- [65] Kretschmann, E. and Raether, H., *Zeitschrift Für Naturforschung Part A-Astrophysik Physik Und Physikalische Chemie* **1968**, A 23(12), 2135–2136, Radiative Decay of Non Radiative Surface Plasmons Excited by Light.
- [66] Kovacs, G., *John Wiley & Sons, New York* **1982**, Electromagnetic Surface Modes.
- [67] Pochi, Y., *Wiley* **1988**, Optical waves in layered media.
- [68] Andrews, D. L. and Gaburro, Z., *Springer* **2007**, Frontiers in surface nanophotonics: principles and applications.
- [69] Karthe, W. and Müller, R., *Akademische Verlagsgesellschaft Geest & Portig Leipzig, Germany* **1991**, Integrierte Optik.
- [70] Smith, R. E. and Houde-Walter, S. N., *Journal of the Optical Society of America A-Optics Image Science and Vision* **1995**, 12(4), 715–724, Leaky Guiding in Nontransparent Wave-Guides.
- [71] Tien, P. K., *Reviews of Modern Physics* **1977**, 49(2), 361–420, Integrated-Optics and New Wave Phenomena in Optical-Waveguides.
- [72] Filippidi, E., Michailidou, V., Loppinet, B., Ruhe, J., and Fytas, G., *Langmuir* **2007**, 23(9), 5139–5142, Brownian diffusion close to a polymer brush.
- [73] Furukawa, H., Horie, K., Nozaki, R., and Okada, M., *Physical Review E* **2003**, 68(3), Swelling-induced modulation of static and dynamic fluctuations in polyacrylamide gels observed by scanning microscopic light scattering.
- [74] Tu, H. L., Hong, L., Anthony, S. M., Braun, P. V., and Granick, S., *Langmuir* **2007**, 23(5), 2322–2325, Brush-sheathed particles diffusing at brush-coated surfaces in the thermally responsive PNIPAAm system.
- [75] Wang, W., Zhang, C. F., Wang, S. Q., and Zhao, J., *Macromolecules* **2007**, 40(26), 9564–9569, Diffusion of single polyelectrolytes on the surface of poly (N-isopropylacrylamide) brushes.
- [76] Rigler, R. and Elson, E. S., *Springer Berlin* **2001**, Fluorescence correlation spectroscopy: theory and applications.

- [77] Geissler, E., *Oxford: Oxford University Press* **1993**, In: Brown W, Dynamic light scattering. The method and some applications.
- [78] Kroeger, A., Belack, J., Larsen, A., Fytas, G., and Wegner, G., *Macromolecules* **2006**, 39(20), 7098–7106, Supramolecular structures in aqueous solutions of rigid polyelectrolytes with monovalent and divalent counterions.
- [79] Briggs, D., *Cambridge: Cambridge University Press* **1998**, Surface analysis of polymers by XPS and static SIMS.
- [80] Chu, C. L., Wang, R. M., Hu, T., Yin, L. H., Pu, Y. P., Lin, P. H., Dong, Y. S., Guo, C., Chung, C. Y., Yeung, K. W. K., and Chu, P. K., *Journal of Materials Science-Materials in Medicine* **2009**, 20(1), 223–228, XPS and biocompatibility studies of titania film on anodized NiTi shape memory alloy.
- [81] Briggs, D. and Vickerman, J. C., *ToF-SIMS: surface analysis by mass spectrometry*; 2001.
- [82] Castner, D. G., *Nature* **2003**, 422(6928), 129–130, Surface science - View from the edge.
- [83] Cornell, B. A., BraachMaksvytis, V. L. B., King, L. G., Osman, P. D. J., Rague, B., Wieczorek, L., and Pace, R. J., *Nature* **1997**, 387(6633), 580–583, A biosensor that uses ion-channel switches.
- [84] Sackmann, E., *Science* **1996**, 271(5245), 43–48, Supported membranes: Scientific and practical applications.
- [85] Drexler, J., *PhD Thesis, Regensburg, Germany* **2003**, Herstellung porenüberspannender Lipidmembranen auf Basis poröser Aluminate und deren Charakterisierung mittels elektrischer Impedanzspektroskopie.
- [86] Schmickler, W., *Vieweg, Braunschweig* **1996**, Grundlagen der Elektrochemie.
- [87] Ista, L. K., Mendez, S., Perez-Luna, V. H., and Lopez, G. P., *Langmuir* **2001**, 17(9), 2552–2555, Synthesis of poly(N-isopropylacrylamide) on initiator-modified self-assembled monolayers.
- [88] Cole, M. A., Jasieniak, M., Voelcker, N. H., Thissen, H., Horn, R., and Griesser, H. J., *Proceedings of the SPIE - The International Society for Optical Engineering* **2006**, page 641606 (10 pp.), Switchable surface coatings for control over protein adsorption.

- [89] Mizutani, A., Kikuchi, A., Yamato, M., Kanazawa, H., and Okano, T., *Bio-materials* **2008**, 29(13), 2073–2081, Preparation of thermoresponsive polymer brush surfaces and their interaction with cells.
- [90] Alarcon, C. D. H., Farhan, T., Osborne, V. L., Huck, W. T. S., and Alexander, C., *Journal of Materials Chemistry* **2005**, 15(21), 2089–2094, Bioadhesion at micro-patterned stimuli-responsive polymer brushes.
- [91] Huber, D. L., Manginell, R. P., Samara, M. A., Kim, B. I., and Bunker, B. C., *Science* **2003**, 301(5631), 352–354, Programmed adsorption and release of proteins in a microfluidic device.
- [92] Balamurugan, S., Mendez, S., Balamurugan, S. S., O'Brien, M. J., and Lopez, G. P., *Langmuir* **2003**, 19(7), 2545–2549, Thermal response of poly(N-isopropylacrylamide) brushes probed by surface plasmon resonance.
- [93] Cunliffe, D., Alarcon, C. D., Peters, V., Smith, J. R., and Alexander, C., *Langmuir* **2003**, 19(7), 2888–2899, Thermoresponsive surface-grafted poly(N-isopropylacrylamide) copolymers: Effect of phase transitions on protein and bacterial attachment.
- [94] Yamato, M. and Okano, T., *materialstoday* **2004**, 7(5), 42–47, Cell Sheet Engineering.
- [95] Okano, T., Yamada, N., Sakai, H., and Sakurai, Y., *Journal of Biomedical Materials Research* **1993**, 27(10), 1243–1251, A Novel Recovery-System for Cultured-Cells Using Plasma-Treated Polystyrene Dishes Grafted with Poly(N-Isopropylacrylamide).
- [96] Wang, Y. B., Cheng, X. H., Hanein, Y., Shastry, A., Denton, D. D., Ratner, B. D., and Bohringer, K. F., *Boston Transducers'03: Digest of Technical Papers* **2003**, 1/2, 979–982, Selective attachment of multiple cell types on thermally responsive polymer.
- [97] Xuanhong, C., Canavan, H. E., Graham, D. J., Castner, D. G., and Ratner, B. D., *Biointerphases Journal* **2006**, 1(1), 61–72, Temperature dependent activity and structure of adsorbed proteins on plasma polymerized N-isopropyl acrylamide.
- [98] Cheng, X. H., Wang, Y. B., Hanein, Y., Bohringer, K. F., and Ratner, B. D., *Journal of Biomedical Materials Research Part A* **2004**, 70A(2), 159–

168, Novel cell patterning using microheater-controlled thermoresponsive plasma films.

- [99] Beines, P. W., Klosterkamp, I., Menges, B., Jonas, U., and Knoll, W., *Langmuir* **2007**, 23(4), 2231–2238, Responsive thin hydrogel layers from photocross-linkable poly(N-isopropylacrylamide) terpolymers.
- [100] Prucker, O., Naumann, C. A., Ruhe, J., Knoll, W., and Frank, C. W., *Journal of the American Chemical Society* **1999**, 121(38), 8766–8770, Photochemical attachment of polymer films to solid surfaces via monolayers of benzophenone derivatives.
- [101] Toomey, R., Freidank, D., and R uhe, J., *Macromolecules* **2004**, 37(3), 882–887, Swelling behavior of thin, surface-attached polymer networks.
- [102] Xue, W., Hamley, I. W., and Huglin, M. B., *Polymer* **2002**, 43(19), 5181–5186, Rapid swelling and deswelling of thermoreversible hydrophobically modified poly(N-isopropylacrylamide) hydrogels prepared by freezing polymerisation.
- [103] Anac, I., Aulasevich, A., Junk, M. J. N., Jakubowicz, P., Roskamp, R. F., Menges, B., Jonas, U., and Knoll, W., *in preparation* **2009**, Temperature dependent swelling behavior of thin Poly(N-isopropylacrylamide) copolymer gel layers in ethanol-water mixtures.
- [104] Li, H. and McGall, G., *US-Patent 0234788* **2004**, Photoactivateable silane compounds and methods for their synthesis and use.
- [105] Kuckling, D., Hoffmann, J., Plotner, M., Ferse, D., Kretschmer, K., Adler, H. J. P., Arndt, K. F., and Reichelt, R., *Polymer* **2003**, 44(16), 4455–4462, Photo cross-linkable poly(N-isopropylacrylamide) copolymers III: microfabricated temperature responsive hydrogels.
- [106] Junk, M. J. N., *Diploma Thesis, Mainz, Germany* **2007**, Struktur und Strukturierung von Photovernetzbaeren, Thermoresponsiven Hydrogelsystemen.
- [107] Metz, N. and Theato, P., *European Polymer Journal* **2007**, 43(4), 1202–1209, Controlled synthesis of poly(acetone oxime acrylate) as a new reactive polymer: Stimuli-responsive reactive copolymers.

- [108] Gee, K. R., Archer, E. A., and Kang, H. C., *Tetrahedron Letters* **1999**, 40(8), 1471–1474, 4-Sulfotetrafluorophenyl (STP) esters: New water-soluble amine-reactive reagents for labeling biomolecules.
- [109] Nagai, K., Ohashi, T., Kaneko, R., and Taniguchi, T., *Colloids and Surfaces a-Physicochemical and Engineering Aspects* **1999**, 153(1-3), 133–136, Preparation and applications of polymeric microspheres having active ester groups.
- [110] Beines, P. W., *PhD Thesis, Mainz, Germany* **2007**, Synthese und Charakterisierung einer Hydrogelmatrix für die Multianalyt-Sensorik.
- [111] Allen, N. S., Mallon, D., Timms, A., Green, A. W., and Catalina, F., *European Polymer Journal* **1993**, 29(4), 533–538, Synthesis and Spectroscopic Properties of Novel Cinnamate Derivatives of Benzophenone - Photocuring Activity Versus Photodimerization.
- [112] Junk, M. J. N., Jonas, U., and Hinderberger, D., *Small* **2008**, 4(9), 1485–1493, EPR spectroscopy reveals nanoinhomogeneities in the structure and reactivity of thermoresponsive hydrogels.
- [113] Briggs, D. and Beamson, G., *Wiley Chichester* **1992**, High resolution XPS of organic polymers: The scienta ESCA300 database.
- [114] Hirschmugl, C. J., *Surface Science* **2002**, 500(1-3), 577–604, Frontiers in infrared spectroscopy at surfaces and interfaces.
- [115] Arwin, H., *Thin Solid Films* **2000**, 377, 48–56, Ellipsometry on thin organic layers of biological interest: characterization and applications.
- [116] Knoll, W., *Annual Review of Physical Chemistry* **1998**, 49, 569–638, Interfaces and thin films as seen by bound electromagnetic waves.
- [117] Jacobsen, V., Menges, B., Förch, R., Mittler, S., and Knoll, W., *Thin Solid Films* **2002**, 409(2), 185–193, In-situ thin film diagnostics using waveguide mode spectroscopy.
- [118] Zacher, T. and Wischerhoff, E., *Langmuir* **2002**, 18(5), 1748–1759, Real-time two-wavelength surface plasmon resonance as a tool for the vertical resolution of binding processes in biosensing hydrogels.
- [119] Peterlinz, K. A. and Georgiadis, R., *Optics Communications* **1996**, 130(4-6), 260–266, Two-color approach for determination of thickness and dielectric constant of thin films using surface plasmon resonance spectroscopy.

- [120] Slavik, R., Homola, J., and Vaisocherova, H., *Measurement Science & Technology* **2006**, 17(4), 932–938, Advanced biosensing using simultaneous excitation of short and long range surface plasmons.
- [121] Dostálek, J., Adam, P., Kvasnicka, P., Telezhnikova, O., and Homola, J., *Optics Letters* **2007**, 32, 2903–2905, Spectroscopy of Bragg-scattered surface plasmons for characterization of thin biomolecular films.
- [122] Xu, F., Persson, B., Lofas, S., and Knoll, W., *Langmuir* **2006**, 22(7), 3352–3357, Surface plasmon optical studies of carboxymethyl dextran brushes versus networks.
- [123] Homola, J., Yee, S. S., and Gauglitz, G., *Sensors and Actuators B-Chemical* **1999**, 54(1-2), 3–15, Surface plasmon resonance sensors: review.
- [124] Nenninger, G. G., Tobiška, P., Homola, J., and Yee, S. S., *Sensors & Actuators: B. Chemical* **2001**, 74(1-3), 145–151, Long-range surface plasmons for high-resolution surface plasmon resonance sensors.
- [125] Kasry, A. and Knoll, W., *Applied Physics Letters* **2006**, 89(10), Long range surface plasmon fluorescence spectroscopy.
- [126] Sarid, D., *Physical Review Letters* **1981**, 47(26), 1927–1930, Long-Range Surface-Plasma Waves on Very Thin Metal-Films.
- [127] Dostálek, J., Kasry, A., and Knoll, W., *Plasmonics* **2007**, 2(3), 97–106, Long range surface plasmons for observation of biomolecular binding events at metallic surfaces.
- [128] Adam, P., Dostálek, J., and Homola, J., *Sensors and Actuators B-Chemical* **2006**, 113(2), 774–781, Multiple surface plasmon spectroscopy for study of biomolecular systems.
- [129] Brazel, C. S. and Peppas, N. A., *Journal of Controlled Release* **1996**, 39(1), 57–64, Pulsatile local delivery of thrombolytic and antithrombotic agents using poly(*N*-isopropylacrylamide-co-methacrylic acid) hydrogels.
- [130] Weisser, M., Thoma, F., Menges, B., Langbein, U., and Mittler-Neher, S., *Optics Communications* **1998**, 153(1-3), 27–31, Fluorescence in ion exchanged BK7 glass slab waveguides and its use for scattering free loss measurements.

- [131] van der Gucht, J., Besseling, N. A. M., Knoben, W., Bouteiller, L., and Stuart, M. A. C., *Physical Review E* **2003**, 67(5), 051106, Brownian particles in supramolecular polymer solutions.
- [132] Lewis, G., Coughlan, D. C., Lane, M. E., and Corrigan, O. I., *Journal of Microencapsulation* **2006**, 23(6), 677–685, Preparation and release of model drugs from thermally sensitive poly(N-isopropylacrylamide) based microspheres.
- [133] Tong, P., Ye, X., Ackerson, B. J., and Fetters, L. J., *Physical Review Letters* **1997**, 79(12), 2363–2366, Sedimentation of colloidal particles through a polymer solution.
- [134] Phillies, G. D. J., *Journal of Physical Chemistry* **1989**, 93(13), 5029–5039, The Hydrodynamic Scaling Model for Polymer Self-Diffusion.
- [135] Lodge, T. P., Rotstein, N. A., and Prager, S., *Advances in Chemical Physics* **1990**, 79, 1–132, Dynamics of Entangled Polymer Liquids - Do Linear-Chains Reptate.
- [136] Lumma, D., Keller, S., Vilgis, T., and Radler, J. O., *Physical Review Letters* **2003**, 90(21), 218301, Dynamics of large semiflexible chains probed by fluorescence correlation spectroscopy.
- [137] Shusterman, R., Alon, S., Gavrinov, T., and Krichevsky, O., *Physical Review Letters* **2004**, 92(4), 048303, Monomer dynamics in double- and single-stranded DNA polymers.
- [138] Sukhishvili, S. A., Chen, Y., Muller, J. D., Gratton, E., Schweizer, K. S., and Granick, S., *Macromolecules* **2002**, 35(5), 1776–1784, Surface diffusion of poly(ethylene glycol).
- [139] Zettl, H., Hafner, W., Boker, A., Schmalz, H., Lanzendorfer, M., Muller, A. H. E., and Krausch, G., *Macromolecules* **2004**, 37(5), 1917–1920, Fluorescence correlation spectroscopy of single dye-labeled polymers in organic solvents.
- [140] Matejicek, P., Podhajecka, K., Humpolickova, J., Uhlik, F., Jelinek, K., Limpouchova, Z., Prochazka, K., and Spirikova, M., *Macromolecules* **2004**, 37(26), 10141–10154, Polyelectrolyte behavior of polystyrene-block-poly(methacrylic acid) micelles in aqueous solutions at low ionic strength.

- [141] Michelman-Ribeiro, A., Boukari, H., Nossal, R., and Horkay, F., *Macromolecules* **2004**, 37(26), 10212–10214, Structural changes in polymer gels probed by fluorescence correlation spectroscopy.
- [142] Best, A., Pakula, T., and Fytas, G., *Macromolecules* **2005**, 38(10), 4539–4541, Segmental dynamics of bulk polymers studied by fluorescence correlation spectroscopy.
- [143] Liu, R. G., Gao, X., Adams, J., and Oppermann, W., *Macromolecules* **2005**, 38(21), 8845–8849, A fluorescence correlation spectroscopy study on the self-diffusion of polystyrene chains in dilute and semidilute solution.
- [144] Kang, K., Gapinski, J., Lettinga, M. P., Buitenhuis, J., Meier, G., Ratajczyk, M., Dhont, J. K. G., and Patkowski, A., *Journal of Chemical Physics* **2005**, 122(4), 044905, Diffusion of spheres in crowded suspensions of rods.
- [145] Jian, T., Anastasiadis, S. H., Semenov, A. N., Fytas, G., Adachi, K., and Kotaka, T., *Macromolecules* **1994**, 27(17), 4762–4773, Dynamics of Composition Fluctuations in Diblock Copolymer Solutions Far from and near to the Ordering Transition.
- [146] Yuan, G. C., Wang, X. H., Han, C. C., and Wu, C., *Macromolecules* **2006**, 39(18), 6207–6209, Reexamination of slow dynamics in semidilute solutions: Temperature and salt effects on semidilute poly(N-isopropylacrylamide) aqueous solutions.
- [147] Wyart, F. B. and de Gennes, P. G., *European Physical Journal E* **2000**, 1(1), 93–97, Viscosity at small scales in polymer melts.
- [148] Langevin, D. and Rondelez, F., *Polymer* **1978**, 19(8), 875–882, Sedimentation of Large Colloidal Particles through Semidilute Polymer-Solutions.
- [149] Horkay, F., Hecht, A. M., and Geissler, E., *Macromolecules* **1994**, 27(7), 1795–1798, Small-Angle Neutron-Scattering in Poly(Vinyl Alcohol) Hydrogels.
- [150] Narita, T., Knaebel, A., Munch, J. P., and Candau, S. J., *Macromolecules* **2001**, 34(23), 8224–8231, Microrheology of poly(vinyl alcohol) aqueous solutions and chemically cross-linked gels.
- [151] Ikkai, F. and Shibayama, M., *Journal of Polymer Science Part B-Polymer Physics* **2005**, 43(6), 617–628, Inhomogeneity control in polymer gels.

- [152] Roskamp, R. F., Brunsen, A., Gianneli, M., Jakubowicz, P., Menges, B., Jonas, U., Fytas, G., and Knoll, W., *Polymer Preprints* **2008**, 49(1), 1018, Hydrogels: Synthesis, Functionalization and Optical Investigation.
- [153] Rucareanu, S., Gandubert, V. J., and Lennox, R. B., *Chemistry of Materials* **2006**, 18(19), 4674–4680, 4-(N,N-dimethylamino)pyridine-protected Au nanoparticles: Versatile precursors for water- and organic-soluble gold nanoparticles.
- [154] Tien, J., Terfort, A., and Whitesides, G. M., *Langmuir* **1997**, 13(20), 5349–5355, Microfabrication through electrostatic self-assembly.
- [155] Ruhemann, S., *Journal of the Chemical Society* **1910**, 97, 2025–2031, Triketohydrindene hydrate.
- [156] Kaiser, E., Colescott, R. L., Bossinger, C. D., and Cook, P. I., *Analytical biochemistry* **1970**, 34(2), 595–598, Color test for detection of free terminal amino groups in the solid-phase synthesis of peptides.
- [157] Kim, H., Ruhm, A., Lurio, L. B., Basu, J. K., Lal, J., Lumma, D., Mochrie, S. G. J., and Sinha, S. K., *Physical Review Letters* **2003**, 90(6), Surface dynamics of polymer films.
- [158] von Meerwall, E., Grigsby, J., Tomich, D., and Vanantwerp, R., *Journal of Polymer Science Part B-Polymer Physics* **1982**, 20(6), 1037–1053, Effect of Chain-End Free-Volume on the Diffusion of Oligomers.
- [159] Callaghan, P. T. and Pinder, D. N., *Macromolecules* **1984**, 17(3), 431–437, Influence of Multiple Length Scales on the Behavior of Polymer Self-Diffusion in the Semidilute Regime.
- [160] Fleischer, G. and Appel, M., *Macromolecules* **1995**, 28(21), 7281–7283, Chain-Length and Temperature-Dependence of the Self-Diffusion of Polyisoprene and Polybutadiene in the Melt.
- [161] Cheng, Y., Prud'homme, R. K., and Thomas, J. L., *Macromolecules* **2002**, 35(21), 8111–8121, Diffusion of mesoscopic probes in aqueous polymer solutions measured by fluorescence recovery after photobleaching.
- [162] Leger, L., Hervet, H., and Rondelez, F., *Macromolecules* **1981**, 14(6), 1732–1738, Reptation in Entangled Polymer-Solutions by Forced Rayleigh Light-Scattering.

- [163] Kim, H. D., Chang, T. Y., Yohanan, J. M., Wang, L., and Yu, H., *Macromolecules* **1986**, 19(11), 2737–2744, Polymer Diffusion in Linear Matrices - Polystyrene in Toluene.
- [164] Antonietti, M., Coutandin, J., Grutter, R., and Sillescu, H., *Macromolecules* **1984**, 17(4), 798–802, Diffusion of Labeled Macromolecules in Molten Polystyrenes Studied by a Holographic Grating Technique.
- [165] Doi, M. and Edwards, S. F., *Oxford University Press, USA* **1986**, The theory of polymer dynamics.
- [166] Verduzco, R., Scruggs, N. R., Sprunt, S., Palffy-Muhoray, P., and Kornfield, J. A., *Soft Matter* **2007**, 3(8), 993–1002, Director dynamics in liquid-crystal physical gels.
- [167] Joosten, J. G. H., Gelade, E. T. F., and Pusey, P. N., *Physical Review A* **1990**, 42(4), 2161–2173, Dynamic Light-Scattering by Nonergodic Media - Brownian Particles Trapped in Polyacrylamide Gels.
- [168] Xue, J. Z., Pine, D. J., Milner, S. T., Wu, X. L., and Chaikin, P. M., *Physical Review A* **1992**, 46(10), 6550–6563, Nonergodicity and Light-Scattering from Polymer Gels.
- [169] Li, J. F., Li, W., Huo, H., Luo, S. Z., and Wu, C., *Macromolecules* **2008**, 41(3), 901–911, Reexamination of the slow mode in semidilute polymer solutions: The effect of solvent quality.
- [170] McGonigle, J. S., Tae, G., Stayton, P. S., Hoffman, A. S., and Scatena, M., *Journal of Biomaterials Science-Polymer Edition* **2008**, 19(8), 1021–1034, Heparin-regulated delivery of osteoprotegerin promotes vascularization of implanted hydrogels.
- [171] Rowley, J. A., Madlambayan, G., and Mooney, D. J., *Biomaterials* **1999**, 20(1), 45–53, Alginate hydrogels as synthetic extracellular matrix materials.
- [172] Knoll, W., Kasry, A., Yu, F., Wang, Y., Brunsen, A., and Dostálek, J., *Journal of Nonlinear Optical Physics & Materials* **2008**, 17(2), 121–129, New concepts with surface plasmons and nano-biointerfaces.
- [173] Derwinska, K., Gheber, L. A., Sauer, U., Schorn, L., and Preininger, C., *Langmuir* **2007**, 23, 10551–10558, Effect of surface parameters on the performance of IgG-arrayed hydrogel chips: A comprehensive study.

- [174] Gianneli, M., *PhD Thesis, Heraklion, Greece* **2008**, Structure and Dynamics of Thin Anchored Hydrogel Layers by Fluorescence Correlation and Photon Correlation Spectroscopy.
- [175] Edwards, D. A., Goldstein, B., and Cohen, D. S., *Journal of Mathematical Biology* **1999**, 39(6), 533–561, Transport effects on surface-volume biological reactions.
- [176] Qureshi, M. H., Yeung, J. C., Wu, S. C., and Wong, S. L., *Journal of Biological Chemistry* **2001**, 276(49), 46422–46428, Development and characterization of a series of soluble tetrameric and monomeric streptavidin muteins with differential biotin binding affinities.
- [177] Schwartz, K. S., Lee, R. K., and Gedde, S. J., *Current Opinion in Ophthalmology* **2006**, 17(2), 181–189, Glaucoma drainage implants: a critical comparison of types.
- [178] Hong, C. H., Arosemena, A., Zurakowski, D., and Ayyala, R. S., *Survey of Ophthalmology* **2005**, 50(1), 48–60, Glaucoma drainage devices: A systematic literature review and current controversies.
- [179] Blake, D. A., Sahiner, N., John, V. T., Clinton, A. D., Galler, K. E., Walsh, M., Arosemena, A., Johnson, P. Y., and Ayyala, R. S., *Journal of Glaucoma* **2006**, 15(4), 291–298, Inhibition of cell proliferation by mitomycin C incorporated into P(HEMA) hydrogels.
- [180] Chifen, A. N., Jenkins, A. T. A., Knoll, W., and Forch, R., *Plasma Processes and Polymers* **2007**, 4(9), 815–822, Adhesion improvement of plasma-polymerized maleic anhydride films on gold using HMDSO/O-2 adhesion layers.
- [181] Haimovich, B., Difazio, L., Katz, D., Zhang, L., Greco, R. S., Dror, Y., and Freeman, A., *Journal of Applied Polymer Science* **1997**, 63(11), 1393–1400, A new method for membrane construction on ePTFE vascular grafts: Effect on surface morphology and platelet adhesion.
- [182] Leckband, D., Sheth, S., and Halperin, A., *Journal of Biomaterials Science-Polymer Edition* **1999**, 10(10), 1125–1147, Grafted poly(ethylene oxide) brushes as nonfouling surface coatings.
- [183] Sydow-Plum, G. and Tabrizian, M., *Materials Science and Technology* **2008**, 24(9), 1127–1143, Review of stent coating strategies: clinical insights.

- [184] Helmus, M. N., Gibbons, D. F., and Cebon, D., *Toxicol Pathol* **2008**, 36(1), 70–80, Biocompatibility: meeting a key functional requirement of next-generation medical devices.
- [185] Kost, J. and Langer, R., *Advanced Drug Delivery Reviews* **2001**, 46(1-3), 125–148, Responsive polymeric delivery systems.
- [186] Meyer, D. E., Shin, B. C., Kong, G. A., Dewhirst, M. W., and Chilkoti, A., *Journal of Controlled Release* **2001**, 74(1-3), 213–224, Drug targeting using thermally responsive polymers and local hyperthermia.
- [187] Yamato, M., Konno, C., Kushida, A., Hirose, M., Utsumi, M., Kikuchi, A., and Okano, T., *Biomaterials* **2000**, 21(10), 981–986, Release of adsorbed fibronectin from temperature-responsive culture surfaces requires cellular activity.
- [188] Canavan, H. E., Graham, D. J., Cheng, X. H., Ratner, B. D., and Castner, D. G., *Langmuir* **2007**, 23(1), 50–56, Comparison of native extracellular matrix with adsorbed protein films using secondary ion mass spectrometry.
- [189] Norde, W. and Gage, D., *Langmuir* **2004**, 20(10), 4162–4167, Interaction of bovine serum albumin and human blood plasma with PEO-tethered surfaces: Influence of PEO chain length, grafting density, and temperature.
- [190] Pasche, S., Voros, J., Griesser, H. J., Spencer, N. D., and Textor, M., *Journal of Physical Chemistry B* **2005**, 109(37), 17545–17552, Effects of ionic strength and surface charge on protein adsorption at PEGylated surfaces.
- [191] Cole, M. A., Thissen, H., Losic, D., and Voelcker, N. H., *Surface Science* **2007**, 601(7), 1716–1725, A new approach to the immobilisation of poly(ethylene oxide) for the reduction of non-specific protein adsorption on conductive substrates.
- [192] Wagner, M. S., McArthur, S. L., Shen, M. C., Horbett, T. A., and Castner, D. G., *Journal of Biomaterials Science-Polymer Edition* **2002**, 13(4), 407–428, Limits of detection for time of flight secondary ion mass spectrometry (ToF-SIMS) and X-ray photoelectron spectroscopy (XPS): detection of low amounts of adsorbed protein.
- [193] Zuwaylif, F. H., *Addison-Wesley Publishing Co., Inc.: Reading, MA* **1980**, General Applied Statistics.

- [194] Miller, J. C. and Miller, J. N., *Ellis Horwood Ltd.: Chichester, U.K.* **1993**, Statistics for Analytical Chemistry.
- [195] Cole, M. A., Jasieniak, M., Thissen, H., Voelcker, N. H., and Griesser, H. J., *Analytical Chemistry* **2009**, online, DOI: 10.1021/ac9009337, Time-of-Flight-Secondary Ion Mass spectrometry Study of the Temperature Dependence of Protein Adsorption onto Poly(N-isopropylacrylamide) Graft Coatings.
- [196] Wagner, M. S. and Castner, D. G., *Langmuir* **2001**, 17(15), 4649–4660, Characterization of adsorbed protein films by time-of-flight secondary ion mass spectrometry with principal component analysis.
- [197] Zhang, J., Pelton, R., and Deng, Y., *Langmuir* **1995**, 11(6), 2301–2302, Temperature-dependent contact angles of water on poly (N-isopropylacrylamide) gels.
- [198] Cullison, J. K., Hawkrige, F. M., Nakashima, N., and Yoshikawa, S., *Langmuir* **1994**, 10(3), 877–882, A Study of Cytochrome-C-Oxidase in Lipid Bilayer – Membranes on Electrode Surfaces.
- [199] Steinem, C., Janshoff, A., Ulrich, W. P., Sieber, M., and Galla, H. J., *Biochimica Et Biophysica Acta-Biomembranes* **1996**, 1279(2), 169–180, Impedance analysis of supported lipid bilayer membranes: A scrutiny of different preparation techniques.
- [200] Wiegand, G., Arribas-Layton, N., Hillebrandt, H., Sackmann, E., and Wagner, P., *Journal of Physical Chemistry B* **2002**, 106(16), 4245–4254, Electrical properties of supported lipid bilayer membranes.
- [201] Horn, C. and Steinem, C., *Biophysical Journal* **2005**, 89(2), 1046–1054, Photocurrents generated by bacteriorhodopsin adsorbed on nano-black lipid membranes.
- [202] Terrettaz, S., Mayer, M., and Vogel, H., *Langmuir* **2003**, 19(14), 5567–5569, Highly electrically insulating tethered lipid bilayers for probing the function of ion channel proteins.
- [203] Schiller, S. M., Naumann, R., Lovejoy, K., Kunz, H., and Knoll, W., *Ange wandte Chemie-International Edition* **2003**, 42(2), 208–+, Archaea analogue thiolipids for tethered bilayer lipid membranes on ultrasmooth gold surfaces.

- [204] Atanasov, V., Knorr, N., Duran, R. S., Ingebrandt, S., Offenhausser, A., Knoll, W., and Koper, I., *Biophysical Journal* **2005**, *89*(3), 1780–1788, Membrane on a chip: A functional tethered lipid bilayer membrane on silicon oxide surfaces.
- [205] Sinner, E. K. and Knoll, W., *Current Opinion in Chemical Biology* **2001**, *5*(6), 705–711, Functional tethered membranes.
- [206] Tamm, L. K. and McConnell, H. M., *Biophysical Journal* **1985**, *47*(1), 105–113, Supported Phospholipid-Bilayers.
- [207] Giess, F., Friedrich, M. G., Heberle, J., Naumann, R. L., and Knoll, W., *Biophysical Journal* **2004**, *87*(5), 3213–3220, The protein-tethered lipid bilayer: A novel mimic of the biological membrane.
- [208] Haussling, L., Knoll, W., Ringsdorf, H., Schmitt, F. J., and Yang, J. L., *Makromolekulare Chemie-Macromolecular Symposia* **1991**, *46*, 145–155, Surface Functionalization and Surface Recognition – Plasmon Optical-Detection of Molecular Recognition at Self Assembled Monolayers.
- [209] Tanaka, M. and Sackmann, E., *Nature* **2005**, *437*(7059), 656–663, Polymer-supported membranes as models of the cell surface.
- [210] Smith, H. L., Jablin, M. S., Vidyasagar, A., Saiz, J., Watkins, E., Toomey, R., Hurd, A. J., and Majewski, J., *Physical Review Letters* **2009**, *102*(22), 228102–1–4, Model Lipid Membranes on a Tunable Polymer Cushion.
- [211] Hillebrandt, H., Wiegand, G., Tanaka, M., and Sackmann, E., *Langmuir* **1999**, *15*(24), 8451–8459, High electric resistance polymer/lipid composite films on indium-tin-oxide electrodes.
- [212] Wagner, M. L. and Tamm, L. K., *Biophysical Journal* **2000**, *79*(3), 1400–1414, Tethered polymer-supported planar lipid bilayers for reconstitution of integral membrane proteins: Silane-polyethyleneglycol-lipid as a cushion and covalent linker.
- [213] Purrucker, O., Fortig, A., Jordan, R., and Tanaka, M., *Chemphyschem* **2004**, *5*(3), 327–335, Supported membranes with well-defined polymer tethers-incorporation of cell receptors.
- [214] Ataka, K., Giess, F., Knoll, W., Naumann, R., Haber-Pohlmeier, S., Richter, B., and Heberle, J., *Journal of the American Chemical Society* **2004**, *126*(49),

- 16199–16206, Oriented attachment and membrane reconstitution of his-tagged cytochrome c oxidase to a gold electrode: In situ monitoring by surface-enhanced infrared absorption spectroscopy.
- [215] Friedrich, M. G., Robertson, J. W. F., Walz, D., Knoll, W., and Naumann, R. L. C., *Biophysical Journal* **2008**, 94(9), 3698–3705, Electronic wiring of a multi-redox site membrane protein in a biomimetic surface architecture.
- [216] Roskamp, R. F., *Diploma Thesis, Mainz, Germany* **2006**, Tethered Bilayer Lipid Membranes auf Aluminiumoxid.
- [217] Sugimoto, W., Iwata, H., Yokoshima, K., Murakami, Y., and Takasu, Y., *Journal of Physical Chemistry B* **2005**, 109(15), 7330–7338, Proton and electron conductivity in hydrous ruthenium oxides evaluated by electrochemical impedance spectroscopy: The origin of large capacitance.
- [218] Wu, S., Liu, X., Hu, T., Jiang, J., Chu, P. K., Yeung, K. W. K., Chung, C. Y., Chu, C. L., Xu, Z., Lu, W. W., Cheung, K. M. C., and Luk, K. D. K., *Journal of The Electrochemical Society* **2009**, 156(6), C187–C194, Electrochemical Stability of Orthopedic Porous NiTi Shape Memory Alloys Treated by Different Surface Modification Techniques.

Danksagung

Mein Dank gilt Prof. Dr. [REDACTED], Prof. Dr. [REDACTED] und Prof. Dr. [REDACTED] für die Möglichkeit, im Arbeitskreis der Materialwissenschaften zu promovieren.

An dieser Stelle möchte ich besonders meinem Projektleiter Dr. [REDACTED] danken. Für Führung und Freiheit in den Maßen und zu den Zeiten in denen ich sie brauchte, für seinen Glaube an meine Ideen und für ein Thema in dem ich sie auch testen und verwirklichen konnte.

Dr. [REDACTED] sei herzlich für seine Vorarbeit und die Einführung in das Thema Hydrogele gedankt.

Ebenso danke ich all meinen Projektpartnern, besonders:

Prof. Dr. [REDACTED], Dr. [REDACTED], Dr. [REDACTED], Dr. [REDACTED] und [REDACTED] vom FCS, μ PCS und Goldnanopartikel Projekt

Dr. [REDACTED] und [REDACTED] vom cLRSP und Biosensor Projekt

[REDACTED] und [REDACTED] vom WKB Projekt

Dr. [REDACTED] und [REDACTED] vom HGs-ptBLM Projekt

Dr. [REDACTED], Dr. med. [REDACTED], Dr. med. [REDACTED] und [REDACTED] vom Augenlinik Projekt

Prof. Dr. [REDACTED], Dr. [REDACTED] und Dr. [REDACTED]
vom ToF-SIMS Projekt

Ebenso danke ich Dr. [REDACTED], [REDACTED] und [REDACTED], ohne die hier
nichts ginge

Vielen Dank auch an [REDACTED], [REDACTED] und [REDACTED] für ihre
Hilfe im Labor, [REDACTED] und [REDACTED] vom NMR, [REDACTED]
[REDACTED] von der GPC und [REDACTED] für IT-Hilfen aller Art

Einige haben diese Arbeit Korrektur gelesen, besonders [REDACTED], [REDACTED], [REDACTED]
[REDACTED], [REDACTED], [REDACTED], [REDACTED] and [REDACTED] möchte
ich dafür danken

Den Physikern [REDACTED] und [REDACTED] danke ich für ihre Hilfe bei
theoretischen Fragen

[REDACTED] [REDACTED] für die Hilfe bei den Grafiken, speziell für die Abbil-
dungen 6.1 und 6.7

Allen Kollegen aus der Kaffecke, den Labors, dem Büro, Heraklion und
Adelaide ... Danke!

Schließlich und endlich:

meinen Freunden und meiner Familie

